Journal of Physics D:
Applied Physics

TOPICAL REVIEW • **OPEN ACCESS**

Iodine plasmas for space propulsion and industrial applications

To cite this article: Trevor Lafleur *et al* 2026 *J. Phys. D: Appl. Phys.* **59** 023001

IOP Publishing J. Phys. D: Appl. Phys. 59 (2026) 023001 https://doi.org/10.1088/1361-6463/ae2b7e

Journal of Physics D: Applied Physics

RECEIVED
12 August 2025

REVISED
20 October 2025

ACCEPTED FOR PUBLICATION
10 December 2025

PUBLISHED
30 December 2025

TOPICAL REVIEW

Iodine plasmas for space propulsion and industrial applications

Trevor Lafleur[1,*], Benjamin Esteves[2,3], Cyril Drag[3], Anne Bourdon[3], Pascal Chabert[3], Javier Martínez Martínez[4], Luca Vialetto[5], George Bowden[1] and Rawoof Shaik[1]

[1] School of Engineering and Technology, University of New South Wales Canberra, Canberra, ACT 2600, Australia
[2] Safran Spacecraft Propulsion, 27200 Vernon, France
[3] LPP, CNRS, Ecole Polytechnique, Sorbonne Université, F-91128 Palaiseau, France
[4] Private address, Madrid, Spain
[5] Department of Aeronautics and Astronautics, Stanford University, Stanford, CA 94305, United States of America
[*] Author to whom any correspondence should be addressed.

E-mail: t.lafleur@unsw.edu.au

Keywords: iodine, electric propulsion, alternative propellant, plasma etching

Abstract

With as many as 2000 satellites per year forecast to be launched over the next decade, onboard propulsion systems will become increasingly important for ensuring both mission success and a sustainable space environment. Plasma-based electric propulsion systems are particularly attractive because of their high fuel efficiency, but due to challenges with conventional propellants such as xenon, a strong interest in viable alternatives has emerged. One such alternative is iodine, which in addition to space-based applications, is also of use in a number of ground-based industrial applications such as plasma etching. With a lower cost, higher global production output, and a reduced ionization threshold compared with xenon, iodine has the potential to meet current and future space industry demand while also providing improved propulsion performance. Furthermore, iodine is a solid at typical ambient conditions with a high storage density. However, iodine is chemically reactive with many common materials and has a more complex plasma chemistry that includes molecular dissociation, attachment to form negative ions, and several ionization processes creating positive atomic and molecular ions. This topical review provides a comprehensive overview of iodine within the context of plasma applications and also serves as a useful data source for various thermodynamic properties, collision cross-sections, and iodine-surface interactions. In addition to discussing the physical and atomic/molecular properties of iodine, we also highlight important theoretical, numerical, and experimental work in the field and discuss the current state-of-the-art: including the space flight heritage of iodine-fueled propulsion systems and remaining research/-technical challenges.

1. Introduction

Iodine is a versatile substance that has a wide range of uses from wound dressings and disinfectants, to additives in common table salt [1]. However, within a plasma physics context it is still relatively new and has only received increased attention over the last ten years or so largely because of its possible viability as an alternative propellant for space propulsion [2]. High-performance electric propulsion systems such as gridded ion and Hall thrusters have successfully been used in space for more than 60 years [3]. While mercury propellant was chosen for the first gridded ion thrusters tested on the SERT-I spacecraft in 1964 [4], toxicity concerns eventually led to a shift towards xenon within the space community [5], and which has subsequently become the nominal propellant of choice.

As a propellant, xenon offers a number of strong advantages [3, 6]. Firstly, it is a noble gas that is nonreactive and compatible with most materials. It also has a high average atomic mass (131.3 u) and a relatively low ionization threshold energy (12.13 eV). A high atomic mass is usually favored for gridded ion and Hall thrusters as it yields a higher thrust-to-power ratio and thruster electrical efficiency [7]: important factors as most spacecraft are power limited and so a higher thrust can reduce maneuver

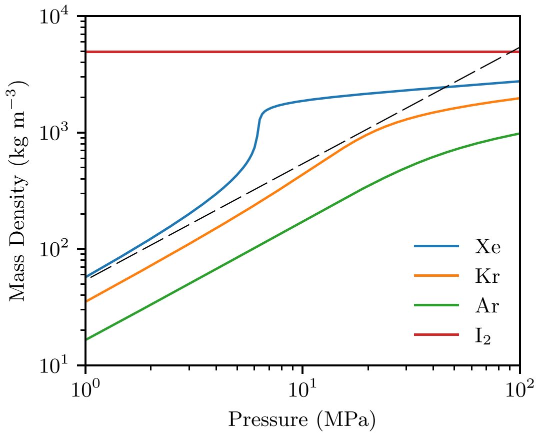

Figure 1. Mass density of xenon, krypton, and argon as a function of pressure at a temperature of 20 °C [8]. The black dashed line shows the expected density for xenon from the ideal gas law, while the solid red line shows the density of iodine under ambient conditions.

duration. Xenon also exhibits very attractive storage properties, as illustrated in figure 1 which shows the mass density as a function of pressure at a temperature of 20 °C. For pressures above approximately 6 MPa, xenon undergoes a phase transition from a gas to a supercritical fluid and its density increases substantially (particularly when compared with that expected from the ideal gas law; black dashed line in figure 1). A higher density implies a smaller storage tank size, which is again an advantage for spacecraft.

Xenon however presents several challenges. It is a relatively rare gas and production is through fractional distillation of air: a process that is time consuming and energy intensive. For example, for every 1000 metric tons of oxygen produced, only 1.2 kg of xenon are obtained [9]. Consequently, xenon can be relatively expensive (of the order of $5000 per kg) and global production is limited to around 50–60 metric tons per year [10]. This creates several emerging problems for the space industry. The rise of satellite constellations [11] has resulted in many hundreds, or even thousands, of satellites requiring onboard propulsion systems, and while economies-of-scale can be used to reduce satellite production costs, such cost savings usually do not extend to the propellant [12]. With the trend towards smaller satellites [13], and with such satellites often being launched via ride-share options or in batches, many satellite operators are looking at further reducing satellite costs. This includes having stand-alone propulsion systems that can be delivered pre-fueled and without any expensive or highly specialized propellant loading equipment being needed: a disadvantage with xenon because of its high storage pressure. Aside from representing a general explosion risk, high-pressure propellant storage can also cause potential blowout problems during launch (because of launch loads and intense vibrations), particularly for CubeSats launched via rideshare. Consequently, low-pressure propellant storage is ideally preferred where possible [14].

Cumulatively, between 17 000 and 300 000 satellites are forecast to be launched over the next 10 years [15, 16], and with the vast majority requiring onboard propulsion, space industry demand for xenon alone may outpace supply. Considering that the estimated average satellite mass is about 300 kg [16], and that the required propellant mass for missions in low-Earth orbit can represent as much as 11%–18% of the satellite mass [17], each satellite may require between 30 and 60 kg of propellant. Conservatively assuming 2000 satellites launched per year, the amount of xenon needed is between 60 and 120 metric tons per year: equal to or higher than current global production. Furthermore, this ignores the demand for xenon from other sectors such as the semiconductor, medical, and lighting industries, as well as large science experiments searching for dark matter [18]. While the above estimate is naturally very simplified and makes several assumptions, it nonetheless highlights the potential scale of the problem. Demand for xenon can also lead to strong market fluctuations, and for several deep-space science missions, xenon needs to be stockpiled in advance to prevent market collapse [10]. In the lead up to the war in Ukraine that broke out in 2022, the xenon market experienced a strong disruption (see figure 2) as Ukraine and Russia account for about 25%–30% of the world's xenon and krypton supply. This disruption initially caused a surge in market prices because of the drop in supply, although prices later stabilized as many industries dipped into their rare-gas reserves, invested in gas recycling technologies, or switched to alternatives.

The above challenges with xenon have provided a strong motivation to search for viable alternative propellants. Within the short term, krypton has emerged as an obvious candidate [12], and more

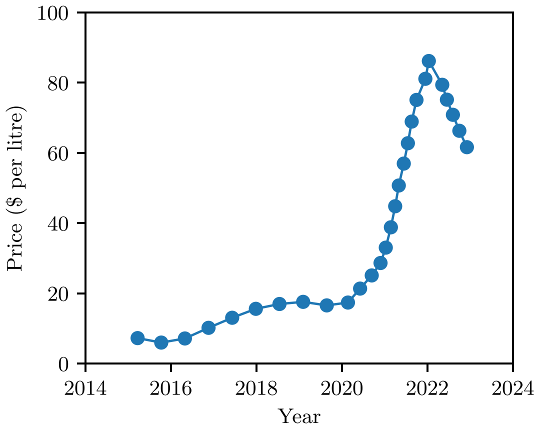

Figure 2. Cost of xenon as a function time indicating the strong market disruption caused by the war in Ukraine. Data taken from [19].

recently, even argon [20]. However, while the cost of krypton and argon are approximately one and two orders of magnitude lower than xenon respectively, their physical properties are less attractive. For example, both gases have lower atomic masses of 83.7988 u and 39.948 u, and higher ionization threshold energies of 14 eV and 15.76 eV. Consequently, the thrust-to-power ratio and electrical efficiency of the propulsion system is lower, which implies that either more satellite power is required, or that maneuver duration increases. Furthermore, the mass density of krypton and argon are much lower than xenon (even at high pressures), as seen in figure 1. Thus, not only does the storage tank size increase, but also the tank mass. This can then affect satellite design and launch costs.

An emerging alternative propellant that can address current concerns is iodine [2, 21, 22], which is also of interest for several ground-based applications such as plasma etching [23]. Located just adjacent to xenon in the periodic table of elements, it has a similar atomic mass of 126.9 u, and a lower atomic ionization threshold of 10.45 eV [24]. As a result, similar or even higher performance to xenon can be obtained. Figure 3 shows a photograph of a typical iodine plasma discharge where its characteristic yellow color is seen. The cost of iodine is approximately two orders of magnitude lower than xenon (although the price can depend strongly on the required purity), and global production sits at about 30 000 metric tons per year [25]: i.e. almost 500–600 times higher than xenon. Chile is the largest supplier of iodine (which is extracted from caliche ore) and accounts for almost two-thirds of global production. Japan is the second largest producer contributing roughly 30%, followed by Turkmenistan and Iran with approximately 3% and 2% respectively. With such a large global output, iodine has the potential to more than satisfy current and future space industry demand. However, the advantages of iodine go further as it is typically a solid at ambient conditions. It therefore has a higher storage density (see figure 1) and does not require pressurization. This significantly reduces the size and mass of the storage tank and overall propulsion system. These cost reducing factors make iodine particularly attractive for satellite constellations.

Iodine does however present certain difficulties, which most likely explains why it is only now being seriously considered as a propellant. Firstly, being stored as a solid complicates propellant delivery and flow control to the thruster. Secondly, iodine is significantly more chemically reactive than xenon and can corrode many common materials such as iron or aluminum [27]. Finally, while xenon is an atomic gas with a relatively simple plasma chemistry, iodine is initially in a molecular state and has a complex chemistry that includes collisional reactions such as dissociation into atomic iodine, and the formation of negative ions because of its high electron affinity [26, 28]. Until quite recently [29–31], many of the electron impact cross-sections for these reactions were not known. Consequently, a significant amount of research work has since occurred to study basic and applied iodine plasmas. Nonetheless, despite this recent progress, large uncertainties in cross-section data and reaction mechanisms still remain.

This topical review is dedicated to a comprehensive overview of iodine within the context of low-temperature plasma physics, while also acting as a single source of useful fundamental data (such as reaction cross-sections). We begin with a brief discussion on the history of iodine and highlight its physical and thermodynamic properties in section 2. We then introduce relevant iodine plasma chemistry (including both atomic and molecular reactions) in section 3, and iodine-surface interactions in section 4. Section 5 is then devoted to iodine plasma applications and important theoretical, numerical, and experimental research that has been conducted. A discussion of iodine propulsion testing in space

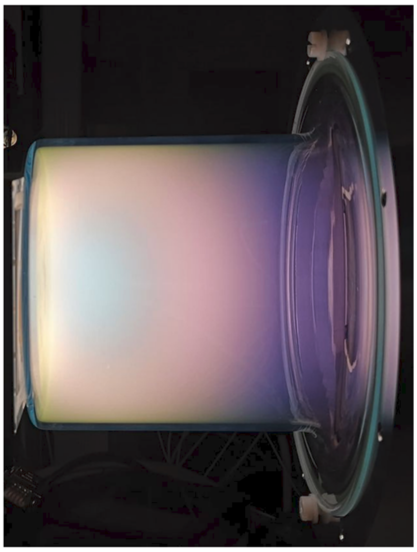

Figure 3. Photograph of a low-pressure iodine plasma produced in the PEGASES thruster prototype. Reproduced with permission from [26].

and possible emerging environmental considerations are presented in section 6. We then end by identifying remaining challenges and further required research in section 7, before providing a final outlook in section 8. Where possible, all fundamental data is either provided in the paper, or is available on the Zenodo repository [32].

2. Properties of iodine

2.1. Overview

Atomic iodine, I, is a non-metallic element of the halogen family that appears in Group 17 of the periodic table. The only stable isotope is iodine-127. Under standard conditions, iodine exists as a diatomic molecule, I_2, with two iodine atoms covalently bonded together. It is a bluish-black solid and has a glittering crystalline appearance. It has a moderate vapor pressure at room temperature, and in an open vessel, it slowly sublimates to a deep violet vapor that is irritating to the eyes, nose, and throat. Iodine melts at a relatively low temperature of 113.7 °C, and boils at 184.3 °C. The triple point temperature was recently determined to a high level of precision as 113.314 ± 0.005 °C [33]. Iodine was discovered by the French chemist Bernard Courtois in 1811 and was named two years later by Joseph Louis Gay-Lussac after the Ancient Greek word Ιώδης, which means 'violet'. Atomic and molecular term symbols are described in appendices A and B, while important thermodynamic properties for the solid, liquid, and gas phases are given in table 1. Additional properties are provided in section 2.3.

2.2. Physical properties

2.2.1. Vapor pressure

The evolution of iodine vapor pressure as a function of temperature is illustrated in figure 4. The earliest measurements, dating back to before 1926, were compiled from the International Critical Tables [34], noting significant uncertainties in pressures for temperatures below 0 °C. Several vapor pressure-temperature relationships can be employed, such as the common Dupré formula derived by integrating the Clausius–Clapeyron equation assuming that the heat of sublimation can be linearized. Gillespie and Fraser extended the vapor pressure measurements in 1936 and proposed the following empirical equation for the vapor pressure-temperature relationship [35]:

$$\log_{10} p = -\frac{3512.830}{T} - 2.013 \log_{10} T + 18.37972, \tag{1}$$

where p is the iodine vapor pressure in units of (Pa), and T is the temperature in (K).

Further measurements were conducted in the 1960s for temperatures between 43 °C and 80 °C, and which yielded values approximately 10% lower than previous measurements [36]. Dupré's law was slightly modified by Lindenberg [37], but the resulting values remained very similar to those given by the original relation. Additionally, the hyperfine transitions of molecular iodine in the visible spectrum

Table 1. Example thermodynamic properties of iodine.

Property	Value
Temperatures	
Melting point (θ_m)	386.85 K
Boiling point (θ_b)	457.45 K
Triple point	386.464 K, 12.1 kPa
Solid phase	
Density (298 K)	4.933 g cm^{-3}
Enthalpy of sublimation (298 K)	245.9 kJ kg^{-1}
Heat capacity (0.1 MPa, 298.15 K)	214.5 J kg^{-1} K^{-1}
Thermal conductivity (298 K)	0.449 W m^{-1} K^{-1}
Electrical conductivity	8×10^{-8} S m^{-1}
Thermal diffusivity	4×10^{-7} m^2 s^{-1}
Thermal effusivity	689.3 W $s^{1/2}$ m^{-2} K^{-1}
Liquid phase	
Enthalpy of fusion	61.1 kJ kg^{-1}
Heat capacity (0.1 MPa, 386.75 K)	313.4 J kg^{-1} K^{-1}
Gaseous phase	
Enthalpy of vaporization	163.8 kJ kg^{-1}
Heat capacity (I_2: 0.1 MPa, 298.15 K)	145.3 J kg^{-1} K^{-1}
Heat capacity (I: 0.1 MPa, 298.15 K)	163.8 J kg^{-1} K^{-1}

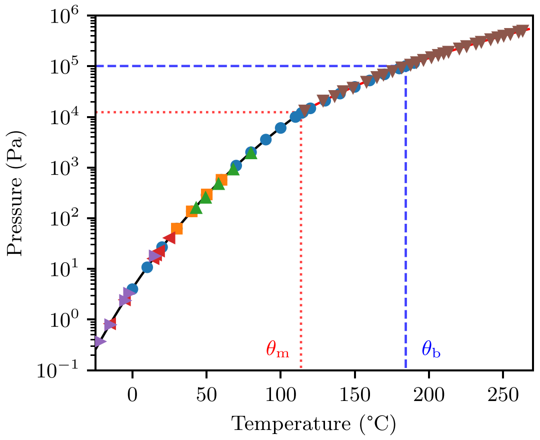

Figure 4. Iodine vapor pressure curve. The data markers correspond to different experimental measurements: blue circles [34], orange squares [35], green up triangles [36], red left triangles [40], purple right triangles [39], and brown down triangles [41] for the liquid phase only. The variation of vapor pressure for solid iodine is determined from equation (1) and is represented by the black curve, while that for the liquid phase is obtained using equation (2) and is represented by the red curve. The red and blue dotted vertical lines represent the melting and boiling temperatures respectively.

were recommended as standard frequencies by the Bureau International des Poids et Mesures (BIPM) [38–40]. In this high-resolution spectroscopy work, pressure effects leading to spectral broadening of laser absorption lines were measured with high precision. These pressure-dependent broadening measurements (for temperatures from 0 °C down to −22 °C), are consistent with Dupré's law to within an accuracy of the order of 4%.

In the liquid phase, the enthalpy of vaporization is lower than that of sublimation, resulting in a smaller slope in the vapor pressure-temperature variation. In addition to the data in [34], measurements published in 1979 [41] were fitted using a least-squares method to the Antoine equation with an average

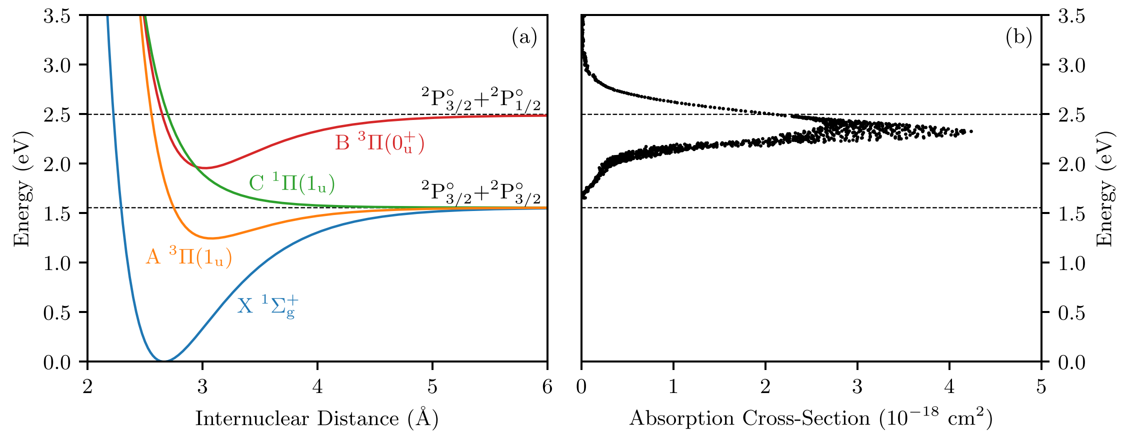

Figure 5. Visible absorption spectrum of I_2. (a) Relevant potential energy curves. (b) Absorption cross-section for $T = 300$ K as a function of wavenumber taken from [57]. The $I(^2P^\circ_{3/2}) + I(^2P^\circ_{3/2})$ and $I(^2P^\circ_{3/2}) + I(^2P^\circ_{1/2})$ dissociation limits are indicated by horizontal dashed lines in (a) and (b).

error of 0.66% for temperatures up to 263.2 °C:

$$\log_{10} p = 9.24828 - \frac{1694.23}{T - 58.32}. \tag{2}$$

The above equation yields pressures similar to those found in recent reference tables for gases and liquids (see for example [42]). Finally, it should be noted that when iodine is no longer in a controlled vacuum cell (where most vapor pressure-temperature measurements are performed), but rather at atmospheric pressure, the vapor pressure will be affected by the ambient pressure exerted on the solid or liquid surface. A vapor pressure correction was established by Poynting [43] but remains negligible (a difference of only 35 Pa at a temperature of 150 °C, for example).

2.2.2. Electronic spectroscopy of molecular iodine

Electronic spectroscopy of the iodine molecule was extensively performed in the second part of the 20th century. In 1978, an atlas of the absorption spectrum of molecular iodine in the energy range 1.83–2.48 eV was developed [44]. The study of the visible absorption spectrum of gaseous I_2 became a classic molecular spectroscopy experiment for undergraduate students in physical chemistry to determine spectroscopic constants [45]. Indeed, the vibrational-electronic spectrum of I_2 in the wavelength range between 500 and 640 nm displays a large number of well-defined bands. Near-ultraviolet (UV) and UV transitions were also well studied [46, 47]. Optical transitions of molecular iodine are also referenced as secondary frequency standards by the BIPM (around 515, 532, 543, 633, and 640 nm).

While known and studied for a century [48, 49], the visible spectrum of I_2 was carefully investigated by Tellinghuisen [50–53]. Three electronic transitions contribute to absorption in the visible region between 400 and 650 nm, and which is continuous below 500 nm (∼2.48 eV) but shows pronounced rovibrational structures between 500 and 630 nm (approximately 1.55–2.48 eV). These transitions are from the ground state $I_2(X\ ^1\Sigma_g^+)$ to the bound state $I_2(B\ ^3\Pi(0_u^+))$, correlated with the $I(^2P^\circ_{1/2})$ + $I(^2P^\circ_{3/2})$ dissociation limit, and the two 1_u states $I_2(A\ ^3\Pi(1_u))$ and $I_2(C\ ^1\Pi(1_u))$, correlated with the $I(^2P^\circ_{3/2})$ + $I(^2P^\circ_{3/2})$ dissociation limit. Potential energy curves (see also section 2.2.3) for the above molecular states are plotted in figure 5(a) which are taken from [54–56].

Recently, hyperfine spectroscopy studies have been carried out to develop an iodine atomic clock for wavelengths around 532 nm [58]. Beyond 2.48 eV, the diffuse part of the absorption spectrum leads exclusively to molecular photodissociation via the $I_2(B\ ^3\Pi(0_u^+))$ and $I_2(C\ ^1\Pi(1_u))$ states. This region is very interesting, in different ways, for absorption-based density measurements between a bound state and the continuum, especially in a plasma where pressures and temperatures are different from what they are in the normal gas phase. Contrary to optical transitions between bound states, the resonance condition is independent of the gas velocity and there is no saturation related to the stimulated emission at high laser intensities. It is also possible to detect the population of different rotational and vibrational levels of molecular iodine without changing the laser wavelength. This peculiarity was used by Esteves *et al* [26, 59] to directly measure the dissociation rate in iodine plasmas.

The effective absorption cross-section is well known experimentally at room temperature (see figure 5(b)), thanks to the growing interest in the role that iodine chemistry plays in a number of

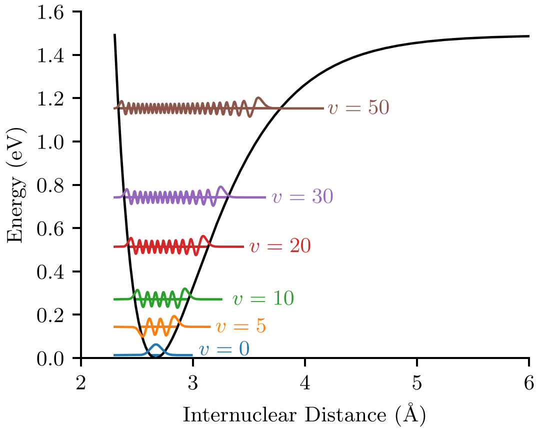

Figure 6. Potential energy curve for the iodine ground state $I_2(X\,^1\Sigma_g^+)$ using the Morse approximation. Example vibrational wave functions (with an arbitrary amplitude) are also shown.

atmospheric processes. The latest measurements of the absorption cross-section of iodine have been reviewed in a technical report from the Jet Propulsion Laboratory-Caltech committee on standards for atmospheric cross-sections [60] (see section 4H of the report). The recommended data are those computed by Saiz-Lopez and Plane [57].

2.2.3. Vibrational states of molecular iodine

For a diatomic molecule, an important property of an electronic state is its potential energy curve (energy as a function of the internuclear distance) as illustrated in figures 5(a) and 6. The curve can have a minimum thus leading to a bound state (such as the blue curve in figure 5(a) with an equilibrium internuclear distance of $r_e = 2.666$ Å [61] for the iodine ground state) or a repulsive state (such as the green curve in figure 5(a) monotonically decreasing and leading to dissociation). For high internuclear distances, the potential energy curve reaches an asymptotic value synonymous with dissociation. It has been found that the iodine ground state $I_2(X\,^1\Sigma_g^+)$ can be well approximated by a Morse potential at low internuclear distances [47, 62], as illustrated in figure 6 (where the ground state potential energy curve is repeated from figure 5).

Unlike atoms, diatomic molecules have two additional degrees of freedom which, until now, have largely been ignored in the study of iodine plasmas: vibration and rotation. A bound electronic state of a molecule is composed of several vibrational levels, which are quantized energy levels associated with the motion of the two iodine nuclei in the molecule. In the case of the iodine electronic ground state, over 60 vibrational levels are present. The first vibrational level, $v = 0$, has an energy of approximately 0.0133 eV (relative to the minimum of the potential energy curve), and the energy gap between the first two levels (E_1–E_0) is about 0.0266 eV in the Morse potential approximation. The energy gap between higher consecutive levels (E_{v+1}–E_v with $v > 0$) diminishes slightly with increasing vibrational level v because the potential is anharmonic. Each vibrational level can be represented by a vibrational wave function, whose radial profile is schematically drawn in figure 6 for several example levels. Note that with the exception of $v = 0$, the vibrational wavefunctions exhibit maxima around the turning points of the potential energy curve. The transition probability between two vibrational levels, according to the Frank–Condon principle, occurs at a fixed internuclear distance. As a result, the transition probability is higher when the overlap of the radial wave functions is maximized. This principle applies to both optical transitions and collision-induced phenomena.

The distribution of iodine vibrational levels is plotted in figure 7 for three different temperatures (300 K, 900 K, and 1500 K) assuming a Boltzmann distribution and using spectroscopic data for the energy of each vibrational level taken from [63]. At room temperature, the $v = 0$ level is by far the most populated (>60%) and the first three v-levels are enough to account for more than 90% of the total population. At 1500 K however, the distribution is much more homogeneous and 11 v-levels are necessary to account for 90% of the population. In iodine plasmas where gas temperatures above 1000 K have been measured [26], the first ten v-levels are therefore expected to be populated to a significant extent.

The iodine molecule can also be excited rotationally, and has a rotational constant of 4.67×10^{-6} eV [61]. At 300 K, the mean number of rotational levels for each v-level is 67. As of now, the

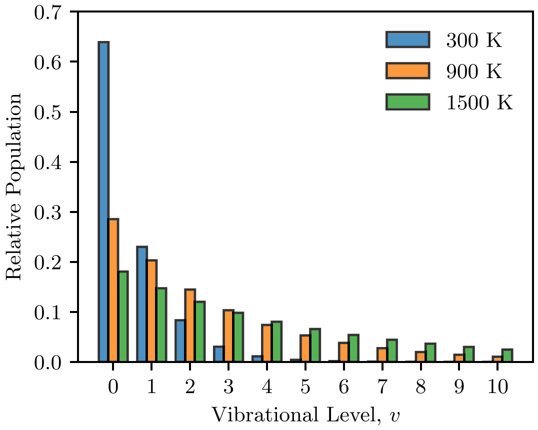

Figure 7. Distribution of the I_2 vibrational state population (assuming Boltzmann statistics) for the first 10 levels at temperatures of 300 K, 900 K, and 1500 K. Data for the energy of each vibrational level is taken from Herzberg [63].

effect of rotational excitation has been neglected in all iodine plasma studies. Additionally, no cross-section data for electron impact rotational excitation of I_2 is available. In the absence of such cross-section data, approximate theoretical expressions for diatomic molecules can be used instead (see for example [64, 65]).

2.3. Thermochemistry properties

While example thermodynamic and thermochemistry properties were given in table 1, these properties naturally vary with temperature and pressure, and this can be important for the operation of an iodine-fed plasma system. In particular, properties such as the gas phase thermal conductivity, specific heat at constant pressure, specific enthalpy, and viscosity, can be relevant to iodine gas flow, heating, and plasma discharge modeling. The variation of thermal conductivity with temperature for both atomic and molecular iodine is available from several sources based on experimental measurements or theoretical calculations. Example data from [66–68] is presented in figure 8 for the thermal conductivity and viscosity. In the temperature range illustrated, the thermal conductivity of atomic, κ_{I}, and molecular, κ_{I_2}, iodine are well described by the following best-fit empirical expressions

$$\kappa_{\mathrm{I}} = 5.307 \times 10^{-5} T_{\mathrm{I}}^{0.804}, \tag{3}$$

$$\kappa_{\mathrm{I}_2} = 1.167 \times 10^{-5} T_{\mathrm{I}_2}^{0.969}, \tag{4}$$

with T_{I} and T_{I_2} the atomic and molecular iodine temperatures respectively in units of (K), and where the thermal conductivity is in units of (W m^{-1} K^{-1}). The empirical relation for I_2 is similar to that independently obtained in [69]. As seen in figure 8, the empirical relations are in excellent agreement with available theoretical and experimental data in the indicated temperature range. Figure 8(b) shows a comparison of the viscosity where similar good agreement is observed. Best-fit empirical expressions of the atomic, μ_{I}, and molecular, μ_{I_2}, viscosity can be obtained using Sutherland's law

$$\mu_{\mathrm{I}} = 3.252 \times 10^{-5} \left(\frac{T_{\mathrm{I}}}{233}\right)^{3/2} \left(\frac{233}{233 + T_{\mathrm{I}}}\right), \tag{5}$$

$$\mu_{\mathrm{I}_2} = 4.424 \times 10^{-5} \left(\frac{T_{\mathrm{I}_2}}{473}\right)^{3/2} \left(\frac{473}{473 + T_{\mathrm{I}_2}}\right). \tag{6}$$

Here the temperature is again in units of (K), while viscosity is in units of (Pa s). Note that thermal conductivity and viscosity may also vary with pressure, but many experiments or databases only provide values at a certain reference pressure (typically about 0.1 MPa). The experimental data for the thermal conductivity in figure 8(a) however corresponds to pressures between 26 and 59 kPa. Comparison with the theoretical calculations performed at 0.1 MPa show negligible differences in this temperature range. Properties also naturally depend on the phase. Figure 9 provides a convenient summary of the phase and temperature dependence of the thermal conductivity for I_2 [70].

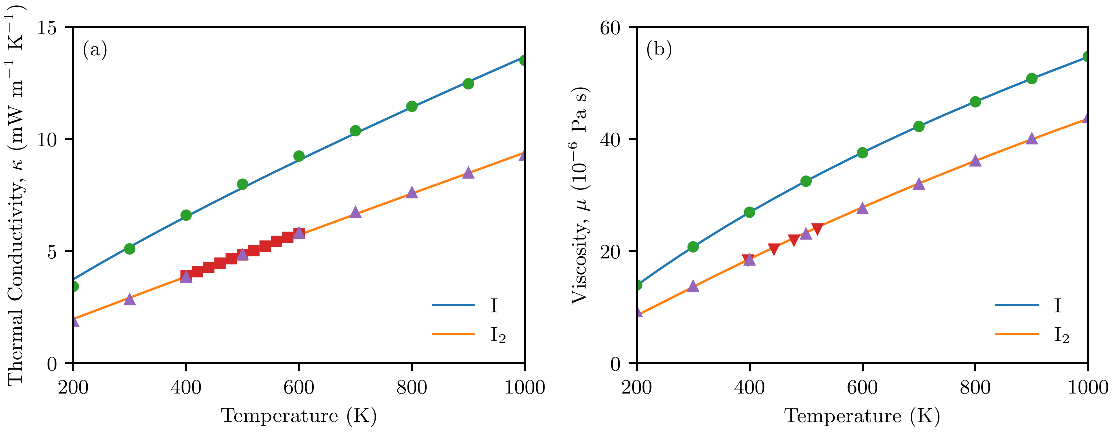

Figure 8. (a) Thermal conductivity and (b) viscosity as a function of temperature for I and I_2. The data markers correspond to different theoretical or experimental measurements: green circles [68], purple up triangles [68], red squares [66], and red down triangles [67].

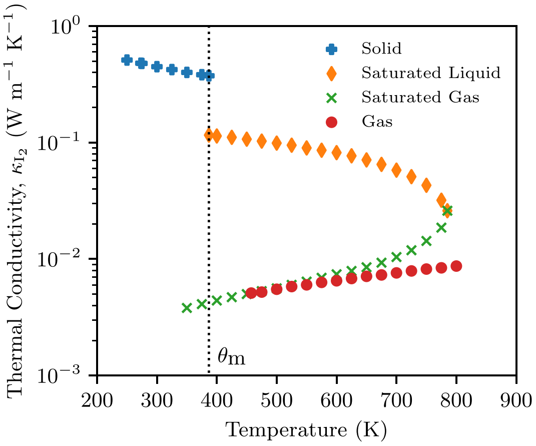

Figure 9. Thermal conductivity of I_2 in various states as a function of temperature. Data compiled by Ho *et al* [70].

Iodine plasmas operating at conditions where local thermodynamic equilibrium (LTE), or near-LTE, is satisfied have so far been of limited interest, and so other transport properties, such as the electrical conductivity, have not been required. Such properties are anyway more directly and accurately obtained from non-equilibrium plasma discharge models (see for example [26, 28, 71] as well as section 5.3). Other properties, such as the specific heat at constant pressure, c_p, the specific enthalpy, h, and the specific entropy, s, may however be useful for understanding iodine gas flow dynamics or designing gas flow systems. Such properties can be directly obtained from various databases (such as the JANAF tables [72]), or approximated by the NASA Glenn 9-coefficient polynomials

$$\frac{c_p(T)}{R} = a_1T^{-2} + a_2T^{-1} + a_3 + a_4T + a_5T^2 + a_6T^3 + a_7T^4, \tag{7}$$

$$\frac{h^0(T)}{RT} = -a_1T^{-2} + \frac{a_2\ln T}{T} + a_3 + \frac{a_4T}{2} + \frac{a_5T^2}{3} + \frac{a_6T^3}{4} + \frac{a_7T^4}{5} + \frac{b_1}{T}, \tag{8}$$

$$\frac{s^0(T)}{R} = -\frac{a_1T^{-2}}{2} - a_2T^{-1} + a_3\ln T + a_4T + \frac{a_5T^2}{2} + \frac{a_6T^3}{3} + \frac{a_7T^4}{4} + b_2, \tag{9}$$

where h^0 is a standard enthalpy relative to that at 298.15 K, and s^0 is a reference entropy at a standard pressure of 1 atm. The corresponding polynomial coefficients (i.e. a_1, a_2, etc) can be retrieved for I and

Table 2. NASA Glenn coefficients for I and I_2 for temperatures between 200–1000 K and 1000–6000 K.

Coefficient	Temperature range 200–1000 K	1000–6000 K
Atomic iodine, I		
a_1	1.698×10^{2}	-7.786×10^{5}
a_2	-2.716×10^{0}	2.303×10^{3}
a_3	2.517×10^{0}	2.887×10^{-3}
a_4	-5.731×10^{-5}	1.181×10^{-3}
a_5	1.032×10^{-7}	-2.264×10^{-7}
a_6	-9.671×10^{-11}	1.964×10^{-11}
a_7	3.706×10^{-14}	-6.244×10^{-16}
b_1	1.211×10^{4}	-2.617×10^{3}
b_2	7.406×10^{0}	2.559×10^{1}
Molecular iodine, I_2		
a_1	-5.088×10^{3}	-5.633×10^{6}
a_2	-1.250×10^{1}	1.794×10^{4}
a_3	4.504×10^{0}	-1.723×10^{1}
a_4	1.371×10^{-4}	1.244×10^{-2}
a_5	-1.391×10^{-7}	-3.333×10^{-6}
a_6	1.175×10^{-10}	4.125×10^{-10}
a_7	-2.338×10^{-14}	-1.960×10^{-14}
b_1	6.213×10^{3}	-1.069×10^{5}
b_2	5.584×10^{0}	1.601×10^{2}

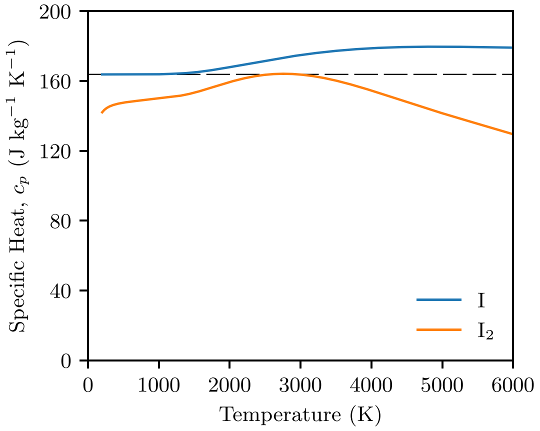

Figure 10. Specific heat at constant pressure for I and I_2. The black dashed line shows the theoretical value for a monatomic gas: $c_p = 5R/2$.

I_2 from various sources, such as the NASA ThermoBuild software [73, 74], and are tabulated in table 2 for temperature ranges between 200–1000 K and 1000–6000 K. Once c_p is known, the specific heat at constant pressure, c_v, can be found from the relation $c_V = c_p - R$, where R is the specific gas constant (equal to 65.52 J kg^{-1} K^{-1} for I and 32.76 J kg^{-1} K^{-1} for I_2). Figure 10 shows the specific heat as a function of temperature for pure I and I_2. While there is some minor variation for I_2, the specific heat is effectively constant for I below 1000 K, and is well approximated by the theoretical value for a monatomic gas: i.e. $c_p = 5R/2$.

If thermal dissociation occurs (see section 2.4), both I and I_2 species may be present in a general iodine gas flow. In this case, the total specific enthalpy and entropy can be computed from

$$h(T) = \sum_j h_j^0(T)\, x_j, \tag{10}$$

$$s(T,p) = \sum_j \left[s_j^0(T) - R_j \ln\left(\frac{p_j}{p_{\mathrm{ref}}}\right)\right] x_j, \tag{11}$$

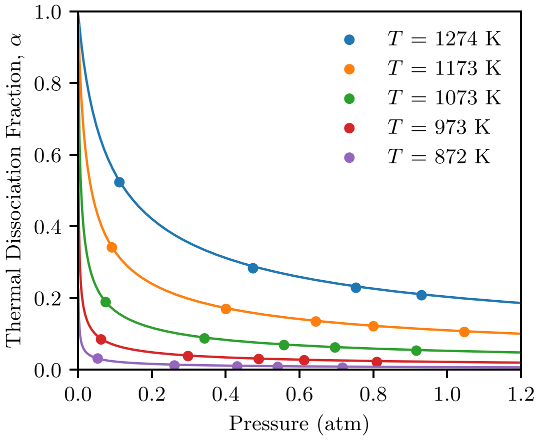

Figure 11. Measured dissociation fraction (data markers) from [78] as a function of pressure for various temperatures. The solid lines show predicted fractions obtained using equations (13) and (14).

where the sum is over I and I_2 species, $p_{\mathrm{ref}} = 1$ atm is a reference pressure, and x_j is the mass fraction of species j.

2.4. Dissociation

Thermal dissociation of I_2 leads to the formation of I according to the reaction: $I_2 \to 2I$. The equilibrium constant for partial pressures of this reaction, K_p, is a function of temperature only and is defined as:

$$K_p = \frac{p_{\mathrm{I}}^2}{p_{\mathrm{I}_2}} = k_{\mathrm{B}} T \frac{n_{\mathrm{I}}^2}{n_{\mathrm{I}_2}}, \tag{12}$$

where p_{I} and p_{I_2} are the atomic and molecular partial pressures respectively, and n_{I} and n_{I_2} are the corresponding number densities. By considering statistical physics and mass action laws, the equilibrium constant can be expressed in terms of the partition function of atoms and molecules [75]. Using the rigid rotator and harmonic oscillator approximation, and considering only the fundamental molecular potential energy curve, the equilibrium constant is given by [76]:

$$K_p = K_0 T^{3/2} \left(1 - \mathrm{e}^{-T_{\mathrm{v}}/T}\right) \mathrm{e}^{-D/T}, \tag{13}$$

with $K_0 = 2.26 \times 10^6\,\mathrm{Pa\,K^{-3/2}}$, D the binding energy of the molecules (1.54 eV = 17 855 K), and T_v the vibrational temperature (313 K). For temperatures above 1500 K, the partition functions must be corrected to account for excited electronic states and anharmonic spectroscopic constants [77].

The equilibrium constant allows the dissociation fraction, $\alpha = n_{\mathrm{I}}/(2n_{\mathrm{I}_2} + n_{\mathrm{I}})$, to be determined from

$$\alpha = \sqrt{\frac{K_p}{4p + K_p}}, \tag{14}$$

where p is the total pressure. Dissociation measurements [78] at different pressures and temperatures are shown in figure 11, together with the predicted dissociation fraction from equations (13) and (14). Despite the simplifying assumptions, the agreement is excellent.

In many plasma systems, the pressure is relatively low such that the predicted thermal dissociation degree may be significant. Figure 12 shows the dissociation fraction as a function of temperature for different representative pressures. For some electric propulsion systems, such as gridded ion or Hall thrusters, the operating pressure can be less than 1 Pa, indicating that thermal dissociation may be substantial. However, it should be noted that equations (13) and (14) are strictly valid only for conditions where thermodynamic equilibrium is satisfied, which is often not true for conditions relevant to electric propulsion systems. In this case, plasma dissociation (such as via electron impact dissociation processes; see section 3.3) may be more prevalent. The importance of thermal dissociation relative to plasma dissociation has been compared in controlled capacitively coupled radio-frequency (RF) discharges [59]. At low pressures, plasma dissociation dominates, but at higher pressures, thermal and plasma dissociation appears similar.

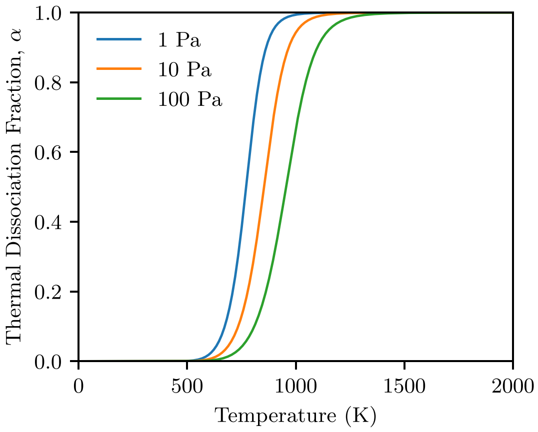

Figure 12. Thermal dissociation fraction as a function of temperature for different pressures.

If thermodynamic equilibrium is not satisfied, the thermal dissociation fraction may differ from that predicted by equations (13) and (14). In this case, dissociation and recombination processes may need to be directly treated from a more fundamental microscopic perspective. The relevant reactions are

$$\mathrm{A} + \mathrm{I}_2\left(\mathrm{X}\ {}^1\Sigma_\mathrm{g}^+\right) \longrightarrow \mathrm{A} + 2\mathrm{I}\left({}^2\mathrm{P}^\circ_{3/2}\right), \tag{15}$$

$$\mathrm{A} + 2\mathrm{I}\left({}^2\mathrm{P}^\circ_{3/2}\right) \longrightarrow \mathrm{A} + \mathrm{I}_2\left(\mathrm{X}\ {}^1\Sigma_\mathrm{g}^+\right), \tag{16}$$

where A represents either I or I_2 (or indeed any heavy particle species that may be present, including ions). The thermal dissociation and recombination rates are then given by $n_\mathrm{A} n_{\mathrm{I}_2} K_\mathrm{th,diss}$ and $n_\mathrm{A} n_\mathrm{I}^2 K_\mathrm{th,recom}$ with n_A the number density of species A, and $K_\mathrm{th,diss}$ and $K_\mathrm{th,recom}$ the thermal dissociation and recombination rate coefficients. Several works have measured or compiled such rate coefficients as a function of temperature for different species A including Baulch *et al* [79] and Ip and Burns [80]. Following Baulch *et al*:

$$K_\mathrm{th,diss} = 1.37 \times 10^{-16} \exp\left(-\frac{15\,250}{T}\right)\ \mathrm{m}^3\,\mathrm{s}^{-1}, \tag{17}$$

$$K_\mathrm{th,recom} = 6.51 \times 10^{-46} \exp\left(\frac{754}{T}\right)\ \mathrm{m}^6\,\mathrm{s}^{-1}. \tag{18}$$

Here the recommended values are based on various experimental measurements in the temperature range 800–2000 K (dissociation) and 290–1250 K (recombination), and with A = Ar (argon) or A = N_2 (molecular nitrogen) for dissociation, and A = Ar for recombination. In the absence of further data, it seems practical to extend the validity of the above rate coefficients to A = I and A = I_2.

3. Iodine plasma chemistry

3.1. Discharge composition

A wide range of neutral and charged particle species contribute to the overall dynamics of an iodine plasma discharge, including atomic iodine (I), molecular iodine (I_2), electrons (e^-), positive and negative atomic ions (I^+, I^-), and positive and negative molecular ions (I_2^+, I_3^+, I_2^-, I_3^-). These species can exist not only in their respective ground states, but also in excited electronic states, and in the case of molecules, excited vibrational and rotational states.

The foundation of ionization and molecular ion formation in halogen plasmas was established in the early 20th century. In 1925, Mohler [81] provided some of the first systematic measurements of electron impact ionization, while Hogness and Harkness [82] demonstrated the formation of molecular ions through charge-exchange and dissociative ionization processes, thus highlighting the importance of molecular species in plasma environments. Further refinements in understanding negative ion formation came from the work of Frost and McDowell [83], who investigated electron attachment processes in halogens, emphasizing iodine's strong electron affinity (3.06 eV) and its ability to form stable negative ions. Iodine is very electronegative as studied in several pioneering works such as those of Healey [84],

Table 3. Electron impact scattering processes for I. Here I* represents an excited state above the $I(^2P^\circ_{3/2})$ and $I(^2P^\circ_{1/2})$ states, while $n \geqslant 1$ is an integer.

ID	Reaction	Process	Threshold energy (eV)
B1	$I(^2P^\circ_{3/2}) + e^- \longrightarrow I(^2P^\circ_{3/2}) + e^-$	Elastic scattering	—
B2	$I(^2P^\circ_{1/2}) + e^- \longrightarrow I(^2P^\circ_{1/2}) + e^-$	Elastic scattering	—
B3	$I(^2P^\circ_{3/2}) + e^- \longrightarrow I^+ + 2\,e^-$	Ionization	10.451
B4	$I(^2P^\circ_{1/2}) + e^- \longrightarrow I^+ + 2\,e^-$	Ionization	9.5084
B5	$I(^2P^\circ_{3/2}) + e^- \longrightarrow I^{n+} + (n+1)\,e^-$	Multiple ionization	See table 4
B6	$I(^2P^\circ_{3/2}) + e^- \longrightarrow I(^2P^\circ_{1/2}) + e^-$	Electronic excitation	0.9426
B7	$I(^2P^\circ_{3/2}) + e^- \longrightarrow I^* + e^-$	Electronic excitation	See table 5
B8	$I(^2P^\circ_{1/2}) + e^- \longrightarrow I^* + e^-$	Electronic excitation	See table 5

Buchdahl [85], Biondi and Fox [86–88], Truby [89, 90], Woolsey *et al* [91] or Emeleus and Coulter [92], and can readily form negative ions (I^-) via electron attachment, while negative molecular ions (I_2^-, I_3^-) emerge through subsequent clustering reactions. However, at higher electron temperatures, such as those encountered in many electric propulsion systems, multiple ionization pathways can become significant. Successive ionization thresholds at 10.45 eV (I^+), 29.58 eV (I^{2+}), 59.15 eV (I^{3+}), and 99.51 eV (I^{4+}) can lead to the formation of highly charged species, which dominate in high-energy environments. In contrast, molecular ions (I_2^+, I_3^+) tend to dissociate at elevated temperatures due to electron-impact fragmentation, while negative ions undergo detachment and collisional destruction. The interplay between these species governs key plasma properties such as particle transport, ionization-loss balance, and recombination kinetics. Within the context of electric propulsion or materials processing applications, sophisticated mathematical models are needed to understand these complex interactions, and to aid system design and optimization. Such models require a broad range of input data that includes important species (both neutral and charged), collisional reaction processes, and collision cross-sections. This section focuses on the underlying plasma chemistry relevant to iodine discharges, and which is required not only for theoretical and numerical plasma models, but also the interpretation and analysis of certain diagnostics. A further discussion of mathematical models making use of this data is provided in section 5.3.

3.2. Electron impact scattering: atomic iodine

For electrons colliding with atomic iodine, the main processes are elastic scattering (which primarily changes the electron momentum) and inelastic processes such as ionization and electronic excitation. Each of these reaction types are discussed further in the subsections below, and are summarized in table 3. The spin–orbit coupling degeneracy of the atomic ground state results in the presence of an 'excited' state $I(^2P^\circ_{1/2})$ only 0.9426 eV [93] above the ground state $I(^2P^\circ_{3/2})$. Further details on the term symbols for atomic iodine are given in appendix A (and for molecular iodine in appendix B). When thermal dissociation occurs due to gas heating (see section 2.4), the $I(^2P^\circ_{1/2})$ state is always much less populated than the ground state, which can easily be seen by considering the system to be in LTE. At an example temperature of 1000 K ≈ 0.086 eV (and assuming Boltzmann statistics), the population density ratio of the first excited state to the ground state is approximately 8.7×10^{-6}. For most applications of current interest however, LTE is not satisfied and the electron temperature is much higher than both the ion and neutral temperatures. Consequently, dissociation due to electron impact processes dominates and can be significant. Since the electron temperature in many plasmas is of the order of 5 eV or higher, the $I(^2P^\circ_{1/2})$ state may be highly populated and strictly speaking should be treated as a separate species in any mathematical model. That being said, experiments in capacitive iodine discharges [94] have shown that the density of $I(^2P^\circ_{1/2})$ states may be relatively low under some conditions due to collisional quenching (see section 3.6).

3.2.1. Elastic scattering

Elastic scattering processes are indicated by reactions B1 and B2 in table 3. Total elastic scattering cross-sections for $I(^2P^\circ_{3/2})$ and $I(^2P^\circ_{1/2})$ have been calculated by Ambalampitiya *et al* [31] up to electron energies of 100 eV. Data for $I(^2P^\circ_{3/2})$ is shown in figure 13. While the cross-section for $I(^2P^\circ_{1/2})$

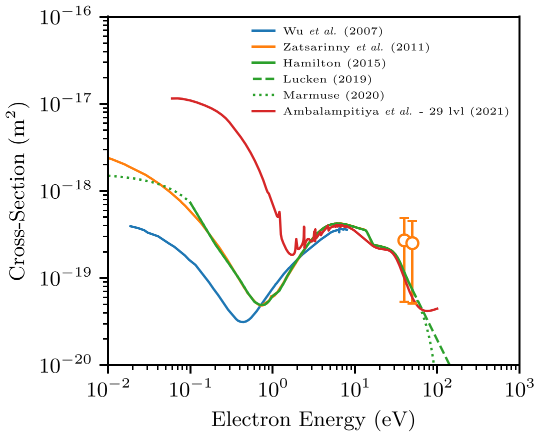

Figure 13. (Reaction B1 in table 3) Comparison of electron impact total elastic scattering cross-sections for I($^2P^\circ_{3/2}$) from available theoretical/numerical data in the literature. The orange circles show experimental data from Zatsarinny *et al* [96].

(not shown in figure 13) had not previously been calculated, the cross-section for I($^2P^\circ_{3/2}$) can be compared to earlier calculations (see figure 13). In 2007, Wu and Yuan [95] performed an 11-state close-coupling calculation for the interaction between a slow electron and ground state atomic iodine using the fully relativistic *R*-matrix method, although their study was limited to energies up to 8 eV. In 2011, Zatsarinny *et al* [96] expanded this work by performing a combined experimental and theoretical study. Experimental data was obtained by subtracting known cross-sections from measured data of a pyrolyzed mixed beam containing various atomic and molecular species. The calculations were conducted using both the fully relativistic Dirac B-Spline *R*-matrix (BSR) method and an optical model potential approach. Despite the complexity of the problem, the agreement between the theoretical predictions and experimental data for angle-differential and angle-integrated elastic cross-sections at 40 eV and 50 eV was found to be satisfactory.

Hamilton [29] also calculated total scattering cross-sections for I($^2P^\circ_{3/2}$), providing valuable data that was used in subsequent mathematical models by Grondein *et al* [71], Lucken [97], and Marmuse [98]. Lucken extrapolated the cross-section data at high energies using a log-linear law, while Marmuse used a power law at high energies and a quadratic law at low energies (see figure 13). While most calculations are in close agreement for electron energies between 3 and 50 eV, there are significant discrepancies below 3 eV. In particular, results differ by almost two orders of magnitude at 0.1 eV and the Ramsauer minima occurs at different energies. Currently, no known data exists for the elastic momentum transfer cross-sections (MTCSs) of either I($^2P^\circ_{3/2}$) or I($^2P^\circ_{1/2}$).

3.2.2. Ionization

Figure 14 shows electron impact ionization cross-sections for I($^2P^\circ_{3/2}$) taken from the literature. The threshold energy is 10.451 eV, which is a value measured more than sixty years ago [24] and commonly included in ionization energy tables of chemistry and physics handbooks. The only experimental data dates back to 1987 with the work of Hayes *et al* [99], where measurements were obtained using a crossed electron-beam fast-atom-beam method with an uncertainty of ±12%. Since then, at least nine different works have provided theoretical or semi-empirical cross-sections. Margreiter *et al* [100] applied the semi-classical Deutsch–Märk (DM) formalism, a semi-empirical method that fits parameters to experimental data. Later, Huo and Kim [101] utilized an effective core potential orbital approach, while Joshipura and Limbachiya [102] introduced the spherical complex optical potential (SCOP) model for ionization calculations. Bartlett and Stelbovics [103] improved calculations based on the Born approximation by incorporating orthogonalized plane waves that enhanced the accuracy of cross-section predictions. The Binary–Encounter–Bethe (BEB) model, originally formulated by Kim and Rudd [104], was later employed by Ali and Kim [105], Hamilton [29], and Ambalampitiya *et al* [31], the latter integrating effective-core potentials within Quantemol electron collisions (QECs) calculations. Vinodkumar *et al* [106] and Naghma *et al* [107] expanded on the SCOP method by introducing the Complex Scattering Potential-ionization contribution (CSP-ic) approach, which dynamically extracts the ionization cross-section from the total inelastic cross-section. The most recent calculations from Hamilton [29] and Ambalampitiya *et al* [31] appear the least consistent with experimental measurements (aside from the work of Bartlett *et al* which overestimates the cross-section as the method used is expected to be accurate

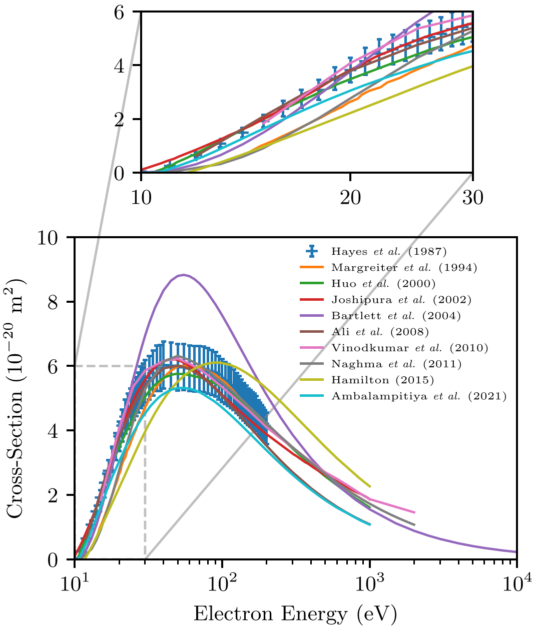

Figure 14. (Reaction B3 in table 3) Comparison of electron impact ionization cross-sections for $\mathrm{I}(^2\mathrm{P}^\circ_{3/2})$ from available data in the literature.

mostly at high electron energies). However, this discrepancy is expected as the BSR calculations include more coupled states which lead to a drop in the cross-section. As indicated in the zoomed region in figure 14, the ionization cross-sections show a fairly significant spread in values (as high as a factor of about two) for electron energies below 30 eV. Since the electron temperature in many iodine discharges is of the order of 5 eV, these differences naturally lead to important variations in the corresponding ionization rate coefficient (see section 3.7) which is crucial for plasma modeling.

Ionization from the $\mathrm{I}(^2\mathrm{P}^\circ_{1/2})$ state may also be important, and which would effectively represent a two-step ionization process involving excitation followed by ionization:

$$\mathrm{I}(^2\mathrm{P}^\circ_{1/2}) + \mathrm{e}^- \longrightarrow \mathrm{I}^+ + 2\,\mathrm{e}^-. \tag{19}$$

No data is available for the above ionization reaction, however, since the ionization cross-section for $\mathrm{I}(^2\mathrm{P}^\circ_{3/2})$ is known, several approaches can be employed to estimate it. For example, a common approach involves applying scaling laws based on the difference in ionization threshold energies and using the following empirical relation

$$\sigma_{\mathrm{iz},\mathrm{I}(^2\mathrm{P}^\circ_{1/2})}(\varepsilon) \approx \sigma_{\mathrm{iz,I}}\left(\varepsilon + \varepsilon_{\mathrm{exc}_1,\mathrm{I}}\right)\left[\frac{\varepsilon_{\mathrm{iz,I}}}{\varepsilon_{\mathrm{iz},\mathrm{I}(^2\mathrm{P}^\circ_{1/2})}}\right]^2, \tag{20}$$

where ε is the electron kinetic energy, $\sigma_{\mathrm{iz,I}}$ and $\sigma_{\mathrm{iz},\mathrm{I}(^2\mathrm{P}^\circ_{1/2})}$ are the ionization cross-sections of the $\mathrm{I}(^2\mathrm{P}^\circ_{3/2})$ and $\mathrm{I}(^2\mathrm{P}^\circ_{1/2})$ states respectively, and $\varepsilon_{\mathrm{iz,I}}$ and $\varepsilon_{\mathrm{iz},\mathrm{I}(^2\mathrm{P}^\circ_{1/2})} = \varepsilon_{\mathrm{iz,I}} - \varepsilon_{\mathrm{exc}_1,\mathrm{I}}$ are the corresponding ionization threshold energies with $\varepsilon_{\mathrm{exc}_1,\mathrm{I}}$ the excitation energy of $\mathrm{I}(^2\mathrm{P}^\circ_{1/2})$. Here, the ionization threshold of $\mathrm{I}(^2\mathrm{P}^\circ_{1/2})$ is shifted relative to that of $\mathrm{I}(^2\mathrm{P}^\circ_{3/2})$ as the minimum energy required for ionization is reduced accordingly by the excitation threshold energy. As an alternative approach, extrapolations of ionization cross-sections from chemically or electronically similar species may also provide reasonable estimates (e.g. chlorine, bromine, or fluorine).

In many iodine discharges, single ionization is usually sufficient for modeling and diagnostics purposes. However, in specific domains such as electric propulsion, where electron temperatures can reach several tens of electron volts in some devices (such as Hall thrusters), multiple ionization processes may become significant and should be considered to more accurately describe the plasma composition and dynamics. Only three known studies provide data for multiple ionization [99, 103, 105]. Table 4 lists the energy thresholds of the first four ionization processes with the corresponding cross-sections plotted in figure 15. Hayes *et al* [99] again remains the sole experimental reference, reporting single, double, and triple ionization cross-sections. Bartlett and Stelbovics [103] extended theoretical calculations up to

Table 4. Threshold energies for electron impact multiple ionization: $I(^2P^\circ_{3/2}) + e^- \rightarrow I^{n+} + (n+1)\,e^-$, for $n \in \{1,2,3,4\}$.

Process	Threshold energy (eV)
Single ionization	10.451
Double ionization	29.58
Triple ionization	59.15
Quadruple ionization	99.51

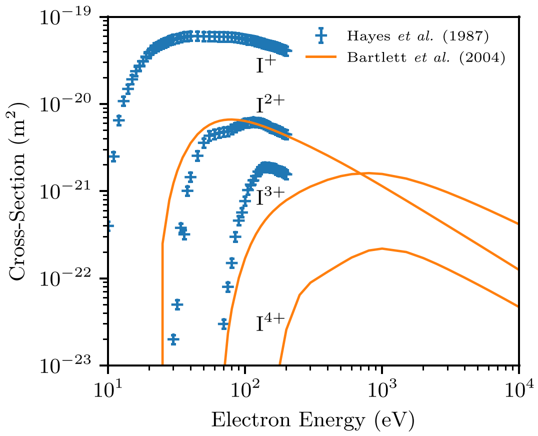

Figure 15. (Reaction B5 in table 3) Comparison of direct electron impact multiple ionization cross-sections from available data in the literature: $I(^2P^\circ_{3/2}) + e^- \longrightarrow I^{n+} + (n+1)\,e^-$, for $n \in \{1,2,3,4\}$.

quadruple ionization, while Ali and Kim [105] calculated indirect double ionization cross-sections (not shown).

3.2.3. Electronic excitation and de-excitation

No experimental measurements of electronic excitation cross-sections for atomic iodine are known, and additionally, there are few available theoretical calculations. Indeed, some early iodine plasma models neglected excitation reaction processes because of this (see for example [108]). The earliest known theoretical calculation was performed by Hamilton [29] in 2015, and was subsequently used in several iodine plasma models [71, 97, 98, 109]. In Hamilton's work, excitation was treated as a single process given by the following reaction:

$$I(^2P^\circ_{3/2}) + e^- \longrightarrow I^* + e^-, \qquad (21)$$

where I^* is an effective lumped excited state accounting for all possible excitation levels above the ground state and with an excitation threshold set to 0.9426 eV: i.e. the energy gap between the $I(^2P^\circ_{3/2})$ and $I(^2P^\circ_{1/2})$ states. The calculation used the BSR method of Zatsarinny and Bartschat [110], together with a close-coupling expansion and non-orthogonal bound and continuum orbitals. A plot of the computed cross-section is shown in figure 16. As noted in [28], a challenge with this cross-section is that it strongly underestimates electron energy losses in iodine plasmas at typical electron temperatures of relevance to electric propulsion. This is because the threshold energy is roughly an order of magnitude lower than the threshold energies of excited states above the first level (see table 5).

More detailed cross-sections were computed in 2021 by Ambalampitiya *et al* [31] who resolved individual levels due to excitation from both the $I(^2P^\circ_{3/2})$ and $I(^2P^\circ_{1/2})$ states. A semi-relativistic Breit–Pauli BSR (BPBSR) method was used [111–114] with either 10 or 25 target states in the close-coupling expansion considered, and which are referred to as BPBSR-10 or BPBSR-25 respectively. This work was also later extended to treat 29 target states (BPBSR-29). These new excitation cross-sections allow more sophisticated iodine plasma models to be built, and as shown in [26, 28], including the correct excitation thresholds of the individual levels can be important. These plasma models have been validated with experimental data and indicate that the theoretical cross-sections appear reasonable. Figure 16 shows a comparison of the total excitation cross-sections, while figure 17 shows excitation cross-sections for $I(^2P^\circ_{3/2})$ and $I(^2P^\circ_{1/2})$ to several higher states. The corresponding atomic configuration, term, and level energy are summarized in table 5, where it is seen that the level energies are in reasonable agreement with those from the National Institute of Standards and Technology (NIST) [93], although the predicted energy is slightly higher and two levels appear missing.

In many plasma models, detailed information on the evolution and dynamics of higher excited states is not usually needed as the density of these states is typically much lower than the $I(^2P^\circ_{3/2})$ ground state. However, as noted in section 3.1, it can be important to account for the $I(^2P^\circ_{1/2})$ state because of its low threshold energy. This state is also metastable with a very weak radiative decay probability. Higher excited state densities are usually very low in most plasma systems of current interest, but we note that if this is not the case, or if modeling of emission spectra is required, then radiative processes can become important. This was recently considered by Agrawl *et al* [115] who developed a collisional-radiative model to study the atomic iodine emission spectra produced in a low-pressure inductive plasma discharge.

In addition to excitation, electron impact de-excitation of the $I(^2P^\circ_{1/2})$ state should also be considered. While de-excitation cross-sections can easily be determined using the principle of detailed balance (see appendix C), for convenience we explicitly calculate this cross-section, and which is shown in figure 17(a).

More recently, Agrawal *et al* [115] have computed excitation cross-sections of 340 fine-structure levels for electron energies up to 500 eV. This work represents the largest known data set of excitation cross-sections that spans most levels likely to be of interest in the near future. Cross-sections were calculated using a fully relativistic distorted wave theory [116, 117], which is derived from a first-order perturbation theory. Example cross-sections obtained with this method are compared with those from Ambalampitiya *et al* [31] in figure 17, where reasonable agreement is found. Table 5 also lists the computed level energies for the first 31 (and the last 3) excited states. Overall, the agreement with NIST appears better than that of the BPBSR-29 model, although there are still slight differences and the energies of some states are higher than those from NIST. For convenience, the data in table 5 has been listed in energy ordered format using the results from Agrawal *et al* [115]. As data for 340 levels was calculated (and which is too large to list in this review paper), the reader is referred to [115] for information on excited states above number 31. Similarly, as there are too many cross-sections to individually plot, we only show some of the first levels in figure 17, while figure 16 shows the total excitation cross-section summed over all levels.

Although [115] and table 5 provides many individual excitation levels which may be required in some cases (such as collisional radiative models [115]), for many other models, such fine-grained detail is not needed. Therefore, having to directly deal with tens or hundreds of excitation levels can be cumbersome, and so making use of a fewer number of lumped excitation levels can often be more practical and convenient. Esteves [26] proposed a series of effective lumped levels based on the BPBSR-29 data, and which are summarized in table 6. Here, the zeroth and first levels correspond to the individual $I(^2P^\circ_{3/2})$ and $I(^2P^\circ_{1/2})$ states. However, higher excited states are grouped together into effective lumped levels that consists of individual states summed together. The level energy is then set equal to the threshold energy (based on the more accurate NIST values) of the lowest excited state included in that lumped level. Based on the detailed individual cross-sections, the effective cross-section for the lumped levels in table 6 can easily be obtained from the sum of individual levels. Similarly, rate coefficient can be calculated based on these cross-sections, as discussed in section 3.7.

3.2.4. Other processes

Aside from electron impact excitation of the $I(^2P^\circ_{3/2})$ and $I(^2P^\circ_{1/2})$ states, excitation of higher states can also occur, although no known cross-sections are available and such reactions have been of limited interest thus far.

3.3. Electron impact scattering: molecular iodine

In addition to electron impact elastic scattering, electronic excitation, and ionization, new reactions emerge in collisions with molecular iodine including vibrational excitation and various dissociation processes. Each of these reaction types are again highlighted in the subsections below and summarized in table 7. The molecular ground state is $I_2(X\ ^1\Sigma^+_g)$, with a further discussion of term symbols provided in appendix B. Since all available scattering data is based on electron impact of the molecular ground state, the term symbol will be omitted for convenience where possible and the ground state will simply be denoted as I_2.

3.3.1. Elastic scattering

Total elastic scattering and MTCSs for molecular iodine obtained from the literature are plotted in figure 18. The first known calculation of the total elastic scattering cross-section was performed by

Table 5. Energy ordered list of the first 31 (and last 3), excitation energy levels of atomic iodine following Agrawal *et al* [115]. Also shown are the corresponding level energies from Ambalampitiya *et al* [31] and NIST [93], as well as the total angular momentum quantum number, *J*, and level degeneracy, *g*.

					Level energy (eV)		
No.	Configuration	Term	*J*	*g*	[115]	[31]	NIST
0	$5p^5$	2P°	3/2	4	—	—	—
1	$5p^5$	2P°	1/2	2	0.9687	0.9529	0.9426
2	$5p^4(^3P_2)6s$	$^2[2]$	5/2	6	6.7655	7.2015	6.7737
3	$5p^4(^3P_2)6s$	$^2[2]$	3/2	4	6.9881	7.3939	6.9546
4	$5p^4(^3P_0)6s$	$^2[0]$	1/2	2	7.5365	8.1898	7.5502
5	$5p^4(^3P_1)6s$	$^2[1]$	3/2	4	7.5878	7.9452	7.6647
6	$5p^4(^3P_2)6p$	$^2[2]^\circ$	5/2	6	7.7717	8.1850	8.0473
7	$5p^4(^3P_2)6p$	$^2[2]^\circ$	3/2	4	7.8121	8.2217	8.0577
8	$5p^4(^3P_1)6s$	$^2[1]$	1/2	2	7.8292	8.0447	7.8341
9	$5p^4(^3P_2)6p$	$^2[3]^\circ$	7/2	8	7.8763	8.3228	8.1420
10	$5p^4(^3P_2)6p$	$^2[3]^\circ$	5/2	6	7.9007	8.3373	8.1389
11	$5p^4(^3P_2)6p$	$^2[1]^\circ$	7/2	8	7.9358	8.3503	8.1652
12	$5p^4(^3P_2)5d$	$^2[3]$	7/2	8	7.9699	8.3758	8.1848
13	$5p^4(^3P_2)5d$	$^2[3]$	5/2	6	8.0081	8.3867	8.1855
14	$5p^4(^3P_2)5d$	$^2[1]$	3/2	4	8.0784	8.4546	8.2270
15	$5p^4(^3P_2)6p$	$^2[1]^\circ$	3/2	4	8.1305	8.4810	8.3146
16	$5p^4(^3P_2)5d$	$^2[1]$	1/2	2	8.1748	8.5757	8.3439
17	$5p^4(^3P_2)5d$	$^2[4]$	9/2	10	8.1923	8.6837	8.3970
18	$5p^4(^3P_2)5d$	$^2[4]$	7/2	8	8.3158	8.7887	8.5003
19	$5p^4(^3P_2)5d$	$^2[2]$	3/2	4	8.4002	9.0054	8.7229
20	$5p^4(^3P_2)5d$	$^2[0]$	1/2	2	8.4069	8.8971	8.5073
21	$5p^4(^3P_2)5d$	$^2[2]$	5/2	6	8.4185	9.0064	8.6976
22	$5p^4(^3P_1)6p$	$^2[0]^\circ$	1/2	2	8.5620	8.9594	8.8650
23	$5p^4(^3P_2)7s$	$^2[2]$	5/2	6	8.6100	9.0545	8.9149
24	$5p^4(^3P_0)6p$	$^2[1]^\circ$	3/2	4	8.6426	9.0841	8.9240
25	$5p^4(^3P_1)6p$	$^2[2]^\circ$	5/2	6	8.6432	—	8.9925
26	$5p^4(^3P_0)6p$	$^2[1]^\circ$	1/2	2	8.6491	9.0330	8.9038
27	$5p^4(^3P_2)7s$	$^2[2]$	3/2	4	8.6901	9.1104	8.9634
28	$5p^4(^3P_1)6p$	$^2[2]^\circ$	3/2	4	8.7178	—	9.0269
29	$5p^4(^1D_2)6s$	$^2[2]$	5/2	6	8.7409	8.8837	8.5038
30	$5p^4(^1D_2)6s$	$^2[2]$	3/2	4	8.7567	8.8700	8.4991
⋮	⋮	⋮	⋮	⋮	⋮	⋮	⋮
337	$5p^4(^1S_0)9s$	$^2[0]$	1/2	2	13.7140	—	—
338	$5p^4(^1S_0)7d$	$^2[2]$	5/2	6	13.8221	—	—
339	$5p^4(^1S_0)5d$	$^2[1]$	3/2	4	14.5976	—	—

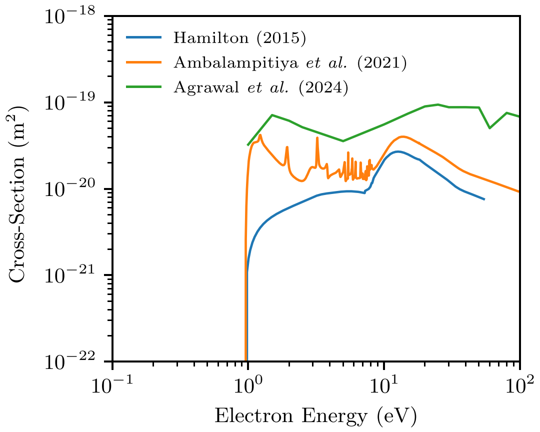

Figure 16. (Reaction B7 in table 3) Comparison of the total atomic iodine excitation cross-section for I($^2P^\circ_{3/2}$) from available data in the literature.

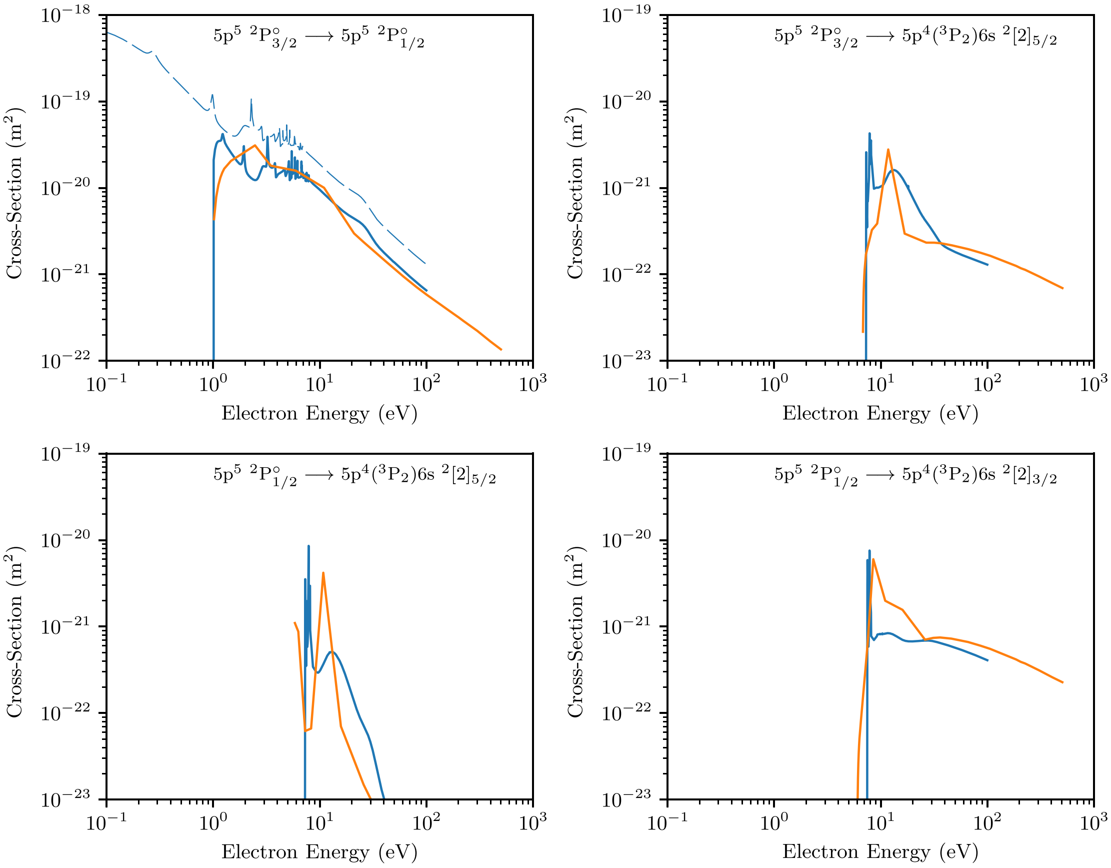

Figure 17. (Reactions B6–B8 in table 3) Comparison of the excitation cross-sections from Ambalampitiya *et al* [31] (blue lines) and Agrawal *et al* [115] (orange lines) for the first two transitions from the I($^2P^\circ_{3/2}$) ground state (top row), and the first two transitions from the I($^2P^\circ_{1/2}$) excited state (bottom row). Also shown is the de-excitation cross-section (dashed line; top left) computed using the principle of detailed balance (see appendix C).

Table 6. Energy ordered list of effective lumped excitation levels based on the BPBSR-29 model [26]. The last column lists the number of individual levels included in each effective level.

No.	g	Energy (eV)	No. Levels
0	4	—	1
1	2	0.9426	1
2	18	6.7736	5
3	26	8.0473	5
4	82	8.1848	17

Hamilton [29] in 2015, and which was adopted—along with various extrapolations—by Grondein *et al* [71], Lucken [97], and Marmuse [98]. Ambalampitiya *et al* [31] later provided new calculations for both total elastic scattering and MTCSs covering a broad range of electron energies. This data was subsequently used by Esteves [26], who extrapolated the data at both low (assuming a constant value) and high (assuming an inverse power law) energies. This extrapolation procedure follows the methodology introduced by Marmuse [98] and is consistent with the approach suggested by Tallents [118]. In 2020, Yadav *et al* [119] introduced new cross-section calculations using the *R*-matrix method with two different models: the static exchange plus polarization method and the configuration interaction technique [120]. While these cross-sections align reasonably well with those of Ambalampitiya *et al* [31], the MTCS is approximately five times larger. The magnitude of the MTCSs from both Ambalampitiya *et al* and Yadav are significant and suggest that elastic backward scattering plays an important role for electrons in I_2. However, similar elastic angular scattering has not been observed in other halogen gases, such as chlorine. Hence, further work is needed to clarify the role of electron momentum transfer during collisions with I_2.

Table 7. Electron impact scattering processes for I_2. Here I_2^* represents an electronically excited state above the $I_2(X\,^1\Sigma_g^+)$ ground state (denoted simply as I_2 for convenience), while v labels the vibrational level. Note that although the threshold energy for reaction C4 is set equal to the dissociation energy of the molecular ground state, the actual energy may vary depending on the specific dissociation pathway (see section 3.3.3).

ID	Reaction	Process	Threshold energy (eV)
C1	$I_2 + e^- \longrightarrow I_2 + e^-$	Elastic scattering	—
C2	$I_2 + e^- \longrightarrow I_2^+ + 2\,e^-$	Ionization	9.31
C3	$I_2 + e^- \longrightarrow I(^2P^\circ_{3/2}) + I^+ + 2\,e^-$	Dissociative ionization	11.63
C4	$I_2 + e^- \longrightarrow 2\,I(^2P^\circ_{3/2}) + e^-$	Dissociation	1.542
C5	$I_2 + e^- \longrightarrow I(^2P^\circ_{1/2}) + I^-$	Dissociative attachment	—
C6	$I_2 + e^- \longrightarrow I_2^* + e^-$	Electronic excitation	See table 8
C7	$I_2(v=0) + e^- \longrightarrow I_2(v>0) + e^-$	Vibrational excitation	~0.0266 per level

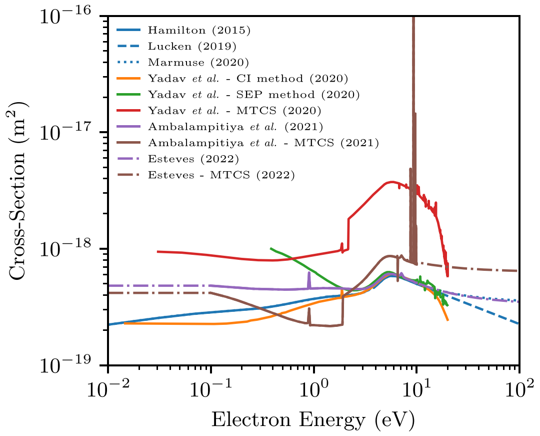

Figure 18. (Reaction C1 in table 7) Comparison of the total elastic scattering and momentum transfer cross-sections (MTCS) for I_2 from available data in the literature.

3.3.2. Ionization

No known experimental data is available for electron impact ionization of I_2, although the ionization threshold energy is well established at 9.31 eV (as experimentally determined by Cockett *et al* [121], for example). In the absence of direct measurements, several theoretical and semi-empirical approaches have been developed to estimate the ionization cross-section, and which are highlighted in figure 19. Among them, Deutsch *et al* [122] introduced the defect concept method, while Probst *et al* [123] applied the DM formalism, relying on semi-classical parameter fitting. Joshipura and Limbachiya [102] extended the SCOP model, and the BEB model (initially formulated by Kim and Rudd [104]), was again later employed by Ali *et al* [105] and Hamilton [29], with Ali *et al* incorporating the screening effect potential method for improved accuracy. Yadav *et al* [119] refined the SCOP model further through the CSP-ic approach, while Ambalampitiya *et al* [31] integrated effective-core potential effects within QEC calculations. In several of the above works, only the total ionization cross-section is determined, which is the sum of direct and dissociative ionization processes

$$I_2 + e^- \longrightarrow I_2^+ + 2\,e^-, \tag{22}$$

$$I_2 + e^- \longrightarrow I(^2P^\circ_{3/2}) + I^+ + 2\,e^-. \tag{23}$$

Ionization cross-sections for each individual process are then established by assuming a constant, energy-independent, branching ratio. For example, Ambalampitiya *et al* [31] assumed a ratio of 0.9 and 0.1 for each process respectively. Thus, the assumed iodine branching ratio represents an additional uncertainty.

3.3.3. Dissociative processes

Aside from thermal dissociation discussed in section 2.4, electron impact dissociation is an important process that tends to dominate at low pressures. The only known dissociation cross-section is from Hamilton [29], which is plotted in figure 20. The reaction threshold energy was fixed to 1.542 eV, which corresponds to the dissociation limit of the molecular ground state [61]. The atomic dissociation

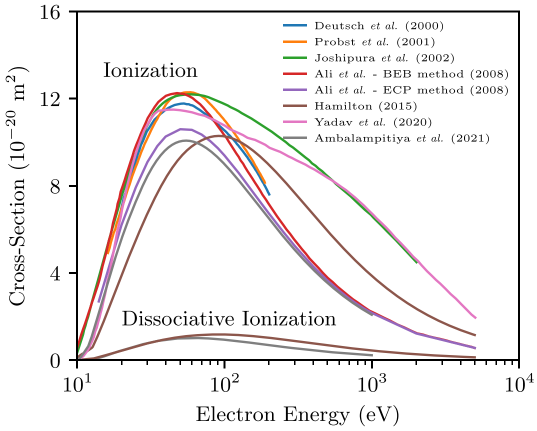

Figure 19. (Reactions C2–C3 in table 7) Comparison of ionization cross-sections for I_2 from available data in the literature.

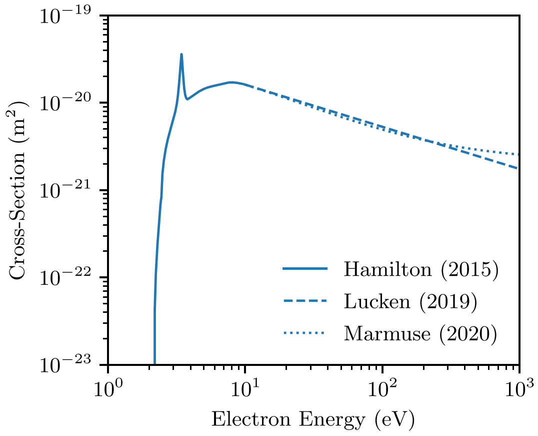

Figure 20. (Reaction C4 in table 7) Dissociation cross-section for I_2 from available data in the literature.

products were assumed to be in the $I(^2P^\circ_{3/2})$ ground state. Unfortunately, data is only available for electron energies below 10 eV, which is typically insufficient for an accurate description of most iodine discharges. Several previous models have therefore extrapolated the data at high energy using either a log-linear or inverse power law [26, 28, 97, 98]. Dissociation can be viewed as a multi-step process whereby an electron first transfers energy to the molecule placing it into one of a number of possible bound or repulsive excited states. Repulsive states can subsequently dissociate into a combination of different $I(^2P^\circ_{3/2})$ or $I(^2P^\circ_{1/2})$ atomic states, or even ionic states [124]. Information on these dissociation pathways is not well known.

Dissociative electron attachment is a reaction whereby the incident electron initially becomes attached to the molecule. The molecule then dissociates and the electron remains bound to one of the resulting atoms to form a negative ion (I^-). This reaction is particularly important in low-pressure iodine discharges as it is the main process leading to the creation of negative ions. Figure 21 shows a comparison of the dissociative electron attachment cross-sections from data available in the literature (obtained either experimentally, theoretically or with numerical simulations) spanning a wide energy range from 0.01 to 100 eV. This includes early works by Healey [84], Buchdahl [85], Biondi and Fox [86–88], and Frost and McDowell [83] (where the data were normalized to Buchdahl's maximum cross-section), subsequent works by Tam and Wong [125], Brooks *et al* [126], Kurepa *et al* [127] and Pozdneev [128], as well as more recent evaluations by Hamilton [29] and Ambalampitiya *et al* [31]. The cross-sections from Tam *et al* and Kurepa *et al* were normalized by setting the total attachment rate coefficient at room temperature (obtained by integrating over a Maxwellian distribution) equal to the value of Truby [89] (the I_2 attachment rate coefficient has been measured several times and its dependence on the gas temperature discussed in different works; see for example [84, 89, 90, 127, 129–132]). For energies below 1 eV, there is significant disagreement across all data sources. Caledonia *et al* [133] and Ayala

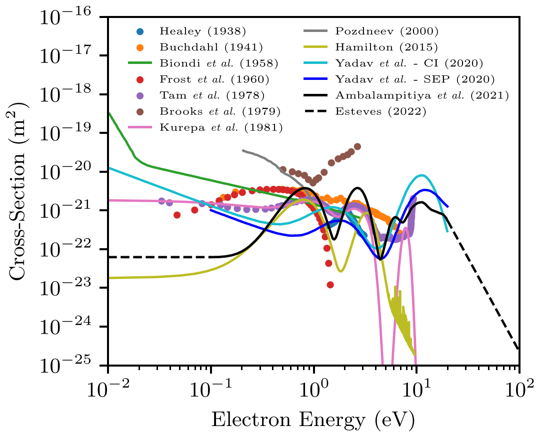

Figure 21. (Reaction C5 in table 7) Comparison of dissociative electron attachment cross-sections for I_2 from available data in the literature.

et al [131] had already highlighted these discrepancies stating that the Biondi and Fox experiments [86–88] were conducted in the presence of hydrogen iodide (HI), which is known to exhibit a large thermal electron attachment cross-section. The presence of HI impurities may therefore account for the discrepancies between their findings and those of other published works [83, 85, 89, 90]. Gallagher *et al* [132] also heavily disregarded Healey's results because of their disagreement with Brook's data. As noted by Ambalampitiya *et al*, the neutral atomic dissociation product is predicted to be the I($^2P^\circ_{1/2}$) state, which has largely been ignored in previous plasma modeling work (with the notable exception of [26]) and which seems to be in contradiction with other works (see section 7.5).

Finally, dissociative ionization is another important dissociation reaction that was already highlighted in section 3.3.2. From Ambalampitiya *et al* [31], the neutral atomic dissociation product is assumed to be the I($^2P^\circ_{3/2}$) ground state. The calculated threshold energy of 11.94 eV is similar to the sum of the photoionization energy (about 8.9 eV; see [134]) and the electron affinity of atomic iodine (approximately 3.06 eV; see [135]). This is also close to the experimentally measured value of 11.63 ±0.05 eV [136]. Differences with the dissociative ionization cross-section originally calculated by Hamilton [29] are very minor, although as noted in section 3.3.2, an assumption is made on the branching ratio of the different ionization pathways.

3.3.4. Electronic excitation

The first known calculations of electron impact electronic excitation of I_2 were performed by Yadav *et al* [119], who considered six excited states: $^3\Pi_u$, $^1\Pi_u$, $^3\Sigma_g^-$, $^1\Sigma_g^+$ (two states), and $^1\Sigma_g^-$. In 2021, Ambalampitiya *et al* [31] performed similar calculations with four excited states: $^3\Pi_u$, $^1\Pi_u$, $^3\Sigma_g^-$, and $^1\Sigma_g^+$. Before these works, iodine plasma models did not account for molecular electronic excitation as no cross-sections were available, and because the dissociation threshold energy is lower than the excitation threshold energies such that excited states were assumed to become dissociated [97].

The levels and notations of molecular excited states used by Ambalampitiya *et al* [31] and Yadav *et al* [119] differ from that used by other authors (see for example [137]). This is related to whether relativistic effects are accounted for in the molecular potential calculations. The notation used by spectroscopists [61, 138] is much closer to that used by Poline *et al* [137]. It is not easy to exactly match the states obtained by relativistic and non-relativistic calculations. Moreover, the threshold energies depend on the calculation method used, which not only differs between authors, but also with precise spectroscopic measurements. This largely explains the discrepancies in table 8 which summarizes several excitation reactions.

The sum of all molecular excitation cross-sections are plotted in figure 22. While the trends agree quite well, the total cross-section from Yadav *et al* is about two times higher than that from Ambalampitiya *et al*. As mentioned previously in section 3.2.3, if the density of excited states is important, or if emission spectra are needed (such as for diagnostic purposes), radiative processes need to be considered. No known collisional-radiative models accounting for emission from molecular iodine exist, although Prince *et al* [139, 140] have performed measurements to enable the development of such models, particularly within the context of diagnosing iodine thruster plumes. Prince *et al* have measured apparent excitation cross-sections for photoemission from iodine plasmas for wavelengths between 300 and 1050 nm. Emission was observed from I^*, I_2^*, I^{+*}, and I_2^{+*} species produced during various electron

Table 8. List of molecular electronic excitation reactions available from the literature. In the work by Yadav *et al* [119], two $^1\Sigma_g^+$ states are considered with different excitation cross-sections.

		Threshold energy (eV)		
ID	Reaction	Calculation [31, 119]	Theory [138]	Experiment [139, 141]
C6-1	$I_2 + e^- \longrightarrow I_2\ (^3\Pi_u) + e^-$	2.18 ; 2.18	2.37	1.25 ; 1.95
C6-2	$I_2 + e^- \longrightarrow I_2\ (^1\Pi_u) + e^-$	3.00 ; 2.99	2.38	—
C6-3	$I_2 + e^- \longrightarrow I_2\ (^3\Sigma_g^-) + e^-$	5.18 ; 5.44	3.90	5.04
C6-4	$I_2 + e^- \longrightarrow I_2\ (^1\Sigma_g^-) + e^-$	— ; 6.26	4.4	—
C6-5	$I_2 + e^- \longrightarrow I_2\ (^1\Sigma_g^+) + e^-$	5.70; 6.80	—	—

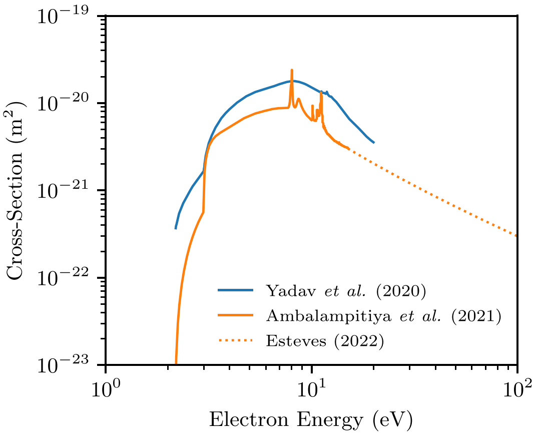

Figure 22. (Reaction C6 in table 7) Total electronic excitation cross-sections for I_2 from available data in the literature.

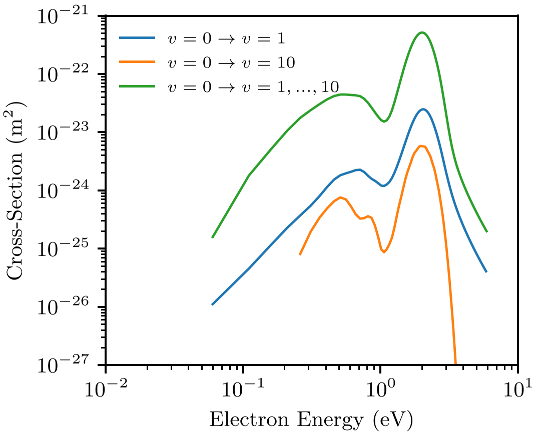

Figure 23. (Reaction C7 in table 7) Example electron impact vibrational excitation cross-sections of molecular iodine for $v = 0$ to $v = 1$, $v = 0$ to $v = 10$, and the combined sum of $v = 0$ to $v = k$ for $k \in \{1, \ldots, 10\}$.

impact collisions of I_2 for electron energies between about 4 and 100 eV. The authors note however that interpretation of the results is limited by several factors including a constrained spectral range, cascading processes from higher excited states, and congested spectral data.

3.3.5. Vibrational excitation

The only known electron impact vibrational excitation cross-sections were calculated by Ambalampitiya *et al* [31] up to electron energies of approximately 6 eV. These calculations treat vibrational excitation from the molecular ground state $I_2(X\ ^1\Sigma_g^+, v = 0)$ to the first ten vibrational levels, and approximate I_2 as a harmonic oscillator. The energy difference between successive vibrational levels corresponds to 0.0266 eV. Figure 23 shows example cross-sections for the first transition (from $v = 0$ to $v = 1$) and the last (from $v = 0$ to $v = 10$), as well as the sum of all ten contributions. Two peaks are observed and which are centered around 0.5 eV (due to the $^2\Pi_g$ resonance) and 2 eV (due to the $^2\Pi_u$ resonance).

Table 9. Example ion-neutral collisional processes. A negative threshold energy indicates an exothermic reaction with energy release.

ID	Reaction	Process	Threshold energy (eV)
D1	$I(^2P^\circ_{3/2}) + I^+ \longrightarrow I^+ + I(^2P^\circ_{3/2})$	Charge-exchange	—
D2	$I_2 + I^+ \longrightarrow I_2^+ + I(^2P^\circ_{3/2})$	Charge-exchange	−1.14
D3	$I_2 + I_2^+ \longrightarrow I_2^+ + I_2$	Charge-exchange	—
D4	$I_2 + I^+ \longrightarrow 2\,I(^2P^\circ_{3/2}) + I^+$	Dissociation	1.542
D5	$I_2 + I_2^+ \longrightarrow I_2 + I(^2P^\circ_{3/2}) + I^+$	Dissociation	2.68

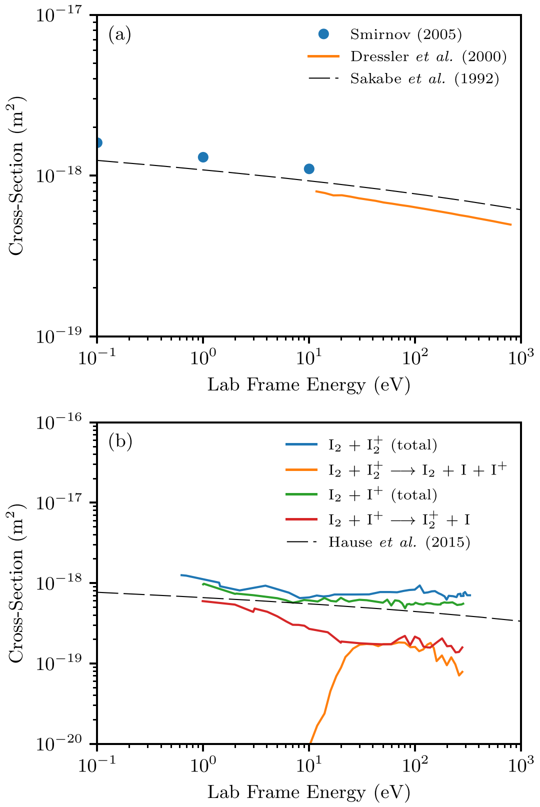

Figure 24. (Reactions D1–D5 in table 9) Ion-neutral collision cross-sections as a function of the lab frame energy for (a) $I + I^+$ and (b) $I_2 + I^+$ and $I_2 + I_2^+$. Data taken from [21, 146]. The dashed line in (a) shows the empirical cross-section from Sakabe *et al* [147], while the dashed line in (b) shows the empirical cross-section from equation (24) for $I_2 + I^+$.

Compared with other electron impact processes, the contribution of vibrational excitation appears small. Nonetheless, it may be important in some plasma discharges to correctly account for electron energy losses or neutral gas heating. For example, in addition to electron impact vibrational excitation and de-excitation, relaxation of vibrationally excited states can also occur via collisions with I or I_2 (see for example [142, 143]).

3.4. Collisional processes between ions and neutrals

Following Phelps [144], ion-neutral elastic collisions can be considered to consist of isotropic and backward (or charge-exchange) scattering processes. We note however that for collisions between particles which have a different mass (such as I_2 and I^+ or I_2^+ and I), charge-exchange is no longer an elastic process as the ionization energy of the species differs. Thus, the reaction may be inelastic or even superelastic. Of the many possible ion-neutral collisional processes that exist in iodine plasmas, only a small number have been studied experimentally or theoretically, as summarized in table 9. Figure 24 shows the cross-sections for these processes as a function of the lab frame energy.

Various works, such as the book by Smirnov [145], provide approximate methods for calculating the charge-exchange cross-section from first principles quantum mechanics. Smirnov also provides representative cross-sections for many atomic elements in the periodic table, including iodine, where the reaction $I + I^+ \longrightarrow I^+ + I$ has a cross-section between about 10 and 20×10^{-19} m^2 and a threshold energy of 0 eV. Dressler *et al* [21] calculated charge-exchange cross-sections for $I + I^+ \longrightarrow I^+ + I$ at lab frame

Table 10. Example charged particle collisional processes. A negative threshold energy indicates an exothermic reaction with energy release.

ID	Reaction	Process	Threshold energy (eV)
E1	$I^{n+} + e^- \longrightarrow I^{(n+1)+} + 2\,e^-$	Ion ionization	—
E2	$I^+ + I^- \longrightarrow 2\,I(^2P^\circ_{3/2})$	Recombination	−7.39
E3	$I_2^+ + I^- \longrightarrow 3\,I(^2P^\circ_{3/2})$	Recombination	−4.71
E4	$I_2^+ + e^- \longrightarrow I(^2P^\circ_{3/2}) + I^+ + e^-$	Ion dissociation	2.68
E5	$I_2^+ + e^- \longrightarrow 2I(^2P^\circ_{3/2})$	Dissociative recombination	−8.27
E6	$I^- + e^- \longrightarrow I(^2P^\circ_{3/2}) + 2\,e^-$	Detachment	3.059

energies between 10 and 1000 eV using a corrected one-electron treatment based on a linear combination of atomic orbitals model. These cross-sections are compared with those from Smirnov in figure 24 where reasonable agreement is seen.

Hause *et al* [146] measured cross-sections for the charge-exchange reaction $I_2 + I^+ \longrightarrow I_2^+ + I$ (which is an exothermic reaction releasing 1.14 eV of energy), as well as total cross-sections for the sum of this reaction and $I_2 + I^+ \longrightarrow 2\,I + I^+$ (with a threshold energy of 1.542 eV), using a guided-ion beam technique. In particular, cross-sections were estimated using a beam attenuation method (expected to provide an upper cross-section limit) and a time-of-flight method (expected to give a lower cross-section limit). Experiments were performed for lab frame energies from around 0.67 eV to almost 300 eV. Individual cross-sections were also measured for the charge-exchange reaction $I_2 + I_2^+ \longrightarrow I_2^+ + I_2$ (with a threshold energy of 0 eV) and the collision induced dissociation reaction $I_2 + I_2^+ \longrightarrow I^+ + I + I_2$ (with a threshold energy of 2.68 eV). Measured cross-sections for the above reactions are provided in figure 24(b). All atomic and molecular iodine products are in their respective ground states. An empirical cross-section was proposed by Hause *et al* for the reaction $I_2 + I^+$ at high energies (above about 100 eV) and which is given by

$$\sigma_{I_2-I^+} = A - B\ln\varepsilon, \tag{24}$$

where $A = 66.0 \times 10^{-20}\ \mathrm{m}^2$, $B = 4.7 \times 10^{-20}\ \mathrm{m}^2$, and ε is the lab frame energy in units of (eV). The above empirical cross-section is similar in form to the Sakabe-type cross-section [147] which was used by Choi [148] to fit the cross-sections by Hause *et al* at high energies.

For ion-neutral collisional processes where no information is available, one may reasonably refer to approaches used for other diatomic gases such as chlorine [149, 150] and oxygen [151]. Here, the scattering cross-section is typically assumed to be half the value of the charge-exchange cross-section. Due to a lack of data, cross-sections for the scattering of negative ions with iodine atoms and molecules is assumed to be the same as those for positive ion scattering. However, as highlighted by Karmohapatro [152] in chlorine plasmas, the resonant charge-exchange cross-section is in fact higher for negative ions than for positive ions, so this simplified approach requires care.

3.5. Collisional processes between charged particles

In addition to collisions between charged particles and neutrals, there can also be collisions between charged particles themselves. Aside from Coulomb collisions (which are not specific to iodine), relevant collisional processes include electron impact excitation and ionization of ions (see also section 3.2), as well as recombination of positive and negative ions. Table 10 lists possible charged particle reactions with several important reactions subsequently discussed in further detail in the subsections below. For convenience (and due to a lack of data), we do not treat electron–ion excitation/de-excitation, nor ion–ion excitation/de-excitation or ionization.

3.5.1. Ion ionization

While direct multiple ionization processes were discussed in section 3.2.2, ionization processes involving electron impact ionization of ions themselves may also be relevant

$$I^{n+} + e^- \longrightarrow I^{(n+1)+} + 2\,e^-, \tag{25}$$

where $n \geqslant 1$ with n an integer. Since the electron temperature in some electric propulsion systems can be above 10 eV, ionization leading to I^{2+} and I^{3+} may be significant in some discharges. Indeed, experimental measurements in the plume of an iodine-fueled Hall thruster [153] have observed small fractions of I^{2+}. Experimental measurements or theoretical calculations of ionization cross-sections of ionic states are however not known.

3.5.2. Ion–ion recombination

In several previous works, such as Grondein *et al* [71], the only reaction process considered for the loss of I^- was via recombination with I^+ (to produce two iodine atoms) or I_2^+ (to produce an iodine atom and a molecule). Rate coefficients were respectively obtained from Yeung [154] and Greaves [155] and were assumed to be constant:

$$K_{\mathrm{rec},\,I^+-I^-} = 9.311\times10^{-15}\quad \mathrm{m^3\ s^{-1}},$$

$$K_{\mathrm{rec},\,I_2^+-I^-} = 1.22\times10^{-13}\quad \mathrm{m^3\ s^{-1}}.$$

The above rate coefficients were also later used by Lucken [97] and Marmuse [98]. However, subsequent investigations have shown that these values are likely not correct for several reasons. Firstly, Yeung [154] did not explicitly mention which recombination process was being studied and both positive and negative iodine ions were assumed to be molecular (i.e. I_2^+ and I_2^-): as suggested by Spencer-Smith's early work on iodine discharges in 1935 [156] where I_2^+ and I_2^- were found to be the most dominant ions. Secondly, Greaves [155] later repeated the experiment of Yeung and concluded that there may have been a fault with one of the amplifiers originally used resulting in an underestimation by a factor of 10. Mass spectrometry measurements also determined that the dominant ion species were I_2^+ and I^- (which had also been demonstrated in 1928 by Hogness and Harkness [82]). Greaves also measured rate coefficients for pressures between 4 and 133 Pa, and gas temperatures between 296 and 338 K. Overall, the rate coefficient increases with pressure and the measured value at 4 Pa and 296 K is $K_{\mathrm{rec},\,I_2^+-I^-} = 5.8\times10^{-14}\ \mathrm{m^3\ s^{-1}}$: a value roughly half of that used by Grondein *et al*. Based on the above factors, and considering similar recombination reactions used in chlorine plasma models [150], reasonable empirical rate coefficients are

$$K_{\mathrm{rec},I^+-I^-} = K_{\mathrm{rec},I_2^+-I^-} = 5\times10^{-14}\sqrt{\frac{300}{T_g}}\quad \mathrm{m^3\ s^{-1}}, \tag{26}$$

where T_g is the gas temperature in units of (K) and the rate coefficients for both recombination reactions are assumed equal. The dependence on gas temperature is an assumption informed by theoretical considerations related to the integration of a cross-section proportional to $1/\varepsilon$ over a Maxwellian distribution [157]. Again in analogy with chlorine plasmas [150], the reaction products depend on the reaction type: i.e. $I^+ + I^-$ leads to two iodine atoms, while $I_2^+ + I^-$ leads to three iodine atoms (as opposed to one atom and one molecule; see table 10). This hypothesis has been confirmed in private discussions with Nicolas Sisourat and his team at the Laboratory of Physical Chemistry-Matter and Radiation (LCPMR) in France who carried out preliminary experiments at the Double ElectroStatic Ion Ring ExpEriment (DESIREE) at Stockholm University in Sweden.

Recently, Poline *et al* [137] studied the recombination of I^+ and I^- at the DESIREE facility and showed that the reaction products are two iodine atoms either in the $I(^2P^\circ_{3/2})$ ground state (40%), or with one of the atoms in the $I(6s\ ^2[2])$ excited state (60%). No significant variation of the branching ratio was observed over the studied energy range between 0.1 and 0.8 eV. The total recombination cross-section (including all reaction pathways) is estimated to be of the order of $10^{-17}\ \mathrm{m^2}$ at an energy of 0.1 eV. Initial cross-section calculations have been performed at LCPMR and are presented in figure 25(a). Here, the cross-section depends on the reaction products with $I(^2P^\circ_{3/2}) + I(6s)$ being the most probable, and where I(6s) designates a highly excited 6s Rydberg state. The corresponding rate coefficients (assuming a Maxwellian distribution) are shown in figure 25(b). The sum of individual rate coefficients is given by the dashed line which is seen to be in quite close agreement with the empirical relation from equation (26) between 0.1 and 1 eV. While different reaction products are possible, the broad assumption of only ground-state atomic iodine (as in table 10) seems practical and reasonable if excited states are not of interest or being tracked in a given plasma model.

3.5.3. Electron–ion scattering

Aside from electron impact ionization of ions (see section 3.2), three additional reaction processes may be important in iodine plasmas: electron impact dissociation of I_2^+, electron impact dissociative recombination of I_2^+, and electron impact detachment of I^-. No known data for dissociative recombination exists, but cross-sections have been calculated by Hamilton [30] for ion dissociation and detachment and are shown in figure 26. No other data is available and these cross-sections have previously been used by Lucken [97] and Marmuse [98]. The dissociation threshold energy is estimated to be 2.68 eV. The energy resolution of the detachment cross-section is only 1 eV and the first non-zero value occurs at 4 eV. The

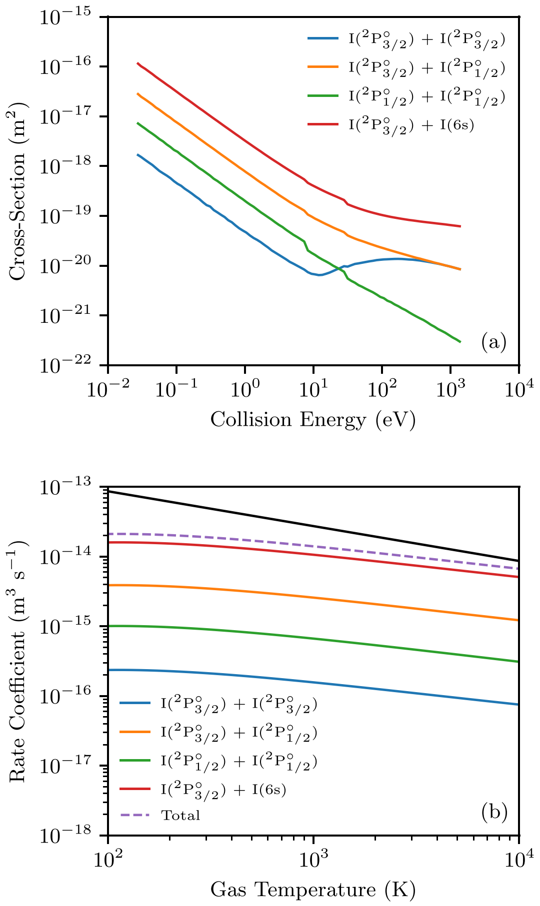

Figure 25. (Generalization of reaction E2 in table 10 accounting for several possible atomic products; see main text) (a) cross-sections and (b) rate coefficients for the recombination of I^+ and I^- as a function of energy. I(6s) designates a highly excited 6s Rydberg state. In (b), the dashed line denotes the sum of the individual rate coefficients, while the black line shows the empirical relation from equation (26).

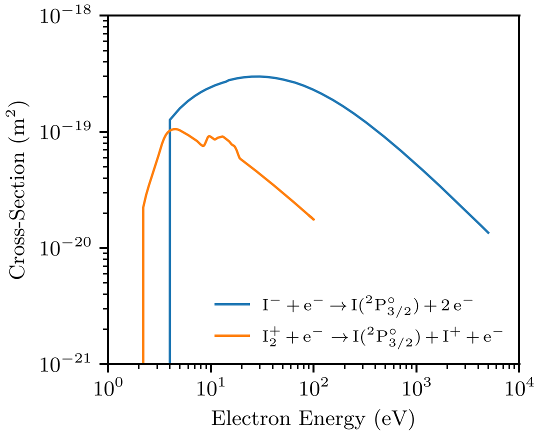

Figure 26. (Reactions E4 and E6 in table 10) Cross-sections for the electron impact dissociation of I_2^+, and the electron impact detachment of I^-.

electron affinity of iodine has however been precisely measured as 3.059 0463 eV [135]. Some uncertainty exists with the detachment cross-section as it is roughly an order of magnitude higher than that for chlorine [158], yet the photodetachment cross-section is of a similar magnitude. Plasma modeling by Esteves [26] noted that better agreement with experiment was obtained if detachment was ignored, again suggesting that the detachment cross-section may be too high.

Table 11. Example neutral-neutral collisional processes. A negative threshold energy indicates an exothermic reaction with energy release.

ID	Reaction	Process	Threshold energy (eV)
F1	$I_2 + I(^2P^\circ_{3/2}) \longrightarrow I_2 + I(^2P^\circ_{3/2})$	Elastic scattering	—
F2	$I_2 + I(^2P^\circ_{1/2}) \longrightarrow I_2 + I(^2P^\circ_{1/2})$	Elastic scattering	—
F3	$I(^2P^\circ_{3/2}) + I(^2P^\circ_{1/2}) \longrightarrow 2I(^2P^\circ_{3/2})$	Quenching	−0.9426
F4	$I_2 + I(^2P^\circ_{1/2}) \longrightarrow I_2 + I(^2P^\circ_{3/2})$	Quenching	−0.9426

3.6. Collisional processes between neutral particles

Aside from thermal dissociation reactions (see section 2.4), other important collisional processes between neutral particles include elastic scattering and quenching of excited states, which are illustrated in table 11. While elastic scattering of neutrals is not typically included or required in many plasma models, it can be important for iodine as it represents an energy exchange mechanism between atoms and molecules that is relevant to gas heating. At the low pressures of interest for several propulsion and industrial applications, elastic collisions appear insufficient for thermalization to a common temperature. Consequently, iodine atoms and molecules can have very different temperatures with the atomic temperature typically higher than the molecular temperature [26]. Similarly, while collisional quenching of excited states can occur in any plasma discharge, it may be more important in iodine because of the low excitation threshold energy of the $I(^2P^\circ_{1/2})$ excited state. As this state is metastable, collisional quenching represents an important depopulating process.

3.6.1. Elastic scattering

Elastic collisions between neutral particles can be approximated with a binary collision model accounting for the relative velocity between colliding species. Following Benilov [159, 160], particles are treated as hard spheres with a MTCS for collisions of I with I_2 given by

$$\sigma_{I-I_2} = \frac{\pi}{4}\left(d_I + d_{I_2}\right)^2, \tag{27}$$

where $d_I \approx 280$ pm and $d_{I_2} \approx 560$ pm are the atom and molecule diameters respectively, which gives $\sigma_{I-I_2} \approx 5.5 \times 10^{-19}$ m^2. Integrating over an assumed Maxwellian distribution, the rate coefficient is

$$K_{I-I_2} = \sigma_{I-I_2}\sqrt{\frac{k_B T_{I-I_2}}{2\pi m_{I-I_2}}}, \tag{28}$$

with

$$T_{I-I_2} = \frac{m_{I_2} T_I + m_I T_{I_2}}{m_I + m_{I_2}}, \tag{29}$$

$$m_{I-I_2} = \frac{m_I m_{I_2}}{m_I + m_{I_2}}, \tag{30}$$

the reduced temperature and mass respectively. The diffusion coefficient, which is relevant to the transport of atomic iodine to any surface bounding the plasma discharge, can be determined from

$$D_{I-I_2} = \frac{3\pi}{8}\lambda_{I-I_2} v_{I-I_2}, \tag{31}$$

where $\lambda_{I-I_2} = 1/(n_{I_2}\sigma_{I-I_2})$ is the collisional mean free path of I with n_{I_2} the I_2 density, and $v_{I-I_2} = \sqrt{2k_B T_{I-I_2}/(\pi m_{I-I_2})}$. Following the above reasoning, a similar diffusion coefficient can be defined for elastic collisions between $I(^2P^\circ_{1/2})$ and $I(^2P^\circ_{3/2})$.

The diffusion coefficient of atomic iodine was estimated by Brewer and Tellinghuisen [161] approximately fifty years ago using an atomic fluorescence technique. Assuming a constant *sticking probability* (γ; see section 4.2), Brewer *et al* proposed a value of $C = pD = 0.01$ Pa m^2 s^{-1}. This estimation leads to $\sigma_{I-I_2} \approx 1.06 \times 10^{-18}$ m^2 at room temperature. More recent measurements obtained by investigating the evolution of the atomic density generated by laser photodissociation of molecular iodine (for pressures between 3 and 30 Pa [162]) have instead yielded $C = 0.047 \pm 0.007$ Pa m^2 s^{-1}. This corresponds to $\sigma_{I-I_2} \approx 2.2 \times 10^{-19}$ m^2.

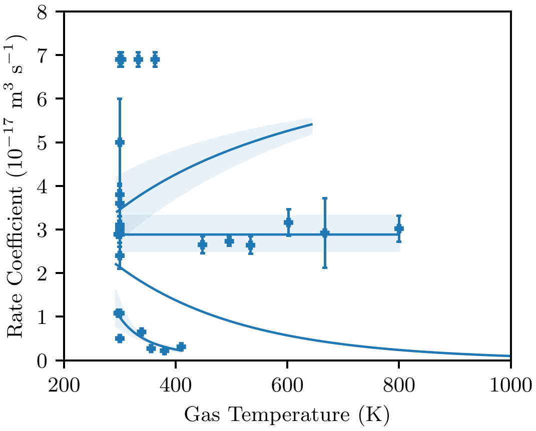

Figure 27. (Reaction F4 in table 11) Quenching rate coefficients of $I(^2P^\circ_{1/2})$ by I_2 as a function of gas temperature from Chichinin [163] (and references therein).

3.6.2. Quenching

The rate coefficients for the quenching of $I(^2P^\circ_{1/2})$ by I_2 have been compiled in a detailed work by Chichinin [163] and are shown in figure 27 (note that some of the data and temperature dependencies appear incorrect and were therefore retrieved directly from the original cited works [164–167]). At a temperature of 300 K, the quenching rate coefficient is measured to be between 3.3×10^{-18} and 7.07×10^{-17} m^3 s^{-1}, taking into account experimental uncertainties. The dependence on temperature is not clear and so until new data becomes available, assuming a constant rate coefficient seems practical. Performing a statistical analysis of the data around 300 K gives a mean rate coefficient of $K_{\text{quench}} = 3.13 \times 10^{-17}$ m^3 s^{-1} with a standard deviation of 1.08×10^{-17} m^3 s^{-1}. Quenching of $I(^2P^\circ_{1/2})$ by I_2 results in vibrationally excited $I_2^*(X, 25 \leqslant v \leqslant 43)$ [168]. Quenching of $I(^2P^\circ_{1/2})$ by $I(^2P^\circ_{3/2})$ is also discussed by Chichinin, but is found to be three orders of magnitude smaller than quenching with I_2, and so may be negligible in most cases.

3.7. Rate coefficients

While the reaction cross-sections provided in the sections above are directly usable for certain theoretical or numerical models (such as particle-in-cell (PIC) simulations), many fluid-based models instead require reaction rate coefficients. In this case, the cross-section data can be averaged over the particle distribution function. If this is not known, a Maxwellian distribution can be assumed, and for the electron impact processes in sections 3.2 and 3.3, the rate coefficient can be computed from

$$K_j = \frac{\bar{v}_e}{T_e^2} \int_0^\infty \sigma_j(\varepsilon)\, \varepsilon\, e^{-\varepsilon/T_e}\, d\varepsilon, \tag{32}$$

where $\bar{v}_e = \sqrt{8eT_e/(\pi m_e)}$ is the electron thermal speed with e and m_e the elementary charge and electron mass respectively, T_e is the electron temperature, and σ_j is the energy-dependent cross-section for reaction j. If required, cross-sections can be extrapolated at low and high energies to compensate for any missing data.

Using equation (32), rate coefficients for the main electron impact scattering processes can be determined for I and I_2 and are displayed in figure 28. Here, the different rate coefficient subscripts in the labels correspond to: total elastic scattering (el), elastic momentum transfer (elm), electronic excitation (exc), ionization (iz), dissociative ionization (dissiz), dissociation (diss), dissociative electron attachment (dissatt), and vibrational excitation (vibexc). For convenience, the correspondence of rate coefficient symbols and processes is provided in table 12, while atomic excitation processes have been grouped together using the lumped method discussed in section 3.2.3. Similarly, all molecular electronic and vibrational excitation processes have been grouped together into separate effective rate coefficients. The rate coefficients in figure 28 are also provided as supplementary data on the Zenodo repository [32]. Additionally, empirical fits for the main processes are provided in tables 13 and 14 using equations (33) and (34):

$$K(T_e) = \mathcal{A}\left[\ln\left(1 + \mathcal{B}T_e + \mathcal{C}T_e^2\right)\right]^{\mathcal{D}} \exp\left(-\frac{\mathcal{E}}{T_e}\right), \tag{33}$$

Table 12. Correspondence between rate coefficient symbols and processes. The lumped electronic excitation processes correspond to those listed in table 6.

Rate coefficient	Process
Electron impact scattering: atomic iodine	
$K_{\mathrm{el,I}}$	Total elastic scattering
$K_{\mathrm{el,I(^2P^\circ_{1/2})}}$	Total elastic scattering—$\mathrm{I(^2P^\circ_{1/2})}$
$K_{\mathrm{iz,I}}$	Ionization
$K_{\mathrm{iz,I(^2P^\circ_{1/2})}}$	Ionization—$\mathrm{I(^2P^\circ_{1/2})}$
K_{dexc}	De-excitation
$K_{\mathrm{exc_1,I}}$	Lumped electronic excitation 1
$K_{\mathrm{exc_2,I}}$	Lumped electronic excitation 2
$K_{\mathrm{exc_3,I}}$	Lumped electronic excitation 3
$K_{\mathrm{exc_4,I}}$	Lumped electronic excitation 4
Electron impact scattering: molecular iodine	
$K_{\mathrm{el,I_2}}$	Total elastic scattering
$K_{\mathrm{elm,I_2}}$	Elastic momentum transfer
$K_{\mathrm{iz,I_2}}$	Ionization
$K_{\mathrm{diss,I_2}}$	Dissociation
$K_{\mathrm{exc,I_2}}$	Electronic excitation
$K_{\mathrm{dissatt,I_2}}$	Dissociative attachment
$K_{\mathrm{dissiz,I_2}}$	Dissociative ionization
$K_{\mathrm{vibexc,I_2}}$	Vibrational excitation
$K_{\mathrm{rotexc,I_2}}$	Rotational excitation

$$K(T_\mathrm{e}) = A\exp\left(-\frac{B}{T_\mathrm{e}} + \frac{C}{T_\mathrm{e}^2} - \frac{D}{T_\mathrm{e}^3} + \frac{E}{T_\mathrm{e}^4}\right) T_\mathrm{e}^{-F}. \tag{34}$$

Rate coefficients for other processes, such as ion–ion recombination, are already provided in sections 3.5 and 3.6.

3.8. Collisional energy cost

A common and useful metric used to assess collisional power loss in plasma discharges is the collisional energy loss, $\mathcal{E}_\mathrm{c}$. This effectively represents the average energy expended to produce an electron–ion pair when considering relevant collisional processes (here only electron impact reactions). For molecular gases like iodine, a true energy loss is difficult to establish outside of a complete and comprehensive simulation where the balance between different species is accounted for. Nonetheless, an approximate order of magnitude computation can be made when assuming fully atomic or fully molecular iodine plasmas. For atomic iodine, the collisional energy loss can be defined by

$$\mathcal{E}_{\mathrm{c,I}} = \frac{1}{K_{\mathrm{iz,I}}}\left[K_{\mathrm{iz,I}}\varepsilon_{\mathrm{iz,I}} + \sum_j K_{\mathrm{exc}_j,\mathrm{I}}\varepsilon_{\mathrm{exc}_j,\mathrm{I}} + \frac{3m_\mathrm{e}k_\mathrm{B}}{m_\mathrm{I}}\left(T_\mathrm{e}-T_\mathrm{I}\right)K_{\mathrm{el,I}}\right], \tag{35}$$

which accounts for all collisional energy loss processes associated with ionization, excitation, and elastic scattering. Here, it is assumed that ground state atoms are the only species present. Similarly, the collisional energy loss for molecular iodine is

$$\begin{aligned}\mathcal{E}_{\mathrm{c,I_2}} = \frac{1}{K_{\mathrm{iz,I_2}} + K_{\mathrm{dissiz,I_2}}}\Bigg[&K_{\mathrm{iz,I_2}}\varepsilon_{\mathrm{iz,I_2}} + K_{\mathrm{dissiz,I_2}}\varepsilon_{\mathrm{dissiz,I_2}} + \sum_j K_{\mathrm{exc}_j,\mathrm{I_2}}\varepsilon_{\mathrm{exc}_j,\mathrm{I_2}} + \sum_j K_{\mathrm{vibexc}_j,\mathrm{I_2}}\varepsilon_{\mathrm{vibexc}_j,\mathrm{I_2}}\\ &+ \sum_j K_{\mathrm{rotexc}_j,\mathrm{I_2}}\varepsilon_{\mathrm{rotexc}_j,\mathrm{I_2}} + \sum_j K_{\mathrm{diss}_j,\mathrm{I_2}}\varepsilon_{\mathrm{diss}_j,\mathrm{I_2}}\\ &+ \frac{3m_\mathrm{e}k_\mathrm{B}}{m_{\mathrm{I_2}}}\left(T_\mathrm{e}-T_{\mathrm{I_2}}\right)K_{\mathrm{el,I_2}}\Bigg].\end{aligned} \tag{36}$$

Collisional energy loss processes include direct and dissociative ionization, electronic, vibrational, and rotational excitation, dissociation, and elastic scattering. Because of a lack of data, we assume that the electron dissociation energy loss is equal to the dissociation threshold energy of the molecular ground state, and rotational excitation processes are ignored. Equations (35) and (36) are plotted in figure 29

Table 13. Best-fit rate coefficients for various electron impact reaction processes for I and I_2 based on equation (33).

Rate Coef.	$\mathcal{A}$ (m^3 s^{-1})	$\mathcal{B}$ (eV^{-1})	$\mathcal{C}$ (eV^{-2})	$\mathcal{D}$	$\mathcal{E}$ (eV)	T_e (eV)	Error (%)
K_{iz,I_2}	1.20694×10^{-13}	-2.05557×10^{-3}	8.10106×10^{-2}	7.95734×10^{-1}	9.31000×10^{0}	[1 ; 50]	4.16
K_{diss,I_2}	1.94272×10^{-14}	1.65161×10^{-5}	-1.36170×10^{-7}	-6.05364×10^{-2}	2.92201×10^{0}	[1 ; 50]	8.91
K_{dissiz,I_2}	2.73612×10^{-14}	1.62507×10^{-1}	-9.69904×10^{-4}	9.41764×10^{-1}	1.19400×10^{1}	[0.5 ; 50]	6.74
$K_{dissatt,I_2}$	8.51271×10^{-18}	5.26610×10^{-6}	1.94777×10^{-7}	-5.57411×10^{-1}	2.94075×10^{0}	[2 ; 50]	17.22
K_{exc,I_2}	6.94179×10^{-18}	2.07908×10^{-6}	2.83839×10^{-9}	-6.91696×10^{-1}	4.63389×10^{0}	[1.5 ; 50]	3.48
K_{vibexc,I_2}	1.68131×10^{-19}	3.04258×10^{-4}	1.57137×10^{-4}	-8.01979×10^{-1}	1.41568×10^{0}	[0.5 ; 50]	3.46
$K_{iz,I}$	1.00526×10^{-13}	3.04247×10^{-1}	-1.87150×10^{-3}	1.02720×10^{0}	1.04500×10^{1}	[0.5 ; 50]	7.16
$K_{exc_2,I}$	9.91412×10^{-16}	7.39500×10^{-9}	1.81077×10^{-10}	-2.18520×10^{-1}	1.01082×10^{1}	[4 ; 50]	8.61
$K_{exc_3,I}$	1.10016×10^{-17}	-4.81093×10^{-10}	3.15998×10^{-9}	-4.89424×10^{-1}	1.17398×10^{1}	[2.5 ; 50]	8.93
$K_{exc_4,I}$	1.61045×10^{-16}	1.80686×10^{-9}	9.69122×10^{-11}	-3.49321×10^{-1}	1.09391×10^{1}	[2.5 ; 50]	13.34
$K_{iz,I(^2P^o_{1/2})}$	2.21512×10^{-13}	2.82764×10^{-1}	-1.72072×10^{-3}	1.03783×10^{0}	9.50740×10^{0}	[0.5 ; 50]	7.74
K_{dexc}	4.65222×10^{-16}	1.33736×10^{-8}	8.85358×10^{-10}	-2.72591×10^{-1}	1.56932×10^{-1}	[0.5 ; 50]	16.50

Table 14. Best-fit rate coefficients for various electron impact reaction processes for I and I_2 based on equation (34).

Rate Coef.	A ($m^3 s^{-1}$)	B (eV)	C (eV^2)	D (eV^3)	E (eV^4)	F	T_e (eV)	Error (%)
K_{el,I_2}	$4.132\,24 \times 10^{-13}$	$2.574\,31 \times 10^{-1}$	$4.185\,01 \times 10^{-2}$	$2.824\,20 \times 10^{-3}$	$6.560\,31 \times 10^{-5}$	$-3.702\,09 \times 10^{-1}$	[0.5 ; 50]	6.28
K_{elm,I_2}	$4.354\,60 \times 10^{-13}$	$-4.360\,57 \times 10^{0}$	$-1.329\,92 \times 10^{1}$	$-1.115\,29 \times 10^{1}$	$-2.920\,94 \times 10^{0}$	$-4.883\,06 \times 10^{-1}$	[1.5 ; 50]	8.06
$K_{el,I}$	$3.548\,63 \times 10^{-12}$	$5.503\,32 \times 10^{0}$	$6.217\,21 \times 10^{0}$	$2.873\,60 \times 10^{0}$	$4.674\,78 \times 10^{-1}$	$6.067\,88 \times 10^{-1}$	[0.5 ; 50]	7.51
$K_{exc_1,I}$	$8.996\,40 \times 10^{-14}$	$3.347\,29 \times 10^{0}$	$1.389\,34 \times 10^{0}$	$2.849\,49 \times 10^{-1}$	$7.487\,00 \times 10^{-3}$	$6.554\,18 \times 10^{-1}$	[0.5 ; 50]	8.87
$K_{el,I(^2P^o_{1/2})}$	$6.715\,48 \times 10^{-12}$	$8.961\,92 \times 10^{0}$	$8.422\,73 \times 10^{0}$	$3.608\,17 \times 10^{0}$	$5.733\,89 \times 10^{-1}$	$7.627\,52 \times 10^{-1}$	[0.5 ; 50]	6.28

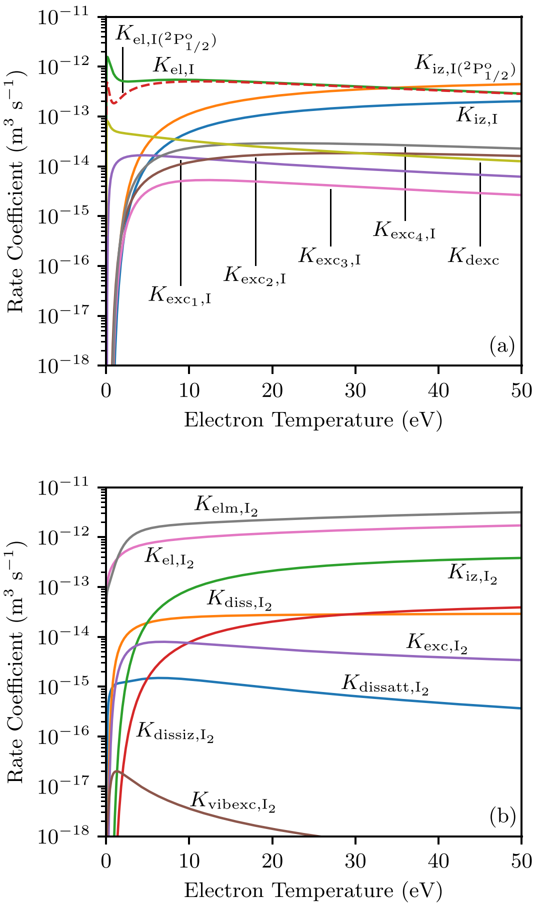

Figure 28. Rate coefficients as a function of electron temperature (assuming a Maxwellian distribution) for various collisional processes for (a) I and (b) I_2.

as a function of electron temperature (assuming a Maxwellian distribution function). For comparative purposes, results are also shown for the noble gases argon, krypton, and xenon. Here we see that the collisional energy loss in iodine is lower than the noble gases for temperature above about 4 eV. This important result indicates that iodine discharges are expected to be more energy efficient at sufficiently high temperatures. However, below 4 eV, the energy loss increases rapidly and far surpasses that of the noble gases. This is largely due to the very low threshold energy for excitation of the $I(^2P^\circ_{1/2})$ state.

Similar results are obtained for molecular iodine, where above a temperature of about 2 eV, the energy cost is lower than both atomic iodine and the noble gases. However, care is needed here as rotational excitation has been neglected, and the electron energy loss during dissociation is typically much higher than the dissociation threshold energy (being equal to the so called vertical excitation energy). Depending on the composition of an iodine discharge, the true energy cost is expected to lie somewhere between that for I and I_2. Regardless, we can already make a strong statement about iodine plasmas: for high-efficiency operation, conditions must be such that the electron temperature is higher than about 4 eV.

3.9. Electron swarm parameters

Due to the high reactivity of halogen gases (such as I_2), experimental investigations of electron swarm parameters are scarce. Most available studies have been conducted in gas mixtures where the halogen is diluted with a non-reactive, non-electronegative buffer gas. In such cases, the concentration of the electronegative component is typically low enough that the electron energy distribution and drift velocity are effectively assumed to be equal to those of the pure buffer gas.

To date, the only available data on the electron drift velocity in I_2 are the indirect measurements reported by Healey in 1938 [84], using a diffusion apparatus constructed from brass and platinum. As noted by Gallagher *et al* [132], these results are subject to significant uncertainty as the drift velocities were not measured directly but rather inferred from measurements in gas mixtures. The inferred values for I_2 are presented in figure 30 and compared with those for other halogens, such as chlorine (Cl_2)

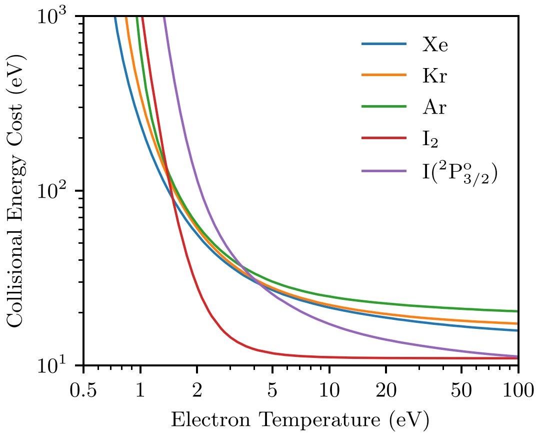

Figure 29. Average collisional energy cost per electron–ion pair as a function of electron temperature for atomic iodine, molecular iodine, argon, krypton, and xenon. In all cases, the gas temperature is 300 K.

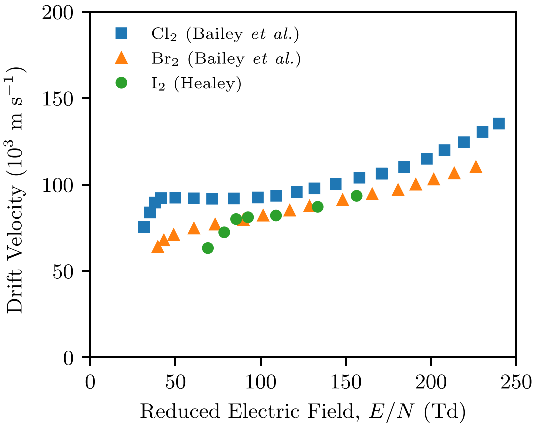

Figure 30. Drift velocity of electrons in Cl_2 (blue squares) [169], Br_2 (orange triangles) [170], and I_2 (green circles) [84] as function of the reduced electric field (E/N).

and bromine (Br_2), reported by Bailey *et al* [169, 170]. More recently, González-Magaña and De Urquijo [171] measured electron drift velocities in Cl_2 and found fair agreement with the data of Bailey *et al* to within about 12% for reduced electric fields (E/N, where E is the electric field magnitude, N is the gas density, and typical units are the Townsend (Td) with $1\ \mathrm{Td} = 10^{-21}\ \mathrm{V\,m^2}$) between 120 and 220 Td (not shown). It is important to emphasize that Healey's data, being the only measurements available for I_2, should be regarded as approximate.

The only reported data for the electron characteristic energy D_T/μ (i.e. the ratio of the transverse diffusion coefficient, D_T, to the mobility, μ) in I_2 also originate from Healey and Bailey *et al* [84, 169, 170], who employed a combined electric and magnetic field technique. Figure 31 presents the inferred values of D_T/μ as a function of the reduced electric field E/N in the range 0–250 Td. As noted by Gallagher *et al* [132], significant challenges were encountered in handling these highly reactive gases, which further complicate the interpretation of the results. Given the absence of additional measurements, this data should also be regarded as approximate.

Brooks *et al* [126] investigated the temperature dependence of the reduced electron attachment coefficient (η/N with η the attachment coefficient) in a mixture of 1% I_2 and 99% N_2 at 6.7 kPa using an electron swarm experiment, as a function of the reduced electric field E/N. This data, shown in figure 32, demonstrates a significant increase in the attachment coefficient with gas temperature, attributed to the thermal population of vibrationally excited states. In figure 32, it is important to note that while the attachment coefficient is referenced to the iodine partial density (i.e. $N = N_{I_2}$), the reduced electric field E/N corresponds to the density of the entire gas mixture. By varying the reduced electric field between 1 and 50 Td, Brooks *et al* modulated the mean electron energy between approximately 0.5 and 2.5 eV. Their results reveal a clear minimum in the attachment coefficient near 4 Td, suggesting the involvement of multiple resonant states for dissociative electron attachment.

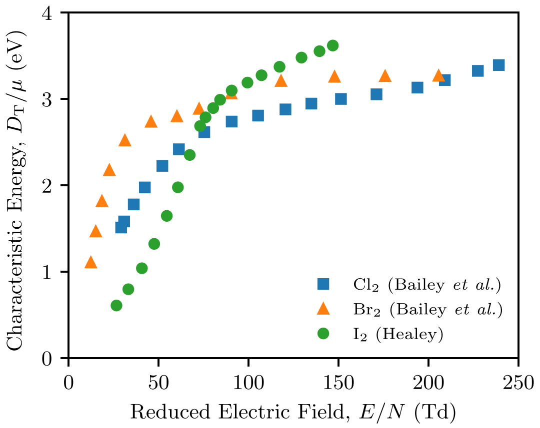

Figure 31. Characteristic energy of electrons in Cl_2 (blue squares) [169], Br_2 (orange triangles) [170], and I_2 (green circles) [84] as function of the reduced electric field (E/N).

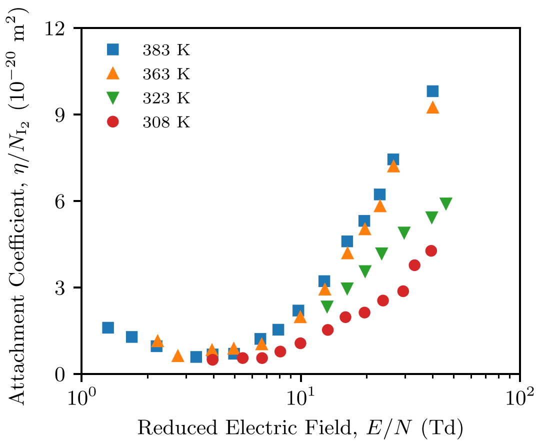

Figure 32. Reduced attachment coefficient (η/N_{I_2}) for 1% I_2 and 99% N_2 measured at different gas temperatures as a function of the reduced electric field (E/N) by Brooks *et al* [126]. The gas pressure is 6.7 kPa.

It should be highlighted that to date, no known studies have been reported in the literature on electron swarm analysis in pure atomic or molecular iodine. Nevertheless, such studies would be very valuable to reduce the large uncertainties in the electron impact total momentum transfer and dissociative electron attachment cross-sections as discussed above in sections 3.3.1 and 3.3.3.

4. Iodine-surface interactions

4.1. Material compatibility

As a halogen, iodine is quite reactive with many other substances. Having an electronic configuration of [Kr] $4d^{10}$ $5s^2$ $5p^5$, it lacks only a single electron to achieve a noble gas like stable configuration with a full valence shell. Although its electronegativity is lower than the lighter halogens (i.e. fluorine, chlorine, and bromine), it is still very high (2.66 on the Pauling scale). The iodine-iodine dissociation energy (1.54 eV) is also weak compared to that of other diatomic molecules which exist in stable states in nature (e.g. 9.79 eV for molecular nitrogen and 5.15 eV for molecular oxygen), which implies that less energy is required to chemically break the bond.

Iodine-material compatibility can be generally discussed by considering a reduced list of transition and post-transition metals, as well as certain non-metallic substances, for two main reasons. Firstly, cost and availability are important factors when selecting materials for space applications [172]. Secondly, structural rigidity and integrity are often of interest in design: particularly for containers, tanks, or fluidic elements in direct contact with iodine. Therefore certain metallic elements and their alloys are ignored here as they are extremely scarce or expensive. This includes, for example, ruthenium (Ru), dubnium (Db), seaborgium (Sg), bohrium (Bh), hassium (Hs), thallium (Tl), astatine (At), as well as the lanthanides and actinides. Similarly, metalloids and their alloys are also ignored, such as germanium

Table 15. Compatibility of iodine with various materials [173, 174].

Material	Reactivity
Metals	
Aluminum (6061)	Medium
Aluminum (7075)	Medium
Aluminum (anodized 7075)	Low
Chromium	Low
Copper (110)	High
Copper (C260 brass)	High
Gold	Low
Iron (4130 alloy steel)	High
Iron (304 stainless steel)	High
Iron (316 stainless steel)	Medium
Nickel (Hastelloy B-3)	Low
Nickel (Hastelloy C-22)	Low
Nickel (Hastelloy C-276)	Low
Nickel (Hastelloy C-2000)	Low
Platinum	Low
Titanium (pure)	Low
Titanium (Ti-6Al-4V)	Low
Tungsten	Low
Non-metals	
Boron nitride	Low
Silicon carbide	Low
Silicon nitride	Low
Zirconium oxide	Low

(Ge), arsenic (As), antimony (Sb), and tellurium (Te), with the exception of boron (B) and silicon (Si). Certain non-metallic substances, such as the noble gases, do not react under normal conditions with iodine, which is useful for some applications (e.g. to extend the lifetime of halogen lamps). These elements do not usually form solid compounds due to their chemical stability, and typically have very high saturation and melting temperature-pressure phase diagram characteristics.

Remaining substances can be divided into three main material categories: metallic pure elements and alloys (e.g. high-strength aluminum alloys like Al2024), ceramics (e.g. zirconium oxide, ZrO2) and polymers (e.g. polytetrafluoroethylene, PTFE). Establishing the chemical compatibility of iodine with every chemical compound is a complex task as the behavior of compound components (i.e. alloying elements) often differs from the behavior of the base elements. Nonetheless, an overview can be provided based on the existing literature, with table 15 providing a summary indicating the typical level of reactivity between iodine and various materials.

Naturally, alkali metals, which display a s^1 valence electron configuration (i.e. lithium to francium), are perfect electron donors for halogens and therefore show a strong chemical affinity with iodine. When reacting with iodine, alkali metals form metal iodides in a highly exothermic reaction, particularly between iodine and the heavier alkali metals like potassium (K), rubidium (Rb), and cesium (Cs). Similarly, alkaline Earth metals (beryllium to radium), which have a s^2 valence electron configuration, also display a strong affinity with halogens, although at a reduced level compared with the alkali metals.

Note however that the corrosion behavior of a substance does not solely depend on the chemical affinity of the material with iodine. Environmental conditions are equally important and can accelerate the corrosion and failure of the material. Notable factors which influence corrosion behavior include: (a) the phase of iodine (e.g. solid, liquid, or gas), (b) the temperature conditions (with higher temperatures typically causing higher corrosion), (c) the vapor pressure (in the case of corrosion by iodine gas, with higher gas densities typically leading to accelerated corrosion damage), (d) the state of the surface (pits or localized previous attack can remove the protective layer of certain materials, such as aluminum oxides), and (e) the presence of external ambient substances (e.g. water) or pollutant particles (e.g. metallic particles left from the machining/manufacturing process).

Aluminum, typically alloyed with other metallic substances like copper (Cu), zinc (Zn), or magnesium (Mg), generally offers poor resistance to continuous iodine exposure. While Craig and Anderson [175] note its resistance to solid iodine at ambient temperatures, Zschätzsch *et al* [176] and Martínez

Martínez and Rafalskyi [174] have reported localized attack that can easily be perceived under microscope observations.

Stainless steel suffers pitting even at ambient conditions [175], with apparent surface degradation and the formation of iron iodides. The corrosion of iron (Fe) and its alloys is particularly fast. Jerman [173] studied the corrosion of various substances under a 7 day 200 °C iodine flow test, measuring a corrosion rate of 1.055 mm yr^{-1} for A304 stainless steel, which was 3.7 times higher than that of an aluminum alloy (non-anodized Al7075), 25 times higher than that of a nickel alloy (Hastelloy C-276), and 28 times higher than that of pure titanium (Ti). Even if iron suffers strong corrosion, the remaining stainless steel constituents, such as manganese (Mn), chromium (Cr), and nickel (Ni) are also subject to iodine corrosion [177]. Copper similarly displays a strong chemical affinity for iodine, with a corrosion rate of 0.606 mm yr^{-1}. Other works note similar corrosion rates, but also report changes in the core properties of the metal, such as the thermal conductivity, as well as a 42% increase in DC resistance after the tests [174]. Tin (Sn) is also observed to be very susceptible to iodine corrosion [174].

Titanium is reported as moderately resistant at ambient temperatures and may offer certain protection to cold iodine, but is subject to stress corrosion cracking in hot iodine-rich environments [178]. Titanium alloys commonly used in aerospace applications (e.g. Ti6Al4V) may offer worse behavior than the base metal due to corrosion of some of the alloy constituents [173]. Zirconium (Zr) and its alloys, which are used in nuclear power reactors [179], are also subject to iodine corrosion and may suffer from stress corrosion cracking [178].

Iodine reacts with nickel largely to form NiI_2, which has a melting point of about 780 °C. Up to moderately high temperatures (around 100 °C), nickel offers a moderate resistance to iodine and displays limited chemical interaction [176], although it does already display moderate pitting. Fontana and Staehle [180] note that some Ni–Cr alloys (e.g. Inconel 600, Inconel 625, Inconel X-750, and Hastelloy C-276) are generally resistant to iodine [180], although Martínez Martínez and Rafalskyi [174] have highlighted that chromium and iron are present in these alloys and may be subject to localized pitting [174].

Refractory metals (e.g. molybdenum, Mo) offer satisfactory resistance to iodine corrosion and display very limited chemical reactivity at ambient or moderate temperatures [174, 176, 181]. Jerman [173] has however observed non-negligible corrosion of these metals under certain test conditions. For example, the corrosion rate of tantalum under iodine bath exposure at 200 °C was measured as 0.834 mm yr^{-1} [173]. This contradicts other research where corrosion rates of 0.004 mm yr^{-1} at 300 °C, and 0.88 mm yr^{-1} at 450 °C were observed. This again emphasizes the need to carefully set and control the test conditions to replicate the expected operating environment for a given application.

Literature on the corrosion of noble metals and silver (Ag) by iodine is more scarce. Silver and gold (Au) are reported to have a poor resistance to dry iodine by Craig *et al* [175], but these results appear to disagree with later work by Lai [182]. Platinum (Pt) has been used for iodine corrosion applications [183], with some information on measured corrosion rates: 0 mm yr^{-1} at 300 °C and 0.0055 mm yr^{-1} at 450 °C [182]). Iridium (Ir) and ruthenium (Ru) have low corrosion rates (less than 0.003 mm yr^{-1} [175]), but this has only been measured at ambient temperatures (approximately 22 °C). Craig and Anderson [175] also report extended corrosion for osmium (Os). No corrosion rates are given for palladium (Pd) or rhodium (Rh).

Ceramic materials are typically stable and do not display pitting damage. Boron nitride (BN) shows good compatibility with iodine and no evidence of surface attack [174]. Other ceramic materials, such as silicon carbides/nitrides (SiC and Si_3N_4), zirconium oxide (ZrO_2), mica, or Macor show no growth of defects or changes in weight after iodine exposure [174]. Silicate or borosilicate glasses, as amorphous, ceramic-like substances, display very little chemical interaction with iodine, with no surface etching or pitting under extended exposure [173].

Polymeric materials, such as Teflon, Viton, or Kapton, typically have stable corrosion behavior, but may become subject to weakening or changes in volume under certain test conditions, with evidence of shrink or swell. Jerman [173] has reported non-negligible corrosion rates for Teflon (0.219 mm yr^{-1}), Viton (0.24 mm yr^{-1}), and Kapton (0.125 mm yr^{-1}) under a 7 day 200 °C iodine bath test.

Finally, some ceramic coatings (e.g. tantalum pentoxide, Ta_20_5) have been found to protect metallic surfaces exposed to iodine [174]. However, it is noted that iodine can grow on surface defects, or attack the base material, causing the ceramic protective layer to crack and expose further sections of the underlying element. Care needs to be taken when handling iodine with ceramics, glasses, polymeric materials, or in general substances with a low thermal conductivity, as iodine flows may deposit. Even if corrosion is not observed, lack of heating may lead to blockages or other issues [27].

A further discussion exploring the compatibility of materials with iodine is available across a range of relevant studies. For example, a foundational investigation is the 1990 doctoral thesis of Mathieu and

Table 16. List of measured or inferred surface recombination coefficients obtained from the literature.

γ_{wall}	Surface	Comments
0.001–0.01	Acid-coated surfaces [188]	With plasma
0.07	Alumina [28]	With plasma
0.05–0.2	Aluminum [26]	With plasma
0.001–0.065	Quartz [26, 161]	With plasma
0.05–0.25	Quartz [162]	Without plasma
0.14	BK7 glass [189]	Without plasma
0.014	Dimethyldichlorosilane [189]	Without plasma

references therein [184], which, although focused on the behavior of iodine in nuclear reactor environments, provides valuable baseline data on iodine-induced corrosion phenomena. For similar applications, but at the molecular level, Beck *et al* [185] investigated iodine interactions with Fe, Ni, Cr, and stainless steel alloys, offering mechanistic insight into material degradation. In the aerospace context, Guidi *et al* [181] recently examined the reactivity of iodine with various materials commonly used in spacecraft. Complementing this, Costa *et al* [186] reported chemical, structural, and microstructural changes in metallic and silicon-based coatings exposed to iodine vapor. Holste *et al* [187] have also identified material compatibility as a central challenge in advancing iodine-based ion thruster technologies. Finally, Zschätzsch *et al* [176] proposed an accelerated testing methodology based on the constant $p\Delta t$ concept, whereby increased iodine vapor pressure over short durations replicates long-term exposure by maintaining a constant product of pressure and time (proportional to the total number of iodine–material interactions).

Interestingly, despite iodine's well-known corrosive properties described above, its use under vacuum conditions appears to pose a somewhat limited risk of severe degradation for many materials initially considered poorly compatible (e.g. stainless steel or aluminum). In the absence of moisture and at low partial pressures, the reactivity of iodine is significantly reduced, and observed material damage is often superficial or self-limiting. This suggests that, for a wide range of aerospace-relevant substrates, iodine can be safely handled in vacuum environments without inducing critical structural or functional failure.

4.2. Surface recombination of atomic iodine

As discussed in sections 2.4 and 3.3, thermal and electron impact dissociation processes lead to the formation of atomic iodine, which can later recombine via the following general surface reaction (applicable to both ground and excited atomic states)

$$\mathrm{I} + \mathrm{I} \longrightarrow \mathrm{I}_2. \tag{37}$$

The recombination probability can be described by the *sticking probability* or *surface recombination coefficient*, γ_{wall}, which varies between 0 and 1. The flux of atomic iodine to a surface can then be expressed as

$$\Gamma_{\text{wall,I}} = \frac{1}{4} n_{\text{I}} \bar{v}_{\text{I}} \left(\frac{2\gamma_{\text{wall}}}{2 - \gamma_{\text{wall}}} \right), \tag{38}$$

where n_{I} and $v_{\text{I}} = \sqrt{8 k_{\text{B}} T_{\text{I}} / (\pi m_{\text{I}})}$ are the atomic iodine density and thermal speed respectively. The surface recombination coefficient plays a key role in most, if not all, iodine discharges because it directly affects the balance between collisional volume dissociation and surface recombination processes. In general, the surface recombination coefficient depends on the surface material, state (e.g. surface roughness, concentration of chemisorbed or physiosorbed contaminant atoms, surface defect structures, etc), and temperature, and thus is not in general a constant but can vary with discharge conditions. Indeed, recent measurements with atoms produced by photodissociation [162] have shown a variation of the recombination coefficient between 0.25 and 0.05 (for a quartz surface) when the pressure varies from 3 to 30 Pa. For other more well-studied molecular gases, such as chlorine, the recombination coefficient can vary from as low as 0.01 for silicon surfaces at room temperature, to as high as 0.85 for stainless steel. Detailed and accurate data for iodine is sparse, although several experiments have previously measured the surface recombination coefficient for various materials, as summarized in table 16.

For numerical modeling (see section 5.3), the surface recombination coefficient plays a role in diffusional loss processes to any bounding surfaces, which can be described by an effective rate coefficient given by

$$K_{s-s'} = \left[\frac{\Lambda_0^2}{D_{s-s'}} + \frac{4V}{\bar{v}_{s-s'}A_s}\left(\frac{2-\gamma_{\text{wall}}}{2\gamma_{\text{wall}}}\right)\right]^{-1}. \tag{39}$$

Here V is the plasma volume, A_s is the surface area bounding the plasma, $\bar{v}_{s-s'} = \sqrt{8k_B T_{s-s'}/(\pi m_{s-s'})}$ is the thermal speed with the s and s′ subscripts indicating either atomic or molecular iodine species, $D_{s-s'}$ is the relevant diffusion coefficient (see section 3.6), and for a cylindrical discharge, the diffusion length is given by [124]

$$\Lambda_0 = \left[\left(\frac{\pi}{L}\right)^2 + \left(\frac{\chi_{01}}{R}\right)^2\right]^{-1/2}, \tag{40}$$

with L and R the length and radius of the discharge, and $\chi_{01} \approx 2.405$ the first zero of the zeroth order Bessel function of the first kind.

4.3. Secondary electron emission (SEE)

An important plasma-surface process is the emission of electrons due to bombardment by photons and neutral/charged particle species [190]. Referred to as SEE, this process plays a critical role in sustaining DC discharges [191, 192], can influence plasma-wall losses in Hall thrusters [193], modifies electron heating and ionization dynamics in capacitively coupled plasmas (CCPs) [194, 195], and can even affect the operation of electrostatic probe diagnostics [196–198]. Electron- and photon-induced SEE are expected to remain similar in iodine plasmas (although the surface state may change due to deposition and specific photon energies will depend on the various excited iodine states), while neutral- and ion-induced SEE will be a function of the different atomic and molecular species present, and their energy. The current of emitted electrons is quantified by the emission yield, γ_{see}, which is defined as

$$\gamma_{\text{see}} = \frac{I_{\text{see}}}{I_i}, \tag{41}$$

where I_i is the ion beam (or equivalent neutral beam) current incident on the surface, and I_{see} is the current of secondary electrons emitted. Emission yield data for iodine ion and neutral bombardment is very sparse in the literature. In addition, the molecular nature of iodine complicates experimental measurements as multiple positive ion species (primarily I^+ and I_2^+) are typically formed in iodine discharges (see section 3). A further complication is the chemical reactivity of iodine, which can lead to the deposition of iodine or the formation of iodide layers. Thus, the effective emission yield may change in time and differ from that for atomically clean surfaces.

Dedicated measurements of ion-induced SEE yields have been performed by Habl *et al* [199] for energies between 0.6 and 1.4 keV (a range relevant to many electric propulsion systems) and for different target materials including: aluminum (Al), carbon–carbon (CC), copper (Cu), molybdenum (Mo), steel, titanium (Ti), and tungsten (W). Experiments were performed with an iodine-fueled gridded ion thruster that was repurposed to act as an ion source, and the fraction of atomic and molecular ions in the beam was determined using time-of-flight spectrometry. By varying the input power to the ion source, the ratio of atomic-to-molecular ion beam current could be varied. Although filtering of neutral iodine species was not possible, the collisional mean free path was estimated to be about 7 m, such that fast neutrals should only account for a small fraction (∼7%) of the incident beam. Emission yields were inferred from the current–voltage characteristics of an electrostatic probe placed downstream of the ion source, and whose collector surface was composed of the target material. Because of the polarity of the probe, both electrons and negative ions are reflected and prevented from entering the probe. Results are shown in figure 33 for two different ion source power levels (which give atomic-to-molecular ion beam current ratios of approximately 50:50 and 75:25 respectively).

The highest emission yields are obtained with Al and Cu, while CC, Mo, and W give the lowest yields. Since the emission yield varies linearly for some materials (such as Al and Ti), kinetic emission processes likely dominate over Auger emission [124]. Overall, ion beam composition only plays a minor role for SEE from Al, CC, Mo, Ti, and W, but appears to play a significant role for Cu and steel: most likely due to the formation of a thin iodide layer as these materials are known to be reactive with iodine (see section 4.1). Although detailed surface modification studies were not conducted, previous work with oxygen and nitrogen beams have demonstrated that the formation of oxide and nitride layers affects the emission yield [200–203]. As these layers are continually formed and sputtered, the SEE yield obtained is therefore an effective value representative of the original surface material and the compound layer. As

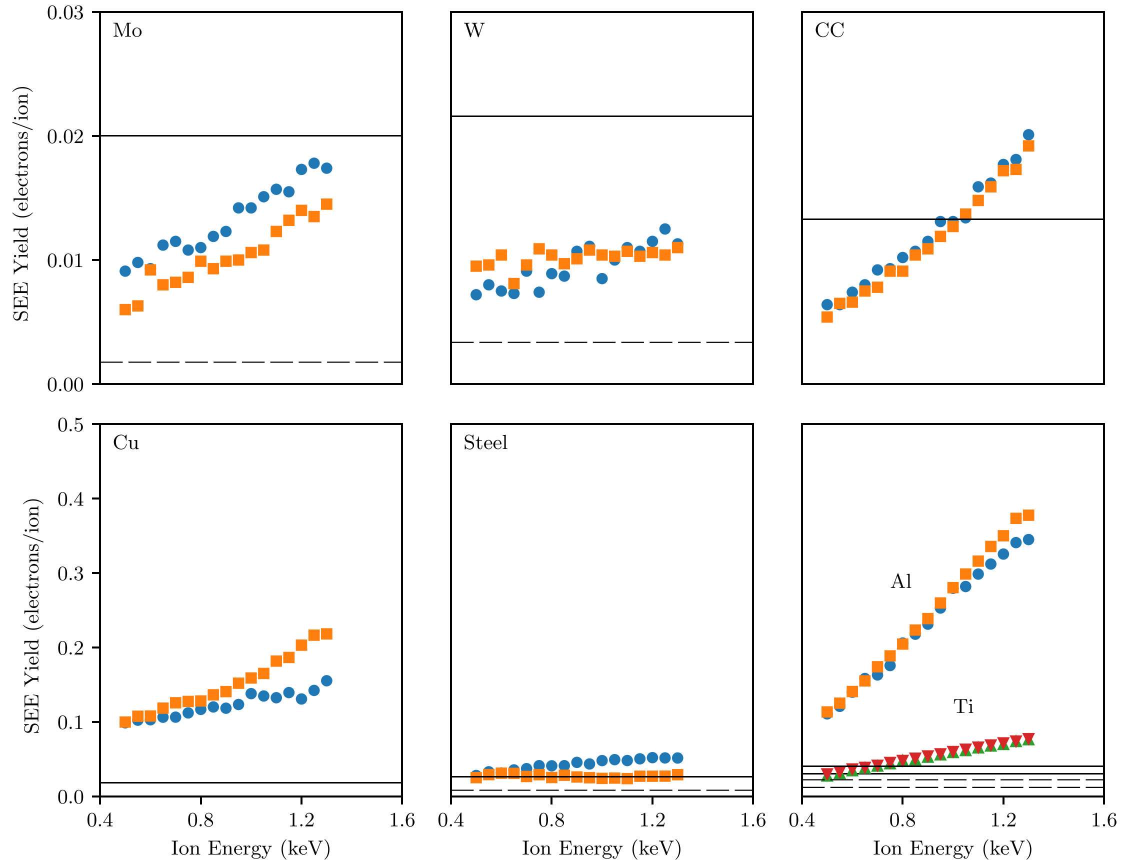

Figure 33. Secondary electron emission yields for iodine ion bombardment of different target surfaces and for two atomic-to-molecular ion beam current ratios (blue circles or green up triangles for 50:50 and orange squares or red down triangles for 75:25). The horizontal solid and dashed lines show the emission yield from equation (42) for I^+ and I_2^+ respectively. Data taken from [199]. Error bars have been omitted for clarity but are typically less than ±20%.

surface modification is expected to anyway occur in any real device, the effective emission yield obtained may well be more accurate than that obtained for a 'clean' surface.

As no measurements were performed at low energies, and in the absence of any other available data, the approximate empirical expression from Raizer [204] can be used to obtain an estimate of the SEE yield due to Auger emission

$$\gamma_{\mathrm{see}} \approx 0.016\left(\varepsilon_{\mathrm{iz}} - 2\varepsilon_{\phi}\right), \tag{42}$$

with $\varepsilon_{\mathrm{iz}}$ the ionization threshold of the ion and ε_{ϕ} the work function of the target material, with both in units of (eV). Comparison with more detailed theoretical emission models show that equation (42) is quite reasonable [205]. As an example, equation (42) is applied to the target materials in figure 33 and predicted emission yields are shown as the horizontal solid and dashed lines, and given in table 17. As seen, the estimated SEE yield is mostly consistent with the low energy values obtained experimentally.

4.4. Sputter erosion

An important consideration in both electric propulsion and materials processing is sputter erosion of materials or components. Here, high-energy ions striking a target can physically remove atoms leading to gradual surface erosion with time. For example, ion-neutral collisions in gridded ion thrusters can lead to a loss of ion focusing through the acceleration grids, and the generation of a backstreaming ion current [3]. This causes high-energy ions to strike the downstream acceleration grid (typically referred to as the accel grid) leading to sputter erosion of grid surfaces (so called 'pits and grooves' erosion), or enlargement of the grid apertures (known as 'barrel' erosion). This erosion produces a degradation in thruster performance and eventually complete failure. Similarly, erosion of neutralizers is a concern, while sputter erosion rates are typically important in certain plasma etching applications. For ions incident on a flat surface, the erosion rate is given by

$$\frac{\mathrm{d}h}{\mathrm{d}t} = \frac{m_{\mathrm{s}}\Gamma_{\mathrm{i}}f_{\mathrm{c}}Y}{\rho_{\mathrm{s}}}, \tag{43}$$

Table 17. Representative secondary electron emission yields due to Auger emission obtained from equation (42). Here $\varepsilon_{\mathrm{iz,I}} = 10.451$ eV and $\varepsilon_{\mathrm{iz,I_2}} = 9.31$ eV.

Target	ε_ϕ (eV)	Ion	γ_{see}
Al	4.28	I^+	0.030
		I_2^+	0.012
CC	4.81	I^+	0.013
		I_2^+	≈ 0
Cu	4.65	I^+	0.018
		I_2^+	≈ 0
Mo	4.60	I^+	0.020
		I_2^+	0.002
Steel	4.40	I^+	0.026
		I_2^+	0.008
Ti	3.96	I^+	0.040
		I_2^+	0.022
W	4.55	I^+	0.022
		I_2^+	0.003

where h is the dimension perpendicular to the surface, m_{s} is the atomic/molecular mass of the surface material, ρ_{s} is the mass density of the surface material, Γ_{i} is the incident ion flux, $Y = Y(\varepsilon_{\mathrm{i}})$ is the *sputter yield* at perpendicular incident and which is a function of the ion bombarding energy ε_{i}, and f_{c} is a correction factor accounting for ions that strike the surface at an oblique angle. The sputter yield can be defined as

$$Y = \frac{\Gamma_{\mathrm{a}}}{\Gamma_{\mathrm{i}}}, \tag{44}$$

with Γ_{a} the flux of atoms removed. Sputter yields have been calculated or measured for many different bombarding ion and target elements [206–208], including for oblique ion incidence [209, 210]. Within an electric propulsion context, xenon ions striking metal surfaces like molybdenum have been particularly well studied [211–213], as molybdenum has a low sputter yield compared with other materials (such as copper for example) and so is well-suited for acceleration grids. Figure 34 shows a range of experimental data for perpendicular incidence of singly-charged xenon ions striking a molybdenum surface [214], together with an empirical fit based on Eckstein's formulation [214, 215]

$$Y = Q s_{\mathrm{n}} \left[\frac{\left(\frac{\varepsilon_{\mathrm{i}}}{\varepsilon_{\mathrm{th}}} - 1 \right)^{\mu}}{\frac{\lambda}{w} + \left(\frac{\varepsilon_{\mathrm{i}}}{\varepsilon_{\mathrm{th}}} - 1 \right)^{\mu}} \right], \tag{45}$$

where $Q = 18.4$, $\varepsilon_{\mathrm{th}} = 14.2$ eV, $\mu = 2.2$, $\lambda = 1.7$, and

$$s_{\mathrm{n}} = \frac{0.5 \ln\left(1 + 1.2288\beta\right)}{\beta + 0.1728\sqrt{\beta} + 0.008\beta^{0.1504}}, \tag{46}$$

$$w = \beta + 0.1728\sqrt{\beta} + 0.008\beta^{0.1504}, \tag{47}$$

$$\beta = \frac{a_{\mathrm{L}}}{Z_{\mathrm{i}} Z_{\mathrm{s}}} \frac{4\pi\epsilon_0}{e^2} \frac{m_{\mathrm{s}}}{m_{\mathrm{i}} + m_{\mathrm{s}}} \varepsilon_{\mathrm{i}}, \tag{48}$$

$$a_{\mathrm{L}} = \left(\frac{9\pi^2}{128} \right)^{1/3} a_0 \left(Z_{\mathrm{i}}^{2/3} + Z_{\mathrm{s}}^{2/3} \right)^{-1/2}. \tag{49}$$

Here $Z_{\mathrm{s}} = 42$ is the molybdenum charge number, $Z_{\mathrm{i}} = 54$ is the xenon charge number, a_0 is the Bohr radius, and m_{i} is the ion mass. By contrast, very little data is available for iodine ions (either atomic or molecular) striking any surfaces, nor has there been any significant research to develop iodine sputter codes. The lack of sputter yield data for other specific ion-surface element combinations is also a challenge for the materials processing community, and which was partially addressed in [216] by using a machine learning (ML) model based on Gaussian process regression to estimate unknown sputter yields. Previous lifetime testing studies [217] of an iodine-fueled gridded ion thruster have used sputter yields predicted from this model, and which are compared with those for xenon in figure 34. As seen, the

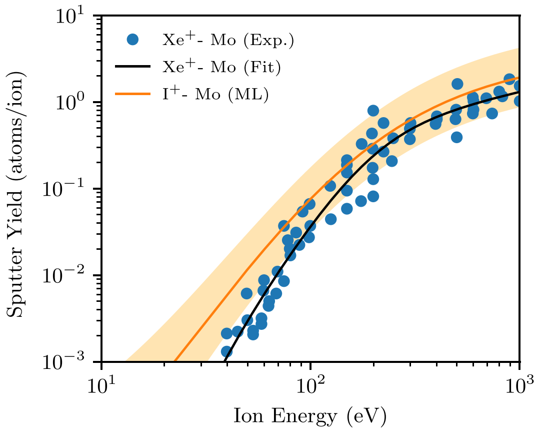

Figure 34. Sputter yields for singly-charged atomic xenon and iodine ions striking a molybdenum surface. Xenon data is taken from [214]. The black curve shows the empirical fit from equation (45), while the orange curve shows machine learning (ML) predictions from [216] (with the shaded orange region denoting model prediction uncertainty).

sputter yield for singly-charged atomic iodine ions is noticeably higher than that of xenon (although the majority of xenon data still falls within the shaded lower uncertainty region). However, comparing erosion rate predictions with measurements obtained through high-resolution metrology suggests that iodine sputter yields may be overestimated by roughly a factor of 2 [217]. By comparison, measurements correlated reasonably well when xenon sputter yield data was used instead. As almost no known experimental iodine sputter yield data is available for validation, the ML predictions in [216] should be viewed as an upper estimate with xenon sputter yield data a reasonable interim substitute until further data becomes available.

5. Applications and modeling of iodine plasmas

5.1. Space propulsion

5.1.1. Thrusters

The first proposal to use iodine within the context of space propulsion occurred at least as early as 1960 when Gilleo and Kash [218] introduced a propulsion concept using composite beams of positive and negative ions to achieve mutual neutralization. The idea was to generate negative ions via surface ionization processes from low work function materials, which was already widely being used at the time for positive ion formation (such as in cesium gridded ion thrusters) [7]. A strong motivation for this work was connected with neutralization of the positive ion beam generated by electrostatic propulsion systems, and concerns over whether electron emission for neutralization was viable. In particular, it was unclear if electrons would be able to provide space-charge compensation of the ion beam in the plume due to their small mass. Negative ions could potentially avoid this problem, and because of its high electronegativity, iodine was identified as a possible propellant. A similar concept was proposed in 1963 by Bussi and Filippi [219]. Around the same time, several other works emerged associated with negative ion formation. For example, in 1962 Dong *et al* [220] performed experiments to generate I^- with the aim of producing a negative ion beam source. Experiments were performed to create negative ions on lanthanum or gadolinium hexaboride surfaces via surface ionization processes. The maximum current density measured was 15 mA cm^{-2} and the technique was concluded to be technically viable with no iodine surface contamination observed. A schematic of the original experiment is shown in figure 35.

The use of iodine for producing negative ions for neutralization then appears to have ‘vanished’ from the literature, possibly because of the successful SERT-1 mission launched in 1964, which tested two mercury-fueled gridded ion thrusters. Neutralization was achieved using thermionic filament neutralizers, which conclusively demonstrated that electrons were able to achieve ion beam neutralization. As electron emission is simpler and easier than negative ion emission, neutralization using electrons subsequently became commonplace and is now used in virtually all electrostatic propulsion systems (with the notable exception of electrospray or colloid thrusters which use ionic liquid propellants [221], and micro-cathode arc thrusters which use a solid metal propellant [222]). Additionally, with the advent of hollow cathode neutralizers which are extremely energy efficient [3], the need for negative ion neutralization effectively disappeared.

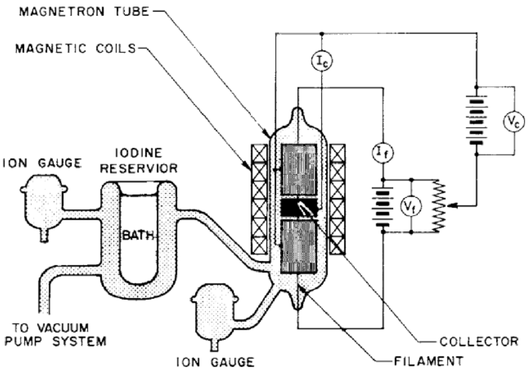

Figure 35. Schematic of the experimental apparatus used by Dong *et al* to produce I^-. Reprinted from [220], Copyright (1962), with permission from Elsevier.

Figure 36. Photograph showing the BHT-200 Hall thruster operating with iodine. The discharge voltage is 250 V and the discharge power is 500 W. From [225]. Reprinted by permission of the American Institute of Aeronautics and Astronautics, Inc.

Iodine did not receive significant consideration again for space propulsion until the early 2000's when Dressler *et al* [21] proposed iodine as an alternative propellant to xenon in the context of general positive ion formation. After the first gridded ion thruster tests which used mercury and cesium propellants, xenon later emerged as the preferred propellant of choice, in large part because of its low reactivity and toxicity. However, based on space industry trends and long-term projections, Dressler *et al* noted that cost and availability problems with xenon were likely to occur in the near future and that alternative propellants would be needed. Iodine was identified as an attractive propellant option because its atomic mass is similar to xenon, the ionization threshold energies of both I and I_2 are low, and iodine can be stored unpressurized as a solid with a high density. Dressler *et al* concluded that iodine was potentially a feasible alternative to xenon, but that further investigation was required.

Around the same time, Tverdokhlebov and Semenkin [22] considered several alternative condensable propellants for Hall thrusters, including iodine. It was again noted that the availability of xenon (due to a low global production output) was a restriction that could cause challenges for the space industry in the future. After considering several alternatives, iodine was discussed as an attractive option as world production is several orders of magnitude higher than xenon, and iodine can be stored as a solid with a low temperature required for sublimation. Several potential reactivity and toxicity concerns were however noted.

Several patents for iodine electric propulsion systems were subsequently filed, first by Dressler *et al* [223] in 2003 and then by Chabert [224] in 2006. However, the first known iodine electric propulsion system was only developed and tested in 2011 by Szabo *et al* [225] at the US company Busek. Ground experiments consisted of an iodine-fed Hall thruster, an iodine propellant storage and feed system, and a prototype power processing unit. Neutralization was provided with a xenon-fueled hollow cathode. Operation was found to be stable and performance was comparable with xenon. Figure 36 shows a photograph of the thruster operating with iodine, while figure 37 shows a performance comparison between iodine and xenon propellants. Solid iodine crystals were stored in a reservoir and then sublimated using a thermal control system to vary the pressure and achieve target mass flow rates. For mass flow rates of the order of 1 $\mathrm{mg\,s^{-1}}$, and a discharge voltage of 300 V, the thrust-to-power ratio observed was about 60 $\mathrm{mN\,kW^{-1}}$ with an anode specific impulse and anode thruster efficiency of approximately 1500 s and 45%–50% respectively. The ion beam plume was found to be well-collimated and contained small fractions of I_2^+, I^{2+}, and I^{3+} [226], with the dominant ion being I^+. This was confirmed in subsequent work by Chiu and Prince [227] who performed optical emission spectroscopy of the thruster plume.

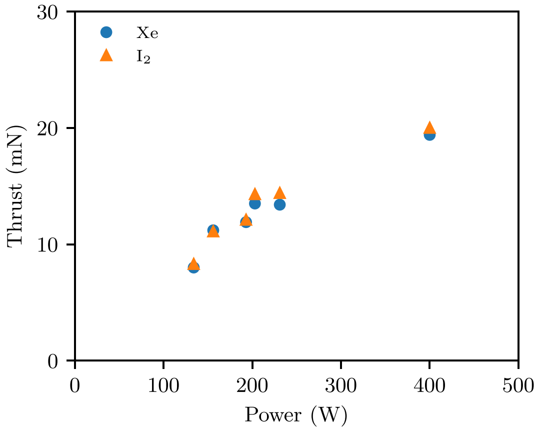

Figure 37. Thrust as a function of power for the BHT-200 Hall thruster operating with xenon and iodine. The propellant mass flow rate is between 0.58 and 1.04 mg s^{-1}. Data taken from [225].

Following successful ground-testing, Busek performed an extensive set of additional experiments with different Hall thruster variants, and power levels ranging from below 200 W to around 10 kW [228, 229]. As a general conclusion, iodine was found to be a viable alternative propellant that can provide superior performance to xenon for various space missions. Furthermore, a strong reduction in propulsion system size, mass, and cost is possible, and iodine deposition on spacecraft components was predicted to be negligible. Some of the above tests were supported by NASA, which began to invest in further advancing iodine propulsion technology [230, 231]. In particular, a CubeSat-sized iodine Hall thruster demonstrator mission was proposed in 2012 [232] based on the Busek BHT-200 Hall thruster and which led to the Iodine Satellite (iSAT) mission. Although iodine Hall thrusters were developed and delivered as part of the mission, it did not fly. Scheduled for launch in 2018, the mission was stopped in 2017 because of concerns related to propulsion system maturity: particularly operational challenges with the iodine hollow cathode [231] (see also sections 5.1.2 and 7.2).

Several other research groups also began seriously investigating iodine around this time. This included Tsay *et al* [233] (also at Busek) who developed a gridded ion thruster (the BIT-3) based on RF inductively coupled plasma (ICP) technology. This propulsion system also included an RF neutralizer (see section 5.1.2 below). Similarly, Holste *et al* [234] developed an iodine-fueled gridded ion thruster based on the existing RIT-10. Results were found to be broadly comparable with xenon, although iodine exhibited higher performance at low mass flow rates, while at higher mass flow rates (and hence pressures), there was a strong decrease in performance: consistent with the collisional energy loss arguments discussed in section 3.8. Holste *et al* concluded that iodine appears to be a feasible alternative propellant to xenon, although neutralization was achieved using a heated tungsten filament. Shortly after however, Dietz *et al* [109] developed and tested an iodine-fueled RF neutralizer to replace the thermionic filament (see section 5.1.2).

In parallel to the above studies, work on iodine electric propulsion also began in France at Ecole Polytechnique and which was largely motivated by the plasma propulsion using electronegative GASES (PEGASES) propulsion concept [235]. PEGASES was a proposed dual-beam propulsion system that alternatively extracts and accelerates positive and negative ions (somewhat similar to the original iodine propulsion concepts; see [218, 219]). A primary requirement of this concept was a propellant with a strong electron affinity to enable negative ion formation, and iodine was quickly identified as an ideal propellant. Several experimental prototypes were developed demonstrating the basic idea and validating the alternate ion beam extraction concept [236–238]. In 2016, the French company ThrustMe spun out of Ecole Polytechnique and began pioneering the use of iodine in the space industry. To partially validate several iodine technologies (such as the propellant storage and flow control systems) the I2T5 cold/warm gas propulsion system was developed [27], and which is illustrated in figure 38. Here, solid iodine is stored unpressurized and then sublimated using a temperature-controlled feedback loop. The iodine vapor is then expanded through a small nozzle to generate thrust. The high storage density of iodine, and the simple flow control hardware required, enabled a compact propulsion system design with a 0.5-Unit (0.5U) form factor and a total wet mass of 0.9 kg. Concurrently, ThrustMe also developed the NPT30-I2, which is an iodine-fueled RF gridded ion thruster [2], a cut-away view of which is shown in figure 39. The use of iodine enabled a high impulse density system with a wet mass

Figure 38. Photograph of the I2T5 cold/warm gas propulsion system. Reproduced with permission from [27].

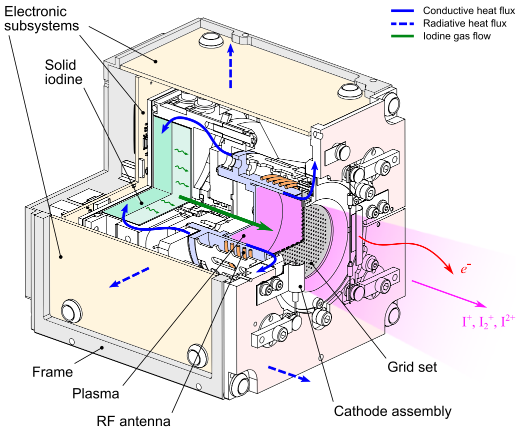

Figure 39. Cutaway schematic of the NPT30-I2 propulsion system. Reproduced from [2]. CC BY 4.0.

of 1.2 kg, and a form factor of only 1U: almost half that needed for a similar xenon version. To promote further propulsion system miniaturization, electron-emitting thermionic filaments were used for ion beam neutralization.

Following the successful in-space demonstration of the NPT30-I2 in 2020, several other organizations have developed iodine electric propulsion systems. This includes the IRIT4 gridded ion thruster by Yang *et al* [239], as well as the REGULUS ambipolar thruster developed by the Italian company T4i [240], and the electron cyclotron resonance ambipolar thruster ECRA developed by ONERA. In the REGULUS system, plasma is created using an RF antenna and is then expanded through a magnetic nozzle. This creates an internal electric field (called an ambipolar field) that then accelerates ions to generate thrust. A strong advantage of such ambipolar acceleration is that the thruster is inherently current balanced, and so no neutralizer is needed. More recently, ThrustMe has developed the prototype iodine Hall thruster JPT-150 [241], while Busek offers several Hall thruster variants that are compatible with iodine [228]. Iodine Hall thrusters have also been developed by Xu *et al* [242], Paganucci *et al* [243] in collaboration with the Italian company SITAEL, and more recently by Esteves *et al* [244] in collaboration with Safran Spacecraft Propulsion. A recent review by Tirila *et al* [245] has compiled Hall thruster performance data for a number of propellants. Iodine gives similar, or even superior, performance to xenon over a wide power range from 100 W to 10 kW, and is found to be one of the best alternative propellants available: nicely validating the original proposals by Dressler *et al* [21] and Tverdokhlebov and Semenkin [22]. Finally, a consortium led by Airbus is developing several iodine-fueled thrusters as part of the iFACT project (iodine Fed Advanced Cusp Field Thruster), which are based on a cusp magnetic

Table 18. Example commercial iodine, or iodine-compatible, electric propulsion systems and the number of systems in space (with respect to iodine). Here, power, thrust, and specific impulse ($I_{sp} = F/(\dot{m}g_0)$ where F is the thrust, $\dot{m}$ is the input propellant mass flow rate, and g_0 is the gravitational acceleration at sea level) represent nominal or maximum values depending on available data [27, 247–251].

Name	Organization	Power (W)	Thrust (mN)	I_{sp} (s)	Number in space
Cold/warm gas thrusters					
I2T5	ThrustMe	5	0.35	—	11
Gridded ion thrusters					
BIT-3	Busek	80	1.25	2300	At least 2
NPT30-I2-1U	ThrustMe	65	1.1	2400	96
NPT30-I2-1.5U	ThrustMe	65	1.1	2400	4
Hall thrusters					
BHT-100	Busek	100	7	1000	Unknown
BHT-200	Busek	200	13	1390	Unknown
BHT-350	Busek	300	17	1244	Unknown
BHT-600	Busek	600	39	1500	Unknown
BHT-1500	Busek	1500	101	1710	Unknown
BHT-6000	Busek	6000	325	2700	Unknown
BHT-20K	Busek	20 000	1005	2515	Unknown
JPT-150	ThrustMe	300	10	1600	-(R&D stage)
PPS®X00	Safran	1000	—	—	-(R&D stage)
Ambipolar thrusters					
REGULUS-50-I2	T4i	50	0.55	550	At least 1
ECRA-30	ONERA	30	—	—	-(R&D stage)
ECRA-150	ONERA	150	—	—	-(R&D stage)
Cusp field thrusters					
Alberich	Airbus	20	0.63	900	-(R&D stage)
MkI	Airbus	300	—	—	-(R&D stage)
Linear CFT	Airbus	1000	—	—	-(R&D stage)

field thruster somewhat similar to Hall thrusters [246]. A summary of several commercial iodine-fueled electric propulsion systems is listed in table 18.

To conclude, Building blOcks for iOdine thruSTers [252], a research initiative funded by the European Union, was recently launched with the primary goal of advancing and promoting iodine electric propulsion technology as a key enabler for the small satellite market; overcoming the current low technological maturity through a modular approach focused on developing essential building blocks for future commercialization.

5.1.2. Neutralizers

The majority of iodine electric propulsion systems developed to date are classed as electrostatic systems (such as gridded ion or Hall thrusters), which require an electron-emitting neutralizer [3]. Not only is this needed to ensure overall current balance of the propulsion system and spacecraft, but it is also necessary for charge compensation to prevent ion-beam stalling [7]. In the case of Hall thrusters, the neutralizer also serves as an electron source for initiating and sustaining the plasma discharge.

Currently, there are three main types of neutralizer technology which includes: a heated wire filament, a miniature RF or microwave plasma discharge, and a thermionic hollow cathode. A filament neutralizer is the simplest and consists of a metal wire (such as thoriated tungsten or tantalum) that is heated by flowing a sufficiently high current through it. Ohmic heating of the wire causes a temperature increase that can lead to thermionic electron emission. Although filament neutralizers have flown in space [2, 253], they are not widely used because the wire can evaporate at typical operating temperatures and/or is very susceptible to damage (such as from sputter erosion due to ion bombardment)

Table 19. Common neutralizer technologies and their typical efficiencies (representative data taken from [257]).

Neutralizer	$\mathcal{E}_e$ (eV)	η_g
Filament	1000–2000	—
RF/microwave	100–300	1–10
Hollow cathode	15–50	1–100

[217]. There is also a limit to the maximum electron current density that can be extracted because of both Richardson's law [3], and the Child–Langmuir law associated with space-charge effects [124]. By contrast, RF neutralizers make use of an ICP discharge and then extract a quasi-neutral plasma (but with a net electron current) through an orifice [109, 233, 252, 254]. Microwave neutralizers operate in a similar manner [255, 256]. As the discharge is essentially quasi-neutral and electrodeless, a higher electron current density can be extracted and erosion is reduced or eliminated. Finally, hollow cathodes create a high-density plasma discharge inside a hollow cylindrical geometry via electron emission from a special heated insert material (such as lanthanum hexaboride, LaB_6, or barium oxide, BaO [3, 257]; see also section 7.2) and a quasi-neutral plasma is again extracted through an orifice. Care is needed when operating and handling hollow cathodes however, as the insert material is susceptible to poisoning or chemical reactions with some substances [3]. Despite this, hollow cathodes are by far the most efficient and dominant neutralizer technology to date.

Neutralizer power efficiency can be expressed in terms of an electron energy cost given by

$$\mathcal{E}_e = \frac{P_{\text{neut}}}{I_e}, \tag{50}$$

where I_e is the net extracted electron current and P_{neut} is the total power needed to operate the neutralizer. A typical design objective is to minimize the energy cost. While RF, microwave, and hollow cathode neutralizers can achieve a lower energy cost than filament neutralizers, they require a small amount of propellant flow (approximately 5%–10% of the main thruster mass flow rate) to operate [3]. Consequently, a propellant gas utilization efficiency can also be defined by

$$\eta_g = \frac{MI_e}{e\dot{m}}, \tag{51}$$

with M the atomic/molecular mass of the propellant, $\dot{m}$ the neutralizer propellant mass flow rate, and e the elementary charge. Table 19 provides representative efficiency values for the different neutralizer technologies, where it is seen that hollow cathodes have the lowest electron energy cost.

At present, the only known technology demonstrated in space for iodine-fueled electric propulsion systems is a filament neutralizer, which is used by the NPT30-I2 thruster [2]. While such neutralizers are simple and do not require any propellant flow, their electron energy cost is very high. Thus, they are only appropriate for low currents (for reference, the ion beam current produced by the NPT30-I2 is between about 10 and 20 mA [2, 28]). For higher currents, and in particular for Hall thrusters, the electron energy cost of filament neutralizers is too high to be feasible. For example, consider a 1 kW Hall thruster generating a nominal ion beam current of 4 A. If a filament neutralizer is to be used, and assuming an aggressive design with an electron energy cost of 1000 eV, the power consumption required is 4 kW. Another challenge with filament neutralizers is that they are easily damaged. Recent testing suggests that the maximum lifetime may be limited to just above 1260 h [217]: a value that may be insufficient for many space missions.

RF/microwave neutralizers have an electron energy cost almost an order of magnitude lower than filaments, and are less prone to erosion or degradation. They are therefore well-suited for long-duration missions and flight models operating with iodine have already been successfully developed [257]. Indeed, an RF neutralizer (the BRFC-1; see figure 40) is used by the BIT-3 thruster [233], although publically available information on flight heritage is not known. The status of iodine neutralizers have recently been thoroughly discussed in the review paper by Becke *et al* [257], who have identified various organizations developing iodine neutralizers. Becke *et al* note that while there does not appear to be any technical barrier for RF neutralizers, as of 2025 there has been no known stable, long-term operation of a hollow cathode using iodine (see also section 7.2). The electron energy cost for RF neutralizers may however still be too high for some thrusters. Using the Hall thruster example from before, and assuming an electron energy cost of 100 eV, the power consumption is about 400 W: a significant fraction of the total propulsion system power. By contrast, the power consumption of a hollow cathode for this example could be as low as 60 W.

Figure 40. Photograph of the BIT-3 ion thruster (bottom discharge) and BRFC-1 RF neutralizer (top discharge) operating with iodine. From [233]. Reprinted by permission of the American Institute of Aeronautics and Astronautics, Inc.

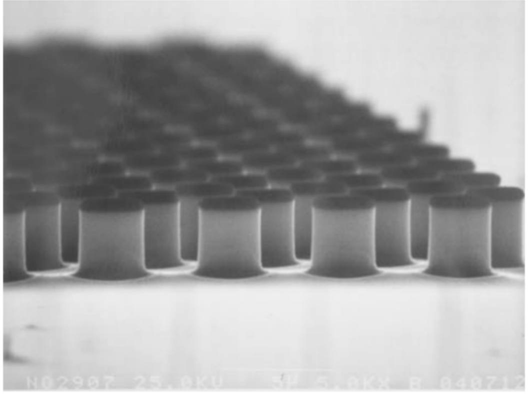

Figure 41. Scanning electron microscope image of InP cylindrical array patterns produced using iodine plasma etching. Reproduced from [23]. © IOP Publishing Ltd. All rights reserved.

5.2. Industrial applications

Although interest in iodine plasmas has largely been driven by space propulsion needs in recent years, there are also a number of potential ground-based applications including dry etching [23, 258], material surface treatment or modification [259, 260], lasers [261–263], and UV light sources [264]. Unlike for propulsion, a mixture of different gases (such as xenon and iodine), or even iodine compounds (such as boron triiodide; BI_3), are typically used instead of pure iodine. While this adds further reaction processes beyond those explicitly treated in this review article, various atomic and molecular neutral and ionic iodine species are nonetheless expected to form such that much of the volume and surface plasma chemistry is still relevant.

Low-temperature dry etching of III–V semiconductors is often desired for preserving fine resist masks during fabrication. An important requirement for dry etching is that the product of the reaction between radicals in the plasma and atoms of the material surface must be volatile. The use of iodine plasmas has been proposed for the etching of certain semiconductor materials [23] such as indium phosphide (InP), gallium arsenide (GaAs), and silicon dioxide (SiO_2). As the volatilization temperature of indium iodide (InI) is much lower than indium chloride (InCl), a lower temperature etching process can be realized. For example, [23, 265] describe an etching process for micro/nano-optical or electron device fabrication, as well as photonic crystals. Solid iodine crystals are placed on a heated substrate that causes sublimation and the resulting iodine vapor is then distributed within the processing chamber. Controlling the substrate temperature allows the iodine vapor pressure (and hence mass flow rate) to be adjusted. An ICP discharge is created above the substrate using xenon as the main feed gas, although reactive iodine ions are also generated from the iodine vapor. By applying an RF bias to the substrate, the ion energy can be controlled and a smooth vertical etch of the substrate material obtained. For the etching of InP, a low process temperature of only 90 °C is required and a reasonable etch rate of $0.4\,\mu\text{m}\,\text{min}^{-1}$ can be achieved. By comparison, etching with chlorine requires process temperatures as high as 250 °C. Figure 41 shows a scanning electron microscope image of optical waveguides fabricated using this technique.

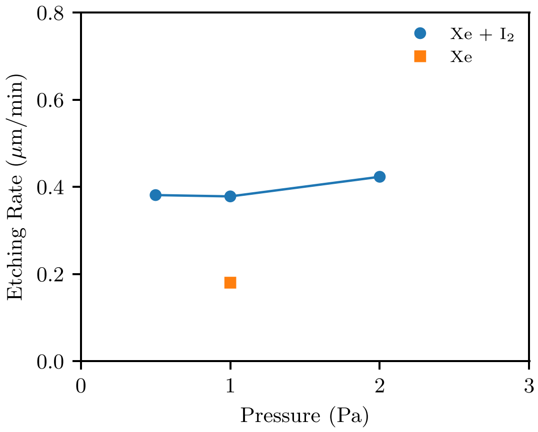

Figure 42. Etching rate of InP as a function of pressure. The ICP power is 300 W, the substrate bias power is 20 W, and the process temperature is 90 °C. Data taken from [23].

Other sources of iodine have included HI for use in neutral beam etching of gallium nitride (GaN) and indium gallium nitride (InGaN) for micro light-emitting diodes [266]. Compared with chlorine neutral beam etching, a higher etch rate is observed when using HI, together with a lower surface roughness and significantly lower etching residues. These results are consistent with those obtained earlier by Pearton *et al* [267], who also showed that HI is a universal etchant for III–V semiconductors enabling very anisotropic etch features. It should be noted though that in some cases, non-hydrogen etchants are preferred as they can result in simpler etch processes and equipment requirements [268]. Solid iodine is therefore an attractive etchant, which also allows more precision in the etching process to be achieved by finely controlling the amount of iodine placed in the processing chamber. Although argon is often used as a feed gas in semiconductor manufacturing, xenon was chosen for iodine etchants because it has a similar mass to atomic iodine [23, 265]. With the use of iodine in the process, the etch rate increases by a factor of almost two compared with that observed for xenon alone. This is thought to result from the higher chemical reactivity of iodine and the higher volatility of the etch products. Figure 42 shows the measured etching rate with pure xenon and xenon/iodine chemistries. Iodine can also have other advantages. For example, when etching indium gallium arsenide phosphide (GaInAsP) structures [268], although indium iodide (InI_3) has a high volatility, other iodide etching products can form a passivization layer protecting etch structure sidewalls. As an alternative to solid iodine crystals, iodine trichloride (ICl_3) powder has been used to etch GaAs [265]. The main etching mechanism depends on the process pressure with sputtering by positive ions dominating at pressures around 0.1 Pa, while chemical etching dominates at 1 Pa.

The etching process described above has also been investigated for the dry etching of silicon (Si) [269], and is very simple as it is free of any carbon, carbon fluoride, or hydrogen reaction products. This is potentially attractive as such products can lead to the deposition of a polymeric layer on etched surfaces. While xenon fluoride (XeF_2) as been used as an alternative etchant, the etching profile is very rough and isotropic which affects device performance. Similarly, although HI has been demonstrated as an etchant, the presence of hydrogen can induce damage to the substrate. Thus, solid iodine etching again offers potential advantages as it avoids these issues. Since deep vertical etches with smooth profiles can be produced (typically with a surface roughness of 6 nm: i.e. smaller than the wavelength of light which satisfies optical device requirements) and with reasonable etching rates of up to 90 nm min^{-1}, solid iodine could be useful for fabricating micro-electromechanical system devices. For the etching of silicon, the use of iodine has been found to increase the etch rate by a factor of 3–4 over pure xenon depending on the process pressure and substrate bias power [269]. Since pure xenon etching is due to sputter erosion, it is thought that iodine etching is again of a chemical nature. This demonstrates that although iodine reactivity may be a disadvantage for some applications (see section 4.1), it can in fact be beneficial for other applications.

The use of iodine for etching is not however always useful. For example, [270] studied the etching of zinc oxide (ZnO) and indium-zinc-oxide (IZO) films with iodine bromide (IBr) and BI_3 chemistries where little benefit was observed. The etching rates found were similar to those for physical sputtering from pure argon. Similarly, BI_3 was used to etch lanthanum manganite perovskite ($LaCaMnO_3$) for magnetic memories and sensors in [271]. While some chemical etching enhancement was observed (amounting to a few tens of percent), above a certain gas flow rate the etch rate in fact decreased due to the adsorption of iodine on the substrate surface. Iodine was also found to be impractical for the etching of silicon carbide (SiC) in [272] because the resulting etch products are not sufficiently volatile.

Several studies have investigated the use of iodofluorocarbon substances (such as iodotrifluoroethylene and 1-iodoheptafluoropropane) for etching dielectric films as an alternative to perfluoro compounds currently used and which have a strong global warming potential [273]. Promising results have been found for the etching of SiO_2 and silicon nitride (SiN_2) films. Global warming concerns with perfluorinated compounds have also led to research with trifluoroiodomethane (CF_3I) for atomic layer etching [274, 275], which is a type of etching that has received increased interest in recent years as it allows atomic-level control of etch thickness and exhibits self-limiting characteristics [276, 277].

Focused ion-beam etching has been proposed as a technique enabling rapid prototyping of new micro-/nano devices and has been applied to the etching of silicon for photonic applications [278, 279]. Optical losses due to crystal damage and ion implantation can make the manufacture of some optical devices impractical or challenging. However, such damage can be reduced by etching with iodine gas enhancement, followed by thermal post-treatment to desorb any silicon-iodine bonds from the surface. Using a 30 keV gallium focused ion beam, [278, 279] injected iodine vapor from a gas nozzle positioned near the etch site. The nozzle contained a crucible with solid iodine heated to 42 °C causing sublimation and adsorption on the silicon surface. Measurements indicated that optical losses were reduced from $3520\,\mathrm{dB\,cm^{-1}}$ for a direct gallium ion beam etch, to approximately $196\,\mathrm{dB\,cm^{-1}}$ when iodine was added (followed by thermal post-treatment).

Aside from etching, there are also other uses for iodine, such as in surface modification/treatment. For example, in [259] carbon nanospheres were impregnated with iodine and iron–nitrogen (Fe–Nx) dopants using a solution plasma process to improve electrocatalytic activity. Iodine dopants have a large atomic radius that can induce defects and distortions in the carbon lattice and positively affect oxygen reduction reactions for fuel cells. In this sense, such novel dopants can act as alternative catalysts to platinum. Iodine can also promote improved electron conductivity and enable high current densities to be achieved. In [280], a low-temperature CCP iodine plasma was used to treat activated carbon for use as an electrode in electrochemical capacitors. Iodine-doped carbon leads to samples that are much rougher compared with untreated carbon (see figure 43), and electrochemical measurements indicate superior performance. This is potentially useful for supercapacitors because of the reversible reduction-oxidation (redox) reactions of iodide species at the carbon/electrolyte interface. Other applications include the manufacture of catalysts for water splitting and hydrogen generation applications [281]. Inspired by observations that iodine addition to some lamps can increase filament lifetime (by binding to evaporated tungsten atoms and promoting re-deposition onto the surface of the filament), [281] used an atmospheric pressure iodine dielectric barrier discharge to create three-dimensional copper sulfide (Cu_2S) nanosheet arrays for the low-cost fabrication of novel oxygen evolution reaction catalysts. Finally, iodine-based substances, such as iodophor and povidone–iodine, have been used to create antiseptic nano-scale coatings via plasma polymerization for medical devices and wound dressings [260]. Such coatings have been shown to exhibit broad spectrum anti-bacterial activity against microbes responsible for wound infections: including drug resistant strains.

Iodine plasmas can also indirectly be formed in several other applications. For example, determination of iodine content in food or geological samples is often conducted using ICP mass or optical spectrometry [282–284]. Knowledge of the relevant iodine plasma chemistry, surface reactions, and different species formed can therefore aid the understanding and interpretation of measurements obtained. Similarly, the purification of iodine for semiconductor production has been studied in [285] to reduce carbon or metal impurities. Here, an oxygen-argon ICP plasma interacts with iodine vapors to form diiodine oxides (I_2O_5). Thermal decomposition then produces oxygen and high-purity iodine: a process that could also be relevant to the production of high-purity iodine propellant for space propulsion applications.

5.3. Theoretical and numerical modeling

Sections 2–4 provided a comprehensive set of data associated with general iodine properties, collision reactions and plasma chemistry, and plasma-surface interactions. Aside from being useful in understanding the basic underlying processes relevant to iodine plasmas, this information is important for the design of practical devices (such as propulsion or processing systems as discussed in sections 5.1

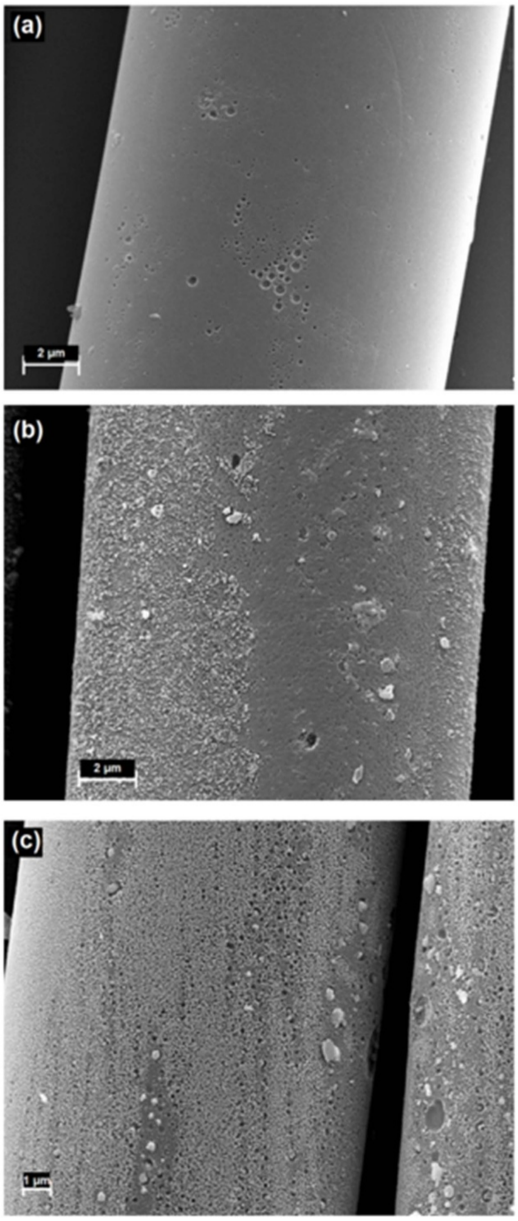

Figure 43. Scanning electron microscope images of (a) unmodified carbon, (b) iodine treated carbon (20 W for 10 min), and (c) iodine treated carbon (80 W for 10 min). Reprinted from [280], Copyright (2016), with permission from Elsevier.

and 5.2), is needed to help interpret or analyze several diagnostics (such as optical emission spectroscopy), or is a critical input to theoretical/numerical models. This last point is particularly relevant as iodine plasmas are significantly more complex than noble gas plasmas like argon or xenon.

The majority of modeling efforts to date have focused on electric propulsion applications. The first known model of an iodine plasma was developed by Grondein *et al* in 2016 [71] using electron impact cross-section data largely obtained from Hamilton [29]. In this work, Grondein *et al* developed a model of an RF gridded ion thruster and studied system performance when using xenon or iodine. Overall, comparable performance was obtained and iodine was found to be a viable alternative propellant. However, at low mass flow rates, the performance with iodine was predicted to be higher than with xenon: consistent with experimental measurements performed several years later by Holste *et al* [234] and Esteves *et al* [286]. The work by Grondein *et al* helped to create an initial iodine reference reaction set that was subsequently leveraged in several previous works: first by Lucken [97] and Marmuse [98], and more recently by Lafleur *et al* [28] and Esteves [26, 287]. The model of Grondein *et al* also appears to have been adapted by Dietz *et al* [109] to model iodine RF neutralizers. While the general trends were consistent with experiment, the predicted neutralizer current was approximately two times higher than that measured experimentally.

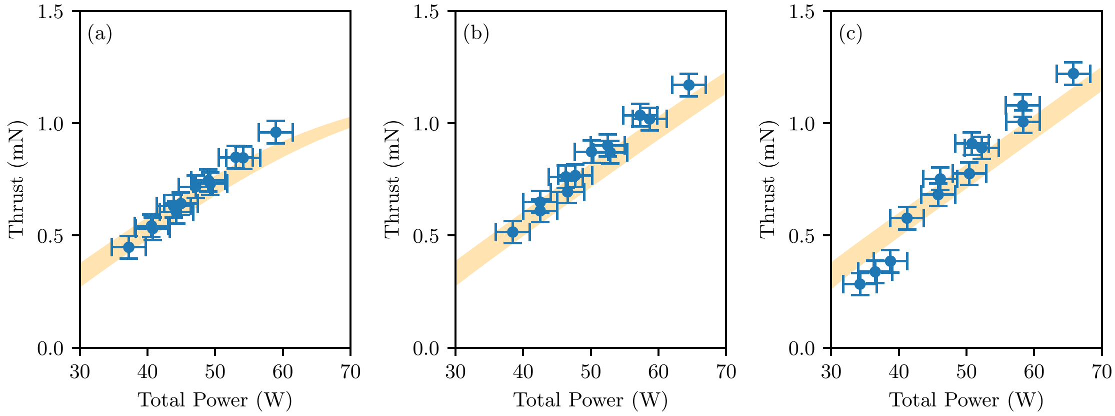

Figure 44. Thrust of the NPT30-I2 as a function of total propulsion system power for mass flow rates of (a) 38 μg s^{-1}, (b) 58 μg s^{-1}, and (c) 99 μg s^{-1}. Data markers show experimental measurements while shaded regions indicate model predictions. Data taken from [288].

Lafleur *et al* [28] and Esteves [26, 287] developed more sophisticated models than Grondein *et al* by including additional reaction processes and using updated electron scattering cross-sections provided by Ambalampitiya *et al* [31]. The model of Esteves was compared with experimental measurements performed in an RF ICP plasma source showing good agreement. Similarly, the model of Lafleur *et al* was validated with measurements of the ion beam current and propellant utilization efficiency ($\eta_m = \dot{m}_\mathrm{i}/\dot{m}_\mathrm{in}$ where $\dot{m}_\mathrm{i}$ is the ion mass flow rate and $\dot{m}_\mathrm{in}$ is the propellant inlet mass flow rate) obtained with the NPT30-I2 propulsion system (see section 5.1). Further work by Jia-Richards and Lafleur [288] then compared the predicted and measured thrust where excellent agreement was obtained, as demonstrated in figure 44 (see also section 6.1). Overall, the above works indicate that although there are missing collisional processes and cross-section data, current reaction sets appear reasonable and can be used to predict realistic system performance. Results also confirm that performance with iodine is higher than xenon at low mass flow rates, and that it appears to be a promising alternative propellant. Furthermore, the higher elastic scattering cross-section of atomic iodine, and the shallower Ramsauer minimum (see section 3.2.1), may enhance electron momentum transfer leading to a higher RF power coupling efficiency in low-pressure ICPs [28]. However, both Lafleur *et al* and Esteves noted that there is still uncertainty in the validity of available elastic scattering cross-sections for atomic iodine at low electron energies and that further research is needed.

The works above use volume-averaged models focused on iodine reaction kinetics and global system performance. Several studies have however investigated discharge spatial variations. This includes the 2D model by Levko and Raja [108] who simulated an iodine ICP, Esteves [26] who developed a 1D model of iodine gas flow in an ICP (including a limited set of plasma collisional processes), and Liu *et al* [289] who developed a 2D fluid model of an iodine-fed hollow cathode discharge. This last model underwent partial validation against experimental electrical measurements, revealing the critical importance of molecular iodine dissociation due to electron impact and thermal processes, which results in atomic iodine as the dominant neutral species. While the simulated discharge behavior shared some similarities with xenon, significant differences were also observed. Simulations illustrate that including I^- results in a higher ionization degree, discharge power, and electron and gas temperatures compared to cases where I^- was not considered. These findings underscore the necessity of thoroughly understanding the more complex iodine plasma chemistry to help optimize the design and operation of iodine neutralizers. As an illustration, figure 45 presents example 2D contour maps of key plasma properties within the hollow cathode, as simulated by Liu *et al.*

Other multi-dimensional models include the work of Saifutdinova *et al* [290] who simulated an iodine ICP with a more sophisticated plasma chemistry than that originally used by Levko and Raja [108]. An interesting finding of this work is that for short initial simulation times, the discharge is an ion–ion plasma dominated by I_2^+ and I^- charged species, and that it only transitions to an electron–ion plasma (dominated by I^+ and e^-) after several milliseconds. This was also studied by the same authors

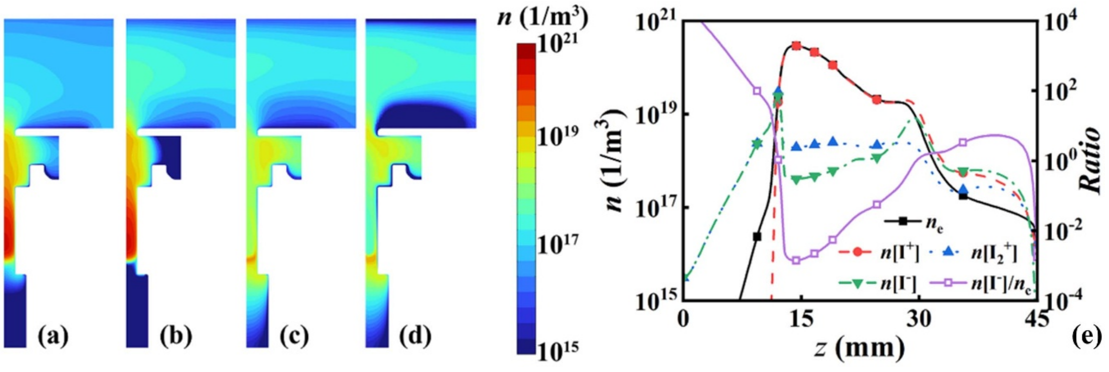

Figure 45. Spatial density distribution of (a) electrons, (b) I^+, (c) I_2^+, and (d) I^- in an iodine hollow cathode, with a 1D profile along the hollow cathode axis shown in (e). Reproduced from [289]. © IOP Publishing Ltd. All rights reserved.

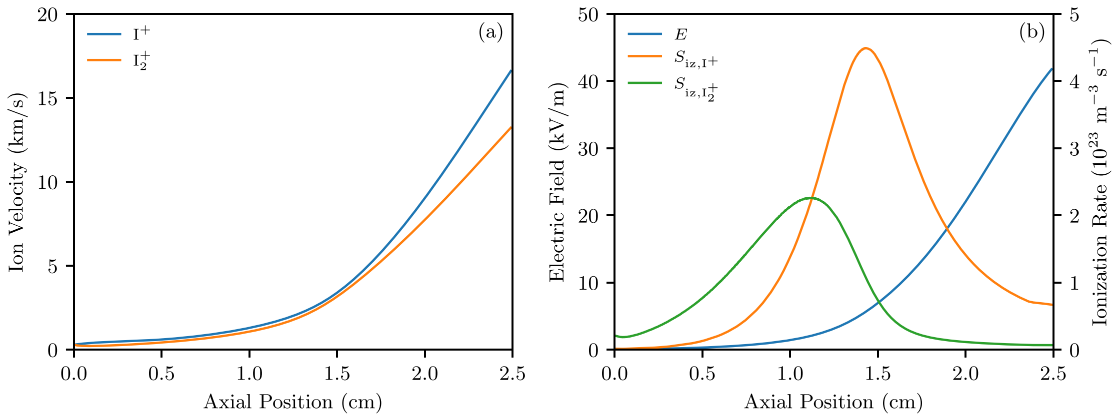

Figure 46. (a) Velocity of I^+ and I_2^+ species and (b) electric field (E) and ionization rate ($S_{\mathrm{iz,I^+}}$ for I^+ and $S_{\mathrm{iz,I_2^+}}$ for I_2^+) profiles as a function of axial position along the channel of an iodine-fueled Hall thruster. Reprinted from [294], with the permission of AIP Publishing.

using an earlier volume-averaged model [291], where it was found that an ion–ion plasma could be produced at low powers and for pressures above 3 Pa. As the power is increased, electron impact dissociation of molecular iodine starts to become more significant and a transition to a conventional electron–ion plasma is observed. Lequette [292] developed a quasi-2D iodine PIC model (which was 1D in the axial direction with approximate transverse boundaries) to simulate inductive discharges. This PIC model was coupled to a fluid model describing the evolution of neutral species and represents one of the only known iodine PIC codes developed to date. Lequette noted that at low pressures, the discharge is eletropositive and similar to a typical noble gas discharge. However, at higher pressures, the plasma becomes electronegative with a significant negative ion density. Strong gas heating is also observed, which is consistent with previous experimental measurements [26], and the atomic iodine temperature is higher than the molecular temperature. Gas heating appears to result from electron impact dissociation processes, although recombination reactions were also found to be relevant in some cases. The work of Lequette provides an important step towards high-fidelity 2D modeling of various iodine electric propulsion systems.

While many models have focused on gridded plasma sources, work has also been done to model Hall thrusters, ambipolar thrusters, and cusp magnetic field thrusters based on the high efficiency multistage plasma thruster (HEMPT) concept. Bianchi *et al* [293] developed a volume-averaged model of an iodine Hall thruster segmented into two separate zones (a dissociation zone and a combined acceleration and ionization zone). Results suggest that the density of negative ions is expected to be negligible, while an appreciable fraction of I_2^+ (as high as 30%) is predicted. Model results were found to be in reasonable agreement with the JPT-150 thruster prototype. Chabert *et al* [294] developed a 1D simulation of an iodine-fed Hall thruster and showed that there are two distinct ionization zones (see figure 46): one near the anode and associated with the ionization of molecular iodine, and a second downstream associated with the ionization of atomic iodine. A significant fraction of I_2^+ was predicted, and the use

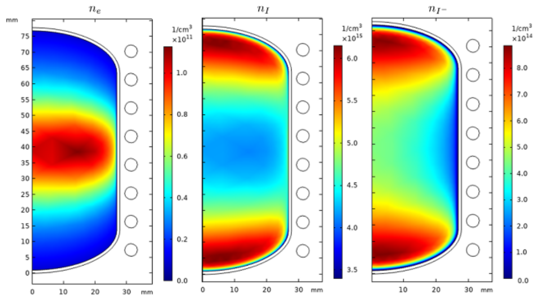

Figure 47. Spatial density distribution of electrons, I, and I^- species in an I_2-Xe ICP plasma operated at 400 W. Reproduced from [298]. CC BY 4.0.

of iodine allows an extension of thruster operating parameters to lower mass flow rates and discharge powers. Xu *et al* [242] performed 2D simulations of an iodine-fueled Hall thruster and found that the dissociation zone overlaps with the near-anode region and the ionization zone. Andrews *et al* [295] have developed a model of the REGULUS ambipolar thruster. In contrast to gridded ion thrusters, Andrews *et al* found that iodine gives slightly lower performance than xenon, but predictions where again in reasonable agreement with experimental measurements. Iodine ambipolar thrusters have also separately been modeled by Saini and Ganesh [296]. Niu *et al* [297] performed 1D fluid simulations of an iodine HEMPT thruster. Low-frequency oscillations (around 25 kHz) were observed and the densities of I^+ and I_2^+ were found to be similar. Iodine was predicted to give enhanced performance compared with xenon. As with the iodine Hall thruster models above, the density of I^- is again predicted to be negligible, which is not surprising given the high electron temperatures present in these devices, and hence the importance of molecular dissociation and detachment processes.

Finally, the work of Gehring *et al* [298] is noteworthy as it is one of the only models not developed for propulsion applications. Here, the commercial package COMSOL was used to simulate iodine ICPs for the development of mercury-free UV radiation sources, and results were compared with experimental data. In particular, the model included a mixture of xenon and iodine. Figure 47 shows the predicted spatial density distribution of different particle species.

6. In-space testing

6.1. Flight heritage

Although development of the first iodine-fueled electric propulsion system occurred at least as early as 2011 by the US company Busek [153], the first known in-space demonstration was in November 2019 by the French company ThrustMe who tested the I2T5 cold/warm gas thruster [27]. The system flew aboard the 6U CubeSat, Xiaoxiang 1-08, operated by the Chinese company Spacety [299], and which was placed into a 500 km circular Sun-synchronous orbit (SSO). The first firings of the thruster were between 16 and 19 November and consisted of 4 h of cumulative burn time. While propulsion system telemetry indicated successful operation, the firing duration and thrust was too low for a clearly discernible orbit change from global positioning system (GPS) and space surveillance network (SSN) data. Despite slight variations in expected thermal behavior compared with ground-testing, the system functioned as expected and validated iodine storage and flow control/distribution hardware [27].

The first in-space demonstration of a plasma-based iodine electric propulsion system occurred in 2020. This system (the NPT30-I2; also developed by ThrustMe) flew aboard the 12U CubeSat, Beihangkongshi-1 (again operated by Spacety), launched on the 6 November 2020 into a 480 km SSO [300]. Figure 48 shows a photograph of the propulsion system integrated with the satellite at the assembly facility. After several initial system tests, the first firing campaign took place at the end of December 2020 and continued until the end of February 2021. During the campaign, a total of 11 separate firings were conducted, with the satellite attitude control system adjusting the thrust vector direction to be parallel, anti-parallel, or perpendicular to the satellite velocity vector. The time evolution of the satellite mean semi-major axis is shown in figure 49, together with the firing tests performed. The black line in figure 49 shows the planned/expected semi-major axis from a simplified analytical model including the planned firing maneuvers and their duration. The decay between maneuvers occurs because of residual atmospheric drag on the satellite. The blue circles show independent tracking data from the SSN

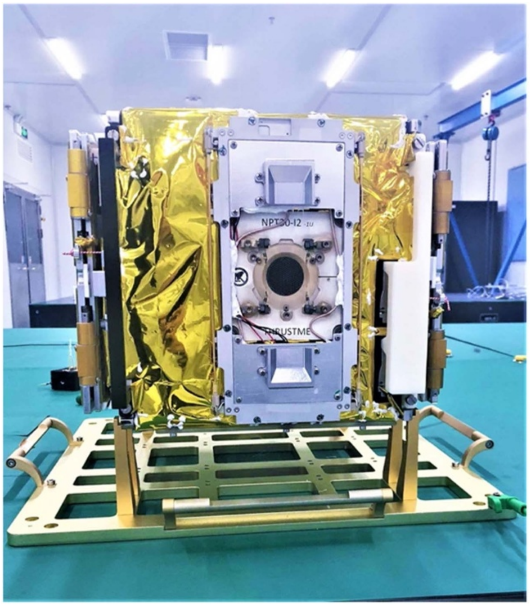

Figure 48. The NPT30-I2 propulsion system integrated with the Beihangkongshi-1 satellite before launch. Reproduced from [2]. CC BY 4.0.

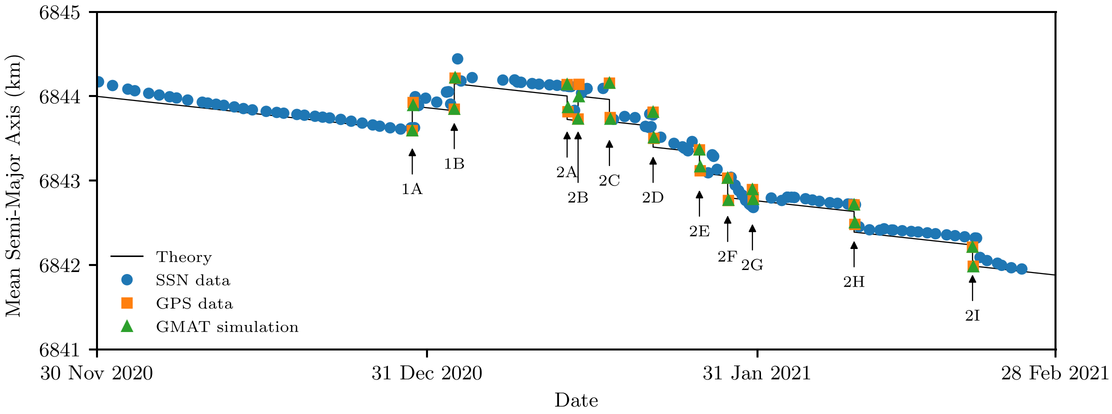

Figure 49. Mean semi-major axis of the Beihangkongshi-1 satellite with time. The black line shows predictions from theory, while the markers show data from the space surveillance network [301] (SSN; blue circles), onboard global positioning system receiver (GPS; orange squares), and high-fidelity numerical simulations using the general mission analysis tool [302] (GMAT; green up triangles). The arrows denote firing events. Reproduced from [2]. CC BY 4.0.

managed by the US Space Force, while the orange squares show GPS data taken just before and after each firing. Finally, the green up triangles show high-fidelity orbital dynamics simulations accounting for the propulsion system performance and firing duration. The nominal thrust was 0.8 mN for a total operating power of approximately 55 W, and the burn duration was between 80 and 90 min for each firing (which included the 10–20 min time needed for initial propellant heating). This resulted in a satellite altitude change between about 200 and 400 m.

Overall, the agreement between theory, simulation, and GPS/SSN measurements in figure 49 is excellent and there is a clear altitude change correlated with each firing. The thrust vector direction was varied such that the altitude increased for firings labeled 1A, 1B, and 2B (simulating a drag compensation maneuver for example), and decreased for firings 2A, 2C, 2D, 2E, 2F, 2H, and 2I (simulating collision avoidance or initial de-orbiting). For firing 2G, the thrust vector direction was such that the altitude was not expected to change. In total, a cumulative altitude change of 3 km occurred over all firings. In addition to a clear orbit change, onboard telemetry confirmed successful thruster operation. Figure 50 shows various grid current measurements, subsystem temperatures, and the thrust/power evolution for firing 1B. As seen, telemetry is consistent with ground testing data, which indicates that the space environment can be well replicated during thruster qualification.

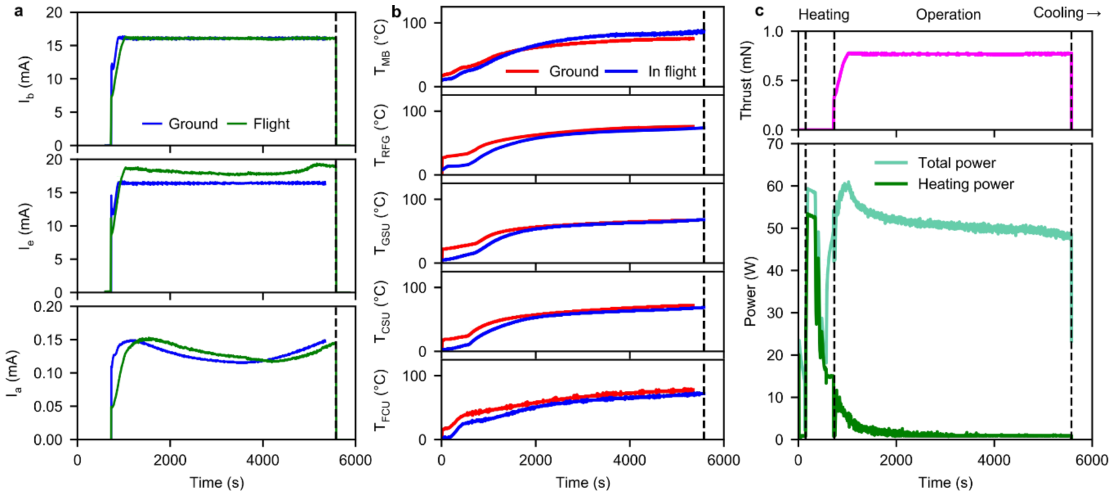

Figure 50. (a) Ion beam current (I_b), electron neutralizer current (I_e), and accel grid current (I_a), (b) propulsion subsystem temperatures, and (c) thrust and power evolution for firing 1B in figure 49. The symbols in (b) indicate the temperature of the MotherBoard (T_{MB}), the radio-frequency Generator (T_{RFG}), the accelerator grid supply unit (T_{GSU}), the neutralizer cathode supply unit (T_{CSU}), and the iodine flow control unit (T_{FCU}). Reproduced from [2]. CC BY 4.0.

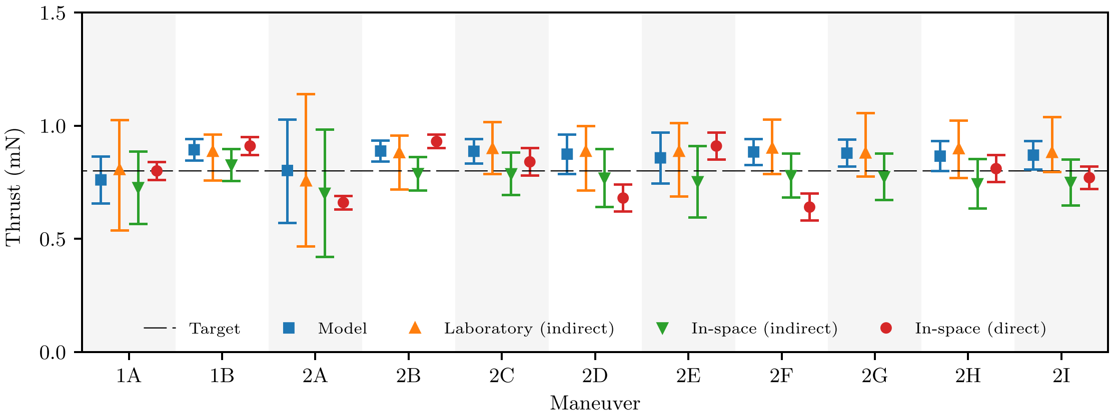

Figure 51. Average estimated thrust for each maneuver in figure 49 as determined by numerical modeling, and indirect/direct testing. From [288]. Reprinted by permission of the American Institute of Aeronautics and Astronautics, Inc.

An important factor in validating new propulsion technologies is a rigorous performance audit conducted throughout the design and testing phases, as even slight variations in performance can lead to unacceptable differences in predicted and actual spacecraft positions during flight [303]. While this has been performed and publically documented for some thrusters and missions, such as SERT-I and SERT-II [253, 304], performance audits of micropropulsion systems are far more limited [305, 306]. Based on numerical modeling (similar to that discussed in section 5.3 and which uses data from sections 3 and 4), indirect laboratory testing from diagnostic probes, indirect in-space testing from propulsion system telemetry, and direct in-space testing analyzing GPS data, a full thrust audit has been conducted of the NPT30-I2 [288]. Figure 51 shows a comparison of these different methods for the firings in figure 49, where excellent agreement and consistency is observed. Furthermore, the predicted thrust of all maneuvers is close to the nominal thrust level commanded by the satellite (black dashed line in figure 51). Such a thrust audit is an important step towards improving confidence in iodine propulsion technologies. The good agreement of the numerical model results with the various measurements also provides a strong indirect validation of the iodine plasma chemistry and cross-section data presented in section 3.

Since the in-space demonstration of the NPT30-I2 between 2020 and 2021, further flights of this technology have occurred with as many as 100 systems in space since July 2025 [307]. In addition, the BIT-3 gridded ion thruster developed by the US company Busek, and the iodine ambipolar thruster REGULUS developed by the Italian company T4i, have also subsequently flown [240, 308]. REGULUS was integrated with the Unisat-7 satellite and launched in March 2021, while the BIT-3 was included onboard the LunaH-Map cubesat and launched as part of Artemis 1 in November 2022. Publically available information is limited such that the status of these systems is not known, although there is some indication that a propellant valve became blocked during the LunaH-Map mission because of iodine deposition (resulting from an excessive launch delay) and the thruster was not able to fire [308].

6.2. Safety and environmental considerations

Iodine is an essential trace element for life. However, molecular iodine is toxic in cases of excessive exposure through inhalation or ingestion, with a mean lethal dose of 2–4 g [309]. For large doses of several grams, iodine can cause burning of the mouth and throat, chest tightness, and even headaches [310]. It is a skin irritant and can even lead to tissue damage. Since iodine readily sublimates to form a corrosive vapor, appropriate safety precautions must be taken when handling iodine: including when cleaning vacuum equipment such as chambers or pumps that have been exposed to iodine. Typical protective gear can include gloves, safety goggles, and respirator masks to prevent inhalation of iodine vapor or contaminated dust [310].

From an environmental perspective, depletion of stratospheric ozone has been proposed as a potential impact of iodine propulsion. Iodine can catalyze ozone destruction in a similar way to the other halogens chlorine and bromine [311]. Feng *et al* [312] modeled ozone depletion in a scenario with widespread use of iodine propulsion numerically using a general circulation model of the atmosphere. They initially assumed emission of 8 metric tons of I_2 per year (corresponding to an annual launch of 40 000 satellites each with 0.2 kg of propellant), resulting in a $\sim$0.1 part per trillion volume increase in stratospheric iodine and 0.02% decrease in global average stratospheric ozone. However, iodine concentration increases were found to scale nearly linearly with 10 to 100-fold further increases in emissions, leading to significant stratospheric ozone depletion in the latter case. Such cases are currently however very far from being achieved or even projected within the space industry. Furthermore, iodine propulsion cannot conceivably alter iodine levels in the troposphere appreciably, with estimates of natural oceanic emissions ranging from 114 000 to 550 000 metric tons per year [313].

In their study, Feng *et al* assumed that iodine from electric propulsion in low-Earth orbit would ultimately descend to lower layers of the atmosphere rather than escape to space. The question of which possibility dominates has been explored for other propellants, such as mercury, by Fourie *et al* [314]. Depending on the thruster orientation and specific impulse, ions may or may not achieve escape velocity. For example, for orbit raising at 800 km, ions with an exhaust velocity less than 1.8×10^4 m s^{-1} remain gravitationally bound to the Earth. Even where they exceed the escape velocity, ions are typically trapped by the geomagnetic field, bouncing between polar magnetic mirror points. Repeating the calculation in appendix A.2 of Fourie *et al* for iodine gives a maximum gyroradius of 1.4 km (much smaller than the Earth's radius). Ions are likely to be neutralized on reaching lower altitudes near the poles, limiting the chance that they will retain sufficient energy to escape. This likelihood contrasts with that of iodine originating in the troposphere reaching the stratosphere; this iodine is contained within short-lived gases severely limiting transport to higher altitudes [311, 313].

7. Future research and remaining challenges

7.1. Material compatibility

As highlighted in section 4.1, iodine can react with many common materials. While a number of recent works have been dedicated to the study of iodine-material compatibility, it is clear that further research is still needed. In particular, three main research directions can be identified. Firstly, there is a lack of uniformity of results in the literature which makes it challenging to extract general conclusions for certain substances (e.g. gold). Similarly, there is a strong discrepancy between corrosion rates for some substances, which implies that test conditions are not identical (e.g. the state of the test material surface, the background pressure and temperature, the quality of measurements, etc).

Secondly, there is a lack of tests and data for high-temperature iodine exposure. Even if some materials may be compatible with iodine at low temperatures, this can change at elevated temperatures where reaction rates can increase exponentially. This may be particularly relevant to many iodine applications, since as discussed in section 7.6 below, measurements in low-pressure iodine discharges indicate strong gas heating with temperatures reaching as high as 1500 K in some cases. Furthermore, vibrationally excited iodine, electronically excited iodine, and even positive or negative iodine ions, may increase reaction rates further or even promote new reaction pathways: as is well-known with other molecular substances such as hydrogen used for reducing iron ores (see for example [315]). While there is some information on high-temperature corrosion of iodine in the context of nuclear applications, this is usually limited to only a few materials (e.g. stainless steel, zirconium alloys, refractory metals, and some ceramics).

Finally, it should be noted that most previous research has only considered a few standard materials with little innovation regarding novel material options. While this is natural for pure metals and their alloys, there are many possible ceramics, ceramic coatings, or polymer coatings that could be tested and very little, if any, existing literature on their iodine compatibility. This point is also of specific relevance to electric propulsion, since thermionic insert materials (such as barium oxide, BaO) for hollow cathodes (see section 7.2) have thus far failed to demonstrate long-term stable operation with iodine [257]. Since the number of possible materials that could be studied is potentially vast, it may be useful to consider several practical or regulatory constraints to narrow the solution space. For example, some materials, such as refractory metals or their compounds, may survive reentry and pose a collision risk on the ground [316], whereas other materials, such as platinum or palladium, have a strong cost barrier.

7.2. Hollow cathodes

While several iodine hollow cathode prototypes have been developed and tested, most, if not all, have failed to achieve stable long-term operation [257, 317–319]. This currently represents one of the greatest challenges facing wide-spread adoption of iodine as an alternative propellant within the space industry. Previous work with iodine Hall thrusters has shown that although thruster and neutralizer structural materials can be found or designed for iodine compatibility, the thermionic insert material in hollow cathodes is not compatible [320]. Similarly, several subsequent research studies focused on iodine neutralizers have encountered problems associated with depletion or degradation of the insert due to chemical reactions or sputtering. Insert materials tested include lanthanum hexaboride (LaB_6) [321], dodecacalcium hepta-aluminate electride (C12A7) [322–324], tungsten doped with La_2O_3 (WL20) [325], and tungsten matrix inserts impregnated with $BaO–CaO–Al_2O_3$ (see for example [320]). Overall, the longest duration operation observed was less than 100 h [257]. It is therefore clear that further research is needed in this area. As a short-term alternative however, the use of a noble gas hollow cathode (e.g. xenon or krypton) with an iodine thruster has been demonstrated [320].

There is also a more subtle challenge that some iodine hollow cathodes may encounter: negative atomic iodine ions (I^-; see also section 7.5 below and [319]). Previous experiments [286] have shown that at sufficiently high pressures (above about 1 Pa), significant quantities of negative ions can be formed and the plasma discharge becomes electronegative. This occurs not only because the electron affinity of atomic iodine is very high, but also because dissociative electron attachment reactions are favored at higher pressures where the electron temperature is lower (see section 3.7). As the pressure inside hollow cathodes can be between 100 and 2000 Pa, negative ion production could therefore strongly reduce electron extraction capability. Thus, even if iodine-compatible insert materials can be found or developed, the unique iodine plasma chemistry may anyway limit or affect hollow cathode operation. At present, it is difficult to assess the impact negative ion formation may have, since both electron and heavy species impact collisional detachment would also occur (see section 3.5). Therefore, additional research is needed to study the underlying iodine plasma chemistry in neutralizer-relevant conditions.

7.3. Lifetime testing

Aside from neutralizer degradation (see section 7.2), general lifetime testing of complete iodine electric propulsion systems presents several practical challenges, some of which have recently been summarized in [217, 326]. For example, iodine can react with vacuum chamber wall materials leading to deposition or even chemical reactions (such as the formation of metal iodide layers). Similarly, iodine can react with other vacuum equipment and even corrode pump components. Typically, a special filter system is needed to prevent this, while periodic vacuum chamber cleaning and maintenance may be necessary. Cold heads or traps can be used to achieve low base pressures by forcing iodine to deposit, but again, this may require periodic cleaning. These factors make testing with iodine significantly more difficult than inert gases like xenon, and since some high-performance electric propulsion systems are required to operate for more than 10 000 h, lifetime testing or qualification of iodine thrusters is a costly and time-consuming process.

Other testing challenges noted in [217, 326] are not necessarily unique to iodine, but may be exacerbated by it. For example, a high level of back-sputtered vacuum chamber material was observed which caused degradation and increased erosion of propulsion system components. Furthermore, the frequent vacuum chamber maintenance cycles introduced other unexpected facility effects, such as an increased exposure to water vapor or oxygen which can chemically react with some thruster components, deposited iodine, or even sputtered material. Because of the high-energy ion beam produced by most electric propulsion systems, a beam dump is needed to prevent direct impingement and damage to vacuum chamber walls. However, sputtering rates with carbon-carbon (which typically has a very low sputter yield) beam dumps exhibited volatility with irregular sputtering patterns. By comparison, molybdenum was found to be a more reliable material, although strong sputtering still occurred.

As iodine is still an emerging propellant, there is limited available information on lifetime testing, with the most detailed investigation described in [217] for the NPT30-I2 gridded ion thruster. This study found that thruster life was limited only by the amount of system propellant, followed by the filament neutralizers which are currently the most life-limiting component (each having an expected operating duration of about 1260 h). Failure of the neutralizer occurs predominantly due to material evaporation that is exacerbated by ion sputtering (a hypothesis confirmed with a simplified model). The filament also reacted with atmospheric oxygen and changes in lifetime (indicated by increased filament resistance: a useful proxy measurement for filament cross-sectional area) were correlated with each scheduled vacuum chamber maintenance cycle. Consequently, future testing should aim to use a partitioned vacuum chamber with a gate valve such that the thruster can remain under vacuum while cleaning of the main chamber is performed. For gridded ion thrusters, grid erosion (see also section 4.4) is also of importance. The testing campaign in [217] indicates that grid lifetime is at least 5000 h, and metrology measurements show that the maximum increase in grid aperture size (due to ‘barrel erosion’) is less than 5%: inline with sputter model predictions. All other subsystems (such as propellant storage and flow control/distribution) are predicted to have a lifetime of at least 8000 h.

Testing of the BHT-600-I Hall thruster was conducted in [320], where a lifetime of at least 1174 h was demonstrated. Because of difficulties with operating an iodine hollow cathode (see section 7.2), a xenon-fueled cathode was used instead. Similar thruster performance was found for both iodine and xenon thruster propellants over long firing durations, but again, several facility effects were identified and specific precautions implemented. For example, grafoil was attached to the vacuum chamber walls with graphite nuts. This not only decreased back-sputtered material, but also reduced the interaction of atomic and molecular iodine with the chamber wall material, since iodine can sputter the natural oxide layer of the walls and lead to direct corrosion.

Aside from challenges with iodine testing in terms of the vacuum equipment, there are also associated testing challenges since measurement equipment/diagnostics compatible with iodine are not always available. This includes mass flow rate controllers, pressure gauges, and even electrostatic probes such as Langmuir probes, retarding field energy analyzers, or ion flux probes. For example, Habl *et al* [196] developed an ion flux probe enabling spatial iodine ion beam measurements to be performed. To protect the system from iodine, the electrical measurement board was coated in urethane polymer, isolating its tracks and components from contamination. Connectors were covered in disposable metallic foil after placement in the chamber, and PTFE-based grease was used on the stepper motor bearings. After operation with iodine, the whole instrument was cleaned with alcohol and the probe collecting surfaces were polished to remove any possible thin film deposits. This latter point is important since as discussed in section 4.3, probe current–voltage characteristics can change due to SEE from any deposited iodides [199]. It should be noted though that optical methods would not suffer the same challenges and may be a valuable alternative or complementary tool for diagnosing iodine plasmas (see for example [26, 98, 227]).

7.4. Flow control and long-term storage

Since iodine is a solid under typical ambient conditions (see section 2), an immediate challenge is flow control. At a temperature of 300 K, the sublimation rate of iodine is very low and the vapor pressure is less than 100 Pa, making it difficult to achieve the mass flow rates required by most electric propulsion systems. The flow control solution to emerge is controlled heating of iodine to increase the sublimation rate and vapor pressure [2, 153]. Typically, heaters are placed on the propellant storage tank together with a temperature sensor. A thermal control algorithm then controls the heater so that the desired temperature can be reached/maintained. If the propulsion system is correctly designed, waste heat from the thruster and power electronics can be used to provide partial heating [2]. However, care needs to be taken to ensure that the temperature does not exceed 113.7 °C as iodine undergoes a phase transition to a liquid above this value. As the tank is directly heated rather than the iodine itself, the tank and iodine temperatures may not be equal. This is particularly true if solid iodine crystals are loaded into the tank, as thermal contact could be unreliable and nonuniform. While not a serious issue for ground-based experiments, it can pose potential problems in space.

The use of solid iodine crystals can also create other possible problems. For example, due to launch vibrations or spacecraft motion in orbit, iodine crystals can break or move around, possibly causing damage to the propulsion system or a variation in thermal contact with the tank walls. One proposed solution is to embed the iodine into a porous ceramic block that is then placed inside the tank [2]. In this way, the iodine is strongly fixed and the ceramic block facilitates more consistent and uniform heat transfer. Together with controlled sublimation, the issue of propellant flow control and storage is therefore largely solved: with the exception perhaps of on/off flow control to prevent iodine leakage. Some propulsion systems have made use of a flow control valve, but as this includes moving parts, iodine deposition can potentially cause valve sticking. This was the problem thought to have occurred on the LunaH-Map spacecraft and which consequently prevented the onboard iodine thruster from firing [308].

An alternative solution for on/off flow control already successfully demonstrated in space [2] is a passive thermal control valve. Here, a short flow distribution line containing a small orifice (<1 mm in diameter) connects the propellant storage tank with the downstream plasma source. When the thruster fires, the orifice becomes hot and iodine deposition is prevented, allowing propellant to flow freely. When the thruster is off though, the orifice is cooler and iodine deposits blocking further flow. One problem with this approach however, is that even when the thruster is not firing, the sublimation rate of iodine in the orifice is not zero. Nonetheless, ground experiments with the NPT30-I2 estimated an iodine leakage rate of less than 3 g per year [2]. While low, this may cause challenges with long-term propellant storage in space: particularly if the satellite temperature rises and causes the sublimation rate to increase.

For micropropulsion systems, sufficiently high mass flow rates can easily be produced with moderate propellant heating to temperatures below the melting point of iodine. However, for larger propulsion systems (such as kW-class Hall or cusp field thrusters) this may be insufficient to achieve the required flow rates and overcome various pressure drops in the flow distribution system, particularly as the vapor pressure just before melting is only about 12 kPa. Consequently, higher temperatures are needed implying that iodine may be present in solid, liquid, and gaseous phases. Additional research is needed to investigate this in more detail.

Further research is also needed to develop viable solutions to enable in-space refueling, which is an area attracting increased attention. For example, Ponti *et al* [252] have recently proposed a novel rechargeable iodine propulsion concept. Here, the use of special iodine propellant cartridges are envisioned which could be removed and replaced via in-orbit satellite servicing, hence allowing mission extension.

7.5. Negative ion formation and loss

As early as in 1925, Mohler [81] observed that in an iodine discharge, I^- is created through Dissociative Electron Attachment (DEA) ($I_2 + e^- \rightarrow I + I^-$) rather than through dissociation into positive and negative ions, and that DEA occurs even at very low electron energies. This peculiarity is explained by the fact that the electron affinity of atomic iodine is 3.059 eV [135], which is almost double the dissociation energy of the iodine molecular ground state (1.542 eV [61]). In this configuration, the threshold energy for the production of negative ion fragments via DEA is lower that that for pure dissociation processes [124]. The potential energy curves of the $I_2(X\ ^1\Sigma_g^+)$ ground state, the anionic molecular ground state I_2^-, and an anionic excited state I_2^{-*} are schematically illustrated in figure 52.

DEA is a two step process whereby the molecule is first placed into an intermediate repulsive excited ionic state ($I_2 + e^- \rightarrow I_2^{-*}$) which subsequently dissociates into $I^-(^1S_0)$ and $I(^2P^o_{3/2})$. The lowest crossing point between I_2 and I_2^{-*} potentials is only a few hundredths of an eV high [131] which explains the magnitude of the DEA cross-section for iodine, the resonances being caused by several I_2^{-*} potentials crossing the I_2 ground state for different energies (only one has been represented in figure 52). A better understanding of the I_2^- electronic potentials would help to clarify the observed discrepancies between all of the DEA cross-section data plotted in figure 21. Note that Ambalampitiya *et al* [31] assumed that the atomic state created was $I(^2P^o_{1/2})$, but this is in contradiction with most works on electron attachment in other halogens (see for example Ayala *et al* [131]).

As highlighted in recent experiments by Esteves *et al* [286], negative ion formation can be important even at low pressures. For example, the electronegativity ($\alpha = n_n/n_e$ where n_n and n_e are the negative ion and electron densities respectively) of an iodine ICP was observed to surpass 1 in some regions of the discharge for pressures above about 1 Pa. This indicates that negative ion creation and loss processes

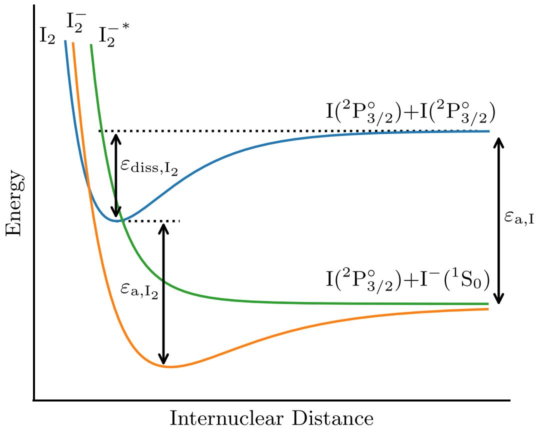

Figure 52. Schematic representation of various iodine potential energy curves and their respective dissociation limits: I_2 is the molecular ground state, I_2^- is the anionic molecular ground state, and I_2^{-*} is the first electronically excited state of I_2^-. Here $\varepsilon_{diss,I_2} = 1.542$ eV is the dissociation energy of I_2, $\varepsilon_{a,I} = 3.059$ eV is the electron affinity of I, and $\varepsilon_{a,I_2} = 2.52$ eV is the electron affinity of I_2.

need to be included when modeling such systems, and that care must be taken with the pressure level when operating an iodine thruster.

When the pressure increases, molecular negative ions I_2^- and I_3^- are known to be created by clustering reactions between I^- and atomic or molecular iodine [82, 327]. For example, Woolsey *et al* [91] used a Langmuir probe together with orbital motion limited theory and found an electronegativity above 2000 resulting in a nearly electron-free ion–ion plasma (I_2^+-I_3^-; produced by allowing the plasma in the Faraday dark space of a DC glow discharge to diffuse into a side-arm at pressures between 27 and 133 Pa). However, no cross-section data is available for these creation processes and, furthermore, hollow cathodes typically operate at pressures between approximately 100 and 2000 Pa, which suggests that molecular negative ion formation may be particularly relevant to such discharges (a fact largely ignored so far).

Finally, as mentioned above and in section 3, large uncertainties remain regarding not only the formation processes of negative ions, but also their destruction mechanisms (e.g. ion–ion recombination, charge-exchange, or detachment) in the plasma volume.

7.6. Anomalous gas heating

During the operation of most electric propulsion systems, there is inevitable thruster heating due to plasma-wall heat transfer. For example, the discharge chamber temperature measured in the NPT30-I2 gridded ion thruster is 443 K [2], while the channel temperature in Hall thrusters routinely reaches 700–900 K [328, 329]. Because of either heat transfer from the thruster walls, and/or plasma-gas collisional processes, the neutral propellant gas temperature increases above its input value. For noble gases such as xenon, this temperature increase may be similar to that of the thruster walls, and relevant collisional processes include electron-neutral elastic scattering, ion-neutral collisions, collisional quenching of excited states, and the formation of high-energy neutrals due to wall recombination. With iodine however, the measured gas temperature in some experiments can be much higher than the wall temperature and even exceed 1500 K [26, 94]. Furthermore, the temperature of I and I_2 species may be different [26], particularly at low pressures where the collision frequency is too low to ensure thermodynamic equilibrium.

In [26, 94], two-photon laser induced fluorescence (TALIF) was used to measure the temperature of neutral atomic iodine in an RF reference cell and a gridded ICP source. In both cases, atomic iodine temperatures were observed to increase with power level and operating pressure, and attained values between 300 and 1800 K. The consequence of high neutral temperatures can easily be seen by considering a simple model of neutral gas flow through a plasma system

$$\dot{m} = \frac{1}{4} M n_g \bar{v}_g A_{eff}, \tag{52}$$

where $\dot{m}$ is the input mass flow rate, M is the propellant atomic/molecular mass, n_g is the average system gas density, $\bar{v}_g = \sqrt{8k_B T_g/\pi M}$ is the gas thermal speed with T_g the gas temperature, and A_{eff} is an effective loss area (accounting for any reduced flow conductance due to the thruster geometry). For a

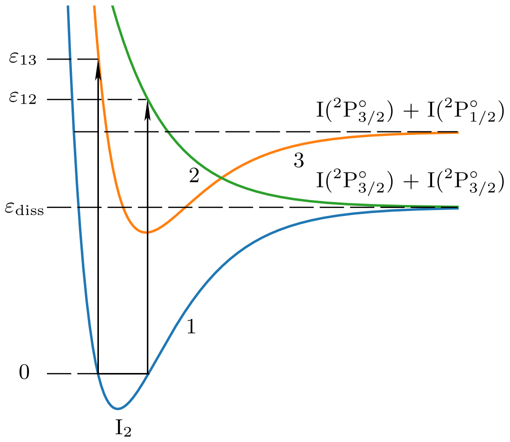

Figure 53. Illustration of example electron impact dissociation pathways of molecular iodine. Here ε_{12} and ε_{13} represent energies transferred to the iodine molecule and which initially take it to either the repulsive state labeled 2, or the bound state labeled 3.

fixed mass flow rate, $n_g \propto 1/\sqrt{T_g}$. Thus, gas heating leads to neutral depletion inside the thruster (see also [330] for a more detailed model). Since many important collisional reaction rates are proportional to the neutral density (such as ionization or dissociation), depletion can cause a change in system performance. In particular, as the neutral density decreases, the electron temperature in the discharge usually increases, which then leads to a larger plasma sheath potential, higher plasma kinetic energy losses to the walls, and therefore increased power consumption to achieve a target thrust level.

At present, these anomalously high gas temperatures are not well understand, but are thought to occur because of the unique iodine plasma chemistry. Initial calculations suggest that energy transfer during electron-neutral elastic scattering is far too small to explain the elevated temperatures observed, but rather kinetic energy release (KER) in several dissociation and neutralization reactions may be responsible [292]. For example, consider the general electron impact dissociation reaction given by

$$I_2 + e^- \longrightarrow I + I^* + e^-, \tag{53}$$

where I* represents a possible excited state because of the various reaction pathways and resulting dissociation products that could be produced (see figure 53). Although the threshold energy for dissociation, $\varepsilon_{\rm diss}$, of I_2 is 1.542 eV, electrons can initially transfer more energy (typically known as the vertical excitation energy), ε_e, to the iodine molecule and place it into a bound state, or a repulsive state where the energy exceeds the molecular dissociation energy. The molecule then splits and releases the energy difference, $\Delta\varepsilon = \varepsilon_e - \varepsilon_{\rm diss}$, which either goes to excite one of the atomic iodine atoms, and/or is shared as kinetic energy amongst the products ($\varepsilon_{\rm ker}$, referred to as KER). As the KER can be of the order of a few eV [124], hot neutral dissociation fragments are created that can subsequently lead to gas heating via heavy particle collisions. Indeed, energy release during dissociation has been implicated in gas heating in hydrogen [124, 331], oxygen [332], and chlorine discharges [333]. The exact KER is difficult to establish because of missing information associated with the initial electron energy transfer, and the different subsequent dissociation pathways. Nonetheless, for $\varepsilon_e > \varepsilon_{\rm diss}$, and assuming that no dissociation products are formed in an excited state, one would expect $\varepsilon_{\rm ker} > 0$ eV.

Initial unpublished calculations of KER due to electron-impact dissociation have been performed by Nicolas Sisourat and his team at LCPMR for different iodine gas temperatures. The KER has an energy distribution that depends on the specific intermediate excitation state and subsequent dissociation products. Although gas temperature is found to have little effect, the dissociation pathway strongly influences the resulting energy release. KER distributions typically show a spread between 0 and 1 eV per atom, with distribution-averaged values as low as 0.1 eV, and as high as 0.5 eV, depending on the specific dissociation pathway.

KER can also occur in other dissociation reactions, such as dissociative electron attachment (see reaction C5 in table 7). As iodine has an electron affinity of $\varepsilon_{a,I} = 3.059$ eV that is higher than the molecular dissociation energy, a transient I_2^{-*} repulsive state can initially be produced even for low electron collision energies, before it dissociates. Since the electron is captured by one of the atomic iodine products, it cannot carry away any excess collision energy. Consequently, very hot neutral and negative ion fragments

Table 20. Example collisional processes that may produce hot fragments, together with an estimate of the kinetic energy release (see also [292]).

Reaction	$\varepsilon_{\mathrm{ker}}$ (eV)
$\mathrm{I_2 + e^- \longrightarrow 2I(^2P^\circ_{3/2}) + e^-}$	>0
$\mathrm{I_2 + e^- \longrightarrow I(^2P^\circ_{3/2}) + I^-}$	>0.5
$\mathrm{I_2 + e^- \longrightarrow I(^2P^\circ_{3/2}) + I^+ + e^-}$	>0
$\mathrm{I_2^+ + e^- \longrightarrow 2I(^2P^\circ_{3/2})}$	8.27
$\mathrm{I^+ + I^- \longrightarrow 2I(^2P^\circ_{3/2})}$	7.39
$\mathrm{I_2^+ + I^- \longrightarrow 3I(^2P^\circ_{3/2})}$	4.71
$\mathrm{I(^2P^\circ_{3/2}) + I(^2P^\circ_{1/2}) \longrightarrow 2I(^2P^\circ_{3/2})}$	0.94
$\mathrm{I_2 + I(^2P^\circ_{1/2}) \longrightarrow I_2 + I(^2P^\circ_{3/2})}$	0.94

can be produced. The KER can be estimated by performing a collision energy balance

$$\varepsilon_{\mathrm{e}} + \varepsilon_{\mathrm{I_2}} + U_{\mathrm{I_2}} = \varepsilon_{\mathrm{I}} + \varepsilon_{\mathrm{I^-}} + U_{\mathrm{I}} + U_{\mathrm{I^-}}, \tag{54}$$

where $\varepsilon_{\mathrm{I_2}} \approx 0$ is the kinetic energy of the molecule, ε_{I} and $\varepsilon_{\mathrm{I^-}}$ are the kinetic energies of the neutral and negative ion fragments, and $U_{\mathrm{I_2}}$, U_{I}, and $U_{\mathrm{I^-}}$ are the internal energies of the molecule, neutral, and negative ion. Calculations suggest that the neutral fragment is in the excited $^2\mathrm{P}^\circ_{1/2}$ state (with a threshold energy $\varepsilon_{\mathrm{exc_1}}$) [31], and thus $U_{\mathrm{I_2}} - U_{\mathrm{I}} - U_{\mathrm{I^-}} = \varepsilon_{\mathrm{a,I}} - \varepsilon_{\mathrm{diss}} - \varepsilon_{\mathrm{exc_1}}$. Using this in equation (54) and rearranging, we find

$$\varepsilon_{\mathrm{I}} + \varepsilon_{\mathrm{I^-}} \approx \varepsilon_{\mathrm{e}} + \varepsilon_{\mathrm{a,I}} - \varepsilon_{\mathrm{diss}} - \varepsilon_{\mathrm{exc_1}} = \varepsilon_{\mathrm{e}} + 0.574. \tag{55}$$

Thus, even if the initial electron energy is zero, the resulting KER is above 0.5 eV. Considering a typical electron temperature of 5 eV, and assuming an upper limit case where all kinetic energy is initially transferred to the molecule (i.e. $\frac{3}{2}T_{\mathrm{e}}$ on average), the KER could be as high as 8.074 eV. Similarly, consider the dissociative ionization reaction

$$\mathrm{I_2 + e^- \longrightarrow I + I^+ + 2e^-}. \tag{56}$$

Assuming that both neutral and ion fragments are in the ground state, and again performing a collision energy balance, the KER is estimated to be at least $\varepsilon_{\mathrm{ker}} = \varepsilon_{\mathrm{dissiz,I_2}} - \varepsilon_{\mathrm{diss}} - \varepsilon_{\mathrm{iz,I}} > 0$ eV.

Table 20 summarizes KER from the above reactions, together with several other reactions including: recombination between $\mathrm{I^+}$ and $\mathrm{I^-}$, recombination between $\mathrm{I_2^+}$ and $\mathrm{I^-}$, and collisional quenching of $\mathrm{I(^2P^\circ_{1/2})}$ with either I and $\mathrm{I_2}$. Not included in table 20 are vibrational–vibrational and vibrational–translational collisional relaxation processes, which are known to be important in some molecular plasmas [334]. Further research is needed to better understand which processes are responsible for anomalous gas heating, and how this affects system performance.

7.7. Missing collision cross-section and surface data

While we have provided a detailed iodine reaction set in section 3, there are a number of reactions still missing and for which little or no reliable cross-section or rate coefficient data exists (or for which there are strong inconsistencies). Similarly, and as already highlighted in section 4, iodine-surface data (such as sputter/SEE yields and surface recombination coefficients) is very sparse in the literature. It should also be noted that most cross-sections have only been computed theoretically/numerically and there is very little available experimental cross-section or swarm parameter data for validation. Table 21 summarizes some of the main iodine reactions for which data is missing or inconsistent.

While recent research has calculated and proposed cross-sections for various electron impact processes [31, 115], there is only a single set of known data for dissociation of molecular iodine, and this is only for energies below 10 eV which is insufficient (hence requiring extrapolation for higher energies; see also section 3.3.3). In addition, information on the specific dissociation pathways and reaction products, as well as the KER, is not known.

Another important process for which incomplete and inconsistent data exists is elastic collisions between electrons and atomic iodine. Firstly, only the total elastic scattering cross-section is known [31], while the elastic MTCS (which is important for calculating collisional drag and momentum exchange) is missing. Secondly, total elastic scattering cross-sections calculated with different theoretical methods disagree by as much as an order of magnitude below about 3 eV (see figure 13). Consequently, the electron-neutral total elastic scattering collision frequency may be over or underestimated depending on the data

Table 21. Important iodine reaction processes for which cross-section or rate coefficient data is either unknown, missing, or inconsistent. Here J and J' denote rotational excitation levels of I_2 such that $J' > J$.

Reaction	Process	Comment
Electron impact scattering: atomic iodine		
$I(^2P^\circ_{3/2}) + e^- \longrightarrow I(^2P^\circ_{3/2}) + e^-$	Total elastic scattering	Disagreement between calculations below 3 eV
$I(^2P^\circ_{3/2}) + e^- \longrightarrow I(^2P^\circ_{3/2}) + e^-$	Elastic momentum transfer	No data
$I(^2P^\circ_{1/2}) + e^- \longrightarrow I(^2P^\circ_{1/2}) + e^-$	Elastic momentum transfer	No data
$I(^2P^\circ_{1/2}) + e^- \longrightarrow I^+ + 2\,e^-$	Ionization	Empirical estimate only
$I^+ + e^- \longrightarrow I^{2+} + 2\,e^-$	Double ionization	No data
$I^- + e^- \longrightarrow I(^2P^\circ_{1/2}) + 2\,e^-$	Detachment	Only one calculation with a high cross-section
Electron impact scattering: molecular iodine		
$I_2(J) + e^- \longrightarrow I_2(J' > J) + e^-$	Rotational excitation	No data
$I_2 + e^- \longrightarrow 2\,I(^2P^\circ_{3/2}) + e^-$	Dissociation	No data above 10 eV
$I_2 + e^- \longrightarrow I(^2P^\circ_{3/2}) + I(^2P^\circ_{1/2}) + e^-$	Dissociation	No data
$I_2 + e^- \longrightarrow 2\,I(^2P^\circ_{1/2}) + e^-$	Dissociation	No data
$I_2 + e^- \longrightarrow I(^2P^\circ_{1/2}) + I^-$	Dissociative attachment	Disagreement between calculations Uncertainty in the resulting neutral atomic state
Ion-neutral collisions		
$I + I_2^+ \longrightarrow I^+ + I_2$	Charge-exchange	Data only for the reverse reaction
$I + I^{2+} \longrightarrow I^+ + I^+$	Charge-exchange	No data
$I_2 + I^{2+} \longrightarrow I_2^+ + I^+$	Charge-exchange	No data
$I + I^- \longrightarrow I_2^-$	Clustering	No data
$I_2 + I^- \longrightarrow I_3^-$	Clustering	No data

set used. Furthermore, below 2 eV, the total elastic scattering cross-section for atomic iodine is much higher even than that for molecular iodine.

8. Conclusions

Despite being proposed for space propulsion applications as early as 1960 [218], iodine was only seriously considered as a propellant several decades later in 2000 when it became apparent that xenon may not be able to meet growing space industry demand in the future [21, 22]. Consequently, it is only within the last 15 years or so that strong research interest has emerged. While a significant amount of work has been performed during this time, there are still several difficulties that must be overcome before iodine becomes a widespread propellant option within the space community. Although several challenges were identified in section 7, it is worth emphasizing that these challenges do not appear to represent physical or technical barriers to iodine usage: with the exception perhaps of iodine-material compatibility. Appropriate materials for the thruster subsystem itself have been found or developed [2, 174, 176], but iodine-compatible hollow cathode neutralizers remain a strong concern [257, 317]. Furthermore, the high gas temperatures observed in several iodine plasmas [26, 59, 94] may increase chemical reaction rates with some materials and alter the conclusions of previous iodine-material studies [174].

It is worth reiterating that iodine electric propulsion systems have been successfully developed and continuously flown in space since 2020 [2]. Thus, until feasible iodine-fueled hollow cathodes are developed, we note that thermionic filament and RF neutralizer solutions already exist [2, 109, 233, 257]. For some propulsion technologies, such as ambipolar thrusters [240], no neutralizer is required and so this problem is avoided altogether. For high-performance propulsion technologies that require large neutralizer currents, such as Hall thrusters, a short-term solution is the use of an iodine-fueled thruster and a xenon- or krypton-fueled hollow cathode. Since the mass flow rate required to operate a hollow cathode is typically between 5% and 10% of the main thruster mass flow rate [3], this still offers significant advantages over a full xenon system. For example, less xenon (or krypton) is needed, and both the size and mass of the propellant tanks is reduced [172]: important considerations for small satellites and satellite constellations.

While much of the recent research with iodine plasmas has been driven by space propulsion applications, there are several ground-based industrial applications of importance that can leverage many of these developments. For example, atomic and molecular plasma chemistry data is relevant to the operation and numerical modeling of iodine etching reactors [23, 270, 335]. Furthermore, lifetime testing and iodine-material compatibility studies provide important information for understanding iodine plasma-surface interactions, long term operation of vacuum systems, and the appropriate design of plasma processing reactors. Likewise, materials processing studies can benefit the propulsion sector through the development or discovery of novel materials that are resistant to iodine.

As noted previously in several other topical reviews [187, 257, 336], electric propulsion systems, as well as plasma processing reactors, are complex devices and development requires a multi-disciplinary approach that not only considers plasma physics and gas dynamics, but also material science. A collaborative approach is therefore needed to advance iodine plasma technology further and address some of the challenges highlighted in this review. Iodine has the potential to be a game-changing propellant for the space industry and to both enable new missions, while ensuring a sustainable space environment around the Earth. Iodine has a low cost, a high global production output, is easier to handle and transport than xenon, and can provide a higher plasma discharge efficiency. Solutions currently exist for iodine delivery and flow control, and a number of compatible materials have been found. Furthermore, a reasonable iodine plasma chemistry reaction set with known collision cross-sections exists and has been validated with several experiments [26, 28, 287, 288]. In closing, we note that iodine plasma research could also serve as a model for the development of other alternative propellants currently being investigated such as water [337–339], bismuth [245], and even air [340].

Data availability statement

The data that support the findings of this study are openly available at the following URL/DOI: https://doi.org/10.5281/zenodo.17348832 [32].

Acknowledgments

The authors would like to thank Dmytro Rafalskyi, Lui Habl, Oliver Jia-Richards, Kristof Holste, Rainer Dressler, Akhiro Matsutani, Harin Ambalampitiya, Klaus Bartschat, Ayushi Agrawal, Mirko Magarotto, Weizong Wang, Victor Desangles, Nicolas Sisourat, and Max Vaupel for several useful discussions on iodine plasmas and for providing valuable feedback on this review paper. The authors also thank Ayushi Agrawal and Nicolas Sisourat for providing supplementary data.

Appendix A. Term symbols for atomic iodine

Overview

The ground state of atomic iodine has an electron configuration of $[\mathrm{Kr}]\,4\mathrm{d}^{10}\,5\mathrm{s}^2\,5\mathrm{p}^5$, with the seven valence electrons in the outermost (fifth) shell. Like the other halogens, iodine is one electron short of a full octet and is hence an oxidising agent that easily reacts with many other elements. Table 22 provides several fundamental properties.

Ground state and first excited state

The iodine atom has a transition from the fundamental state $5\mathrm{s}^2 5\mathrm{p}^5\ {}^2\mathrm{P}^\circ_{3/2}$ towards the first excited state $5\mathrm{s}^2 5\mathrm{p}^5\ {}^2\mathrm{P}^\circ_{1/2}$ at 7602.9762(2) cm^{-1} (approximately 0.9426 eV) [341], or around 1.3149 μm in the infrared (IR). The splitting between both states is due to spin–orbit coupling. The transition between these states is forbidden with respect to electric dipole radiation but allowed mainly by magnetic dipole radiation. This transition has been studied by Luc-Koenig *et al* [342] by using Fourier transform spectrometry and by Ha *et al* [343] by measuring the absorption spectra of the transition with a tunable near-IR diode laser. This latter technique has also recently been used as a novel optical diagnostic in iodine CCPs [26, 59].

Table 22. Iodine atom and ion properties.

Mass	126.904 47(3) u
Atomic number	53
Stable isotope	127
Nuclear spin	5/2
Electron configuration	[Kr] $4d^{10}\,5s^2\,5p^5$
Enthalpy of formation	106.76(4) kJ mol^{-1}
First ionization energy	10.451 26 eV
Electron affinity	3.059 0465(37) eV
Polarizability	32.9 ± 1.3 a.u
Pauling electronegativity	2.66
Van der Waals radius	198 pm
Ionic radius (I^-)	206 pm

Higher excited states

The excited levels of the $5s^25p^4nl$ type configuration of I are divided into several groups, each of which corresponds to a level of the $5s^25p^4$ ion: $^3P_{2,1,0}$, $^1D_0$ or $^1S_0$ (with $nl \in \{6s, 7s, 6p, 7p, 5d, 6d, 4f\}$). In 1962, Minnhagen [24] interpreted the set of known levels through the pairwise coupling scheme

$$\langle \left(\left\{ p^4 \left(S_c, L_c \right) J_c l \right\} K s \right) J \rangle, \tag{57}$$

which is the most appropriate to describe the level distribution in some configurations of the iodine spectrum [344]. Except for the degenerated upper level of the ground state (see previous subsection), a general excited level of atomic iodine can be written as

$$5s^2 5p^4 \left(^{2S_c+1}L_{cJ_c} \right) \; nl \quad ^{2s+1}[K]_J, \quad \text{if even}, \tag{58}$$

$$5s^2 5p^4 \left(^{2S_c+1}L_{cJ_c} \right) \; nl \quad ^{2s+1}[K]^{\circ}_J, \quad \text{if odd}, \tag{59}$$

where S_c, J_c, and L_c are the total spin, total angular momentum, and total orbital quantum numbers of the core electrons respectively, while $\boldsymbol{K} = \boldsymbol{J}_c + \boldsymbol{l}$ and $\boldsymbol{J} = \boldsymbol{K} + \boldsymbol{s}$ are quantum numbers built by using the orbital momentum, $\boldsymbol{l}$, and spin, $\boldsymbol{s}$, of the outer electrons.

Using Fourier transform spectrometry, Luc-Koenig *et al* [344] observed 440 structures and analyzed 130 hyperfine structures, giving the magnetic dipole and the electric quadrupole hyperfine structure constants for 37 even levels and 42 odd levels. Recently, absolute positions of atomic levels were revised after new energy measurements of two iodine excited levels using TALIF measurements by Esteves *et al* [94]. The atomic configurations, terms, and level energies from NIST are compared with those obtained in recent theoretical works by Ambalampitiya *et al* [31] and Agrawal *et al* [115] in section 3.2.3.

Hyperfine structure

The nuclear spin number of iodine is $I = 5/2$, meaning that any of the atomic levels of quantum number J is divided into several hyperfine sub-levels from $F = |I - J|$ to $F = I + J$. The positions of the hyperfine components, with respect to the fine structure energy level, are calculated as a function of the hyperfine structure constants A and B of the 2 levels, according to the Casimir formula [344]:

$$\Delta E = \frac{1}{2} A C + B \left[\frac{3C(C+1) - 4I(I+1)J(J+1)}{8I(2I-1)J(2J-1)} \right], \tag{60}$$

with $C = F(F+1) - I(I+1) - J(J+1)$.

Appendix B. Term symbols for molecular iodine

In a diatomic molecule, the rotational symmetry around the line connecting the two nuclei (the internuclear axis) acts as the quantization axis. The projections of the various electronic angular momenta onto this axis have well-defined values that are characteristic of the electronic state of the molecule. Each individual electron, described by a molecular orbital, is characterized by four quantum numbers: n, l, λ, and m_s, which respectively characterize the energy, the magnitude of the orbital angular momentum, the spin component, and the projection of these moments onto the quantization axis. The quantum number λ measures, in units of $\hbar$, the component of the orbital angular momentum on the nuclear axis and can

Table 23. Summary of selected low-lying electronic states of I_2 plotted in figure 5.

State	S	Λ	Ω	Parity	Dissociation limit
$X\,^1\Sigma_g^+$	0	0	0	g^+	$I(^2P^\circ_{3/2}) + I(^2P^\circ_{3/2})$
$A\,^3\Pi(1_u)$	1	1	1	u	$I(^2P^\circ_{3/2}) + I(^2P^\circ_{3/2})$
$C\,^1\Pi(1_u)$	0	1	1	u	$I(^2P^\circ_{3/2}) + I(^2P^\circ_{3/2})$
$B\,^3\Pi(0_u^+)$	1	1	0	u^+	$I(^2P^\circ_{1/2}) + I(^2P^\circ_{3/2})$

take any integer value, positive, negative, or zero, between $-l$ and l. Its absolute value is symbolized analogously to that of atoms, but with a lowercase Greek letter: σ, π, $\delta, \ldots$ Molecular multi-electron wave functions are constructed from a set of molecular orbitals. The ground state of I_2 is written as:

$$\left(\sigma_g 5s\right)^2 \left(\sigma_u 5s\right)^2 \left(\sigma_g 5p\right)^2 \left(\pi_u 5p\right)^4 \left(\pi_g 5p\right)^4, \, ^1\Sigma_g^+. \tag{61}$$

A given electronic configuration gives rise to different energy levels characterized by the total angular momentum vectors, $\vec{L}$, $\vec{S}$, and $\vec{J}$. However, the motion of the electrons occurs within the framework of a cylindrical symmetry defined by the internuclear axis of the molecule. Generally, the spin–orbit coupling of each individual electron is weak compared to other couplings, leading to a consideration of the orbital momentum of all the electrons on one hand and the resulting spin on the other.

Regarding the total orbital momentum, only the projection onto the internuclear axis of the molecule is a constant of motion. The component of the orbital angular momentum of all electrons on the molecular axis is $M_L \times \hbar$, where the quantum number M_L can take positive, negative, or zero integer values. The value of $\Lambda = |M_L|$ for the molecule is symbolized by a capital Greek letter: Σ, Π, Δ, etc depending on whether $\Lambda = 0, 1, 2, 3, \ldots$

The ensemble of electron spins has a resultant characterized by a quantum number $\vec{S}$, whose component also has a quantized value on the internuclear axis because the orbital motion of the electrons creates a magnetic field whose average direction is that of the molecular axis. The quantum number Σ, characterizing the projection of the resultant spin, can take $2S+1$ different values between $-S$ and $+S$. The total electronic momentum Ω along the internuclear axis for all the electrons of the molecule is in units of $\hbar$: $\Omega = |\Lambda + \Sigma|$. For each electronic energy state corresponding to a value of Λ and a determined value of S, Ω can take $2S+1$ different values, which correspond to $2S+1$ sub-energy levels. The quantity $2S+1$ is the multiplicity of the considered state. A molecular term is therefore represented by the symbol

$$^{2S+1}\Lambda_\Omega. \tag{62}$$

For a homonuclear molecule, the electron probability density must always be symmetric with respect to the midpoint between the nuclei, but the wave function itself can be symmetric 'gerade' or antisymmetric 'ungerade'. This symmetry is indicated by the subscript $_g$ or $_u$. For any given Σ state, a $^+$ or $^-$ index is used to denote the symmetry with respect to reflection in any plane passing through the two nuclei.

Traditionally, the electronic states of diatomic molecules are distinguished by different uppercase and lowercase letters: X is reserved for the ground state, A, B, C, etc are used to denote excited states in order of increasing energy characterized by the same multiplicity $(2S+1)$, and the lowercase letters a, b, c, etc are used for a different multiplicity. This convention is not always followed, as in our case for I_2, but also for N_2, where the ground state is $X\,^1\Sigma_g^+$ and the triplet electronic states are denoted $B\,^3\Pi_g$ and $C\,^3\Pi_u$.

Note that nuclear rotation is denoted by $\vec{R}$ and the total angular momentum is $\vec{J} = \vec{R} + \vec{\Omega}$, with the quantum number $J = R + \Omega$. In figure 5, we represent the different electronic states for the first four levels of I_2 using the notation explained above and summarized in table 23, with the shape of the potentials approximated by an empirical expression (the Morse potential). The values of the potential curve parameters for I_2 (i.e. the electronic energy (T_e), the vibrational constant (ω_e), the unharmonicity $(\omega_e x_e)$, the rotational constant for the $v = 0$ vibrational level (B_e), the equilibrium internuclear distance (R_e) and the dissociation energy for the $v = 0$ vibrational level (D_0)) can be found, for instance, in Lukashov's book *The Iodine Molecule* [61].

Finally, it should be mentioned that the various moments associated with the electron spin, the orbital momentum, and the momentum associated with rotation can be coupled in different ways depending on the internuclear distance. These different couplings are referred to as Hund's cases, distinguished by the letters (a), (b), (c), (d), and (e). These couplings are obtained by comparing the relative importance of electrostatic interactions, spin–orbit interactions, and spin-rotation coupling. The description of the states previously described corresponds to Hund's case (a), where the vectors $\vec{L}$ and $\vec{S}$ are decoupled by the electrostatic field of the nuclei and precess independently along the internuclear axis. The rotation does not disturb the coupling of the electronic motion to the internuclear axis, so Ω remains well-defined. $\vec{R}$ precesses around $\vec{J}$, and the molecule, as a whole, rotates around $\vec{J}$. The significant quantum numbers are S, Λ, Σ, Ω, and J.

For heavy nuclei, such as I_2, the spin–orbit interaction is significant enough that $\vec{L}$ and $\vec{S}$ are not decoupled by the field generated by the nuclei. This is Hund's case (c), and one then defines $\vec{J}_a = \vec{L} + \vec{S}$ and $\hbar\Omega$ as the projection of $\vec{J}_a$ onto the internuclear axis. The molecule rotates around $\vec{J}$ such that $\vec{J} = \vec{\Omega} + \vec{R}$. The significant quantum numbers are S, Ω, and J (but not Λ and Σ), and states are noted, for example, as ${}^3 0_{\mathrm{u}}^{+}$ where 0 designates Ω. However, if coupling (c) is not strictly satisfied, Σ, Π, Δ, etc are also applied, which is why, in the case of I_2, we find notations such as ${}^3\Pi(0_{\mathrm{u}}^{+})$, ${}^3\Pi(1_{\mathrm{u}})$, ${}^3\Pi(2_{\mathrm{u}})$, etc.

Electronic spectrum—transition rules

Electronic transitions are primarily of the electric dipole type. The selection rules are as follows if Hund's coupling case (a) is satisfied:

1. $\Delta\Lambda = 0, \pm 1$.
2. $\Delta S = 0$. As with atoms, this selection rule no longer applies when the nuclear charge increases.
3. $\Delta\varSigma = 0$; $\Delta\Omega = 0, \pm 1$. For transitions between multiplet components.
4. $+ \leftrightarrow +$; $- \leftrightarrow -$; $+ \not\leftrightarrow -$. This applies only to Σ - Σ transitions, so only Σ^{+} - Σ^{+} and Σ^{-} - Σ^{-} transitions are allowed.
5. g$\leftrightarrow$u ; g$\not\leftrightarrow$g ; u$\not\leftrightarrow$u.

For Hund's coupling case (c):

1. $\Delta S = 0$ which, as in case (a), is approximate.
2. $\Delta\Omega = 0, \pm 1$.
3. $0^{+} \leftrightarrow 0^{+}$; $0^{-} \leftrightarrow 0^{-}$; $0^{+} \not\leftrightarrow 0^{-}$ with 0 the Ω value.
4. g$\leftrightarrow$u ; g$\not\leftrightarrow$g ; u$\not\leftrightarrow$u.

Molecular ions

The same reasoning applies for homonuclear ions such as I_2^{+} and I_2^{-}, whose electronic configuration are respectively given by

$$\left(\sigma_{\mathrm{g}}5s\right)^2\left(\sigma_{\mathrm{u}}5s\right)^2\left(\sigma_{\mathrm{g}}5p\right)^2\left(\pi_u 5p\right)^4\left(\pi_g 5p\right)^3, {}^2\Pi_{u;3/2}, \tag{63}$$

and

$$\left(\sigma_{\mathrm{g}}5s\right)^2\left(\sigma_{\mathrm{u}}5s\right)^2\left(\sigma_{\mathrm{g}}5p\right)^2\left(\pi_{\mathrm{u}}5p\right)^4\left(\pi_{\mathrm{g}}5p\right)^4\left(\sigma_{\mathrm{u}}5p\right)^1, {}^2\Sigma^{+}_{\mathrm{u};1/2}. \tag{64}$$

Appendix C. Principle of detailed balance

For almost all collisional processes discussed in section 3, only forward reaction rate coefficients are known. These have either been computed through integration of an assumed Maxwellian energy distribution function over the relevant cross-sections, or have been taken directly from the literature. However, certain reverse reactions can be important, such as electron impact de-excitation of the ${}^2\mathrm{P}^{\circ}_{1/2}$ state. To find reaction coefficients for such processes, we make use of the principle of detailed balance [124], which effectively states that at equilibrium, the reaction rates of all forward and reverse processes are equal. Here, we employ this principle to explicitly establish rate coefficients for both de-excitation and three-body recombination. Consider the electron impact atomic excitation and de-excitation reactions given by

$$\mathrm{I}(i) + \mathrm{e}^{-} \longleftrightarrow \mathrm{I}(j) + \mathrm{e}^{-}, \tag{65}$$

where j and i label upper and lower excited states. At equilibrium, the forward and reverse rates are equal such that

$$n_{\mathrm{e}} n_i K_{\mathrm{exc},ij} = n_{\mathrm{e}} n_j K_{\mathrm{deexc},ji}, \tag{66}$$

with $K_{\mathrm{deexc},ji}$ the de-excitation rate coefficient. If atomic iodine is in LTE, then the relative density of excited states can be determined from Boltzmann statistics

$$\frac{n_i}{n_j} = \frac{g_i}{g_j} \exp\left(\frac{\varepsilon_{\mathrm{exc},j} - \varepsilon_{\mathrm{exc},i}}{k_{\mathrm{B}} T}\right), \tag{67}$$

where g_j and g_i are the degeneracies of the upper and lower excited states, $\varepsilon_{\mathrm{exc},j}$ and $\varepsilon_{\mathrm{exc},i}$ are the excitation threshold energies, and T is the temperature (see below). Combining equations (66) and (67) we obtain an expression for the reverse rate coefficient

$$\frac{K_{\mathrm{deexc},ji}}{K_{\mathrm{exc},ij}} = \frac{g_i}{g_j} \exp\left(\frac{\varepsilon_{\mathrm{exc},j} - \varepsilon_{\mathrm{exc},i}}{k_{\mathrm{B}} T}\right). \tag{68}$$

There is some ambiguity as to what temperature to use when applied to non-equilibrium systems, but as the excitation/de-excitation is due to collisions with electrons, typically $T = T_{\mathrm{e}}$. Consider now the electron impact ionization and three-body recombination reactions given by

$$\mathrm{I}\,(i) + \mathrm{e}^- \longleftrightarrow \mathrm{I}^+ + 2\mathrm{e}^-, \tag{69}$$

where I^+ is in the ground state. At LTE, the forward and reverse rates must again be equal such that

$$n_{\mathrm{e}} n_i K_{\mathrm{iz}} = n_{\mathrm{e}}^2 n_{\mathrm{I}+} K_{\mathrm{rec}}, \tag{70}$$

with K_{rec} the recombination rate coefficient and $n_{\mathrm{I}+}$ the positive ion density. Ignoring any molecular iodine species, we can use the Saha equation to express the densities as

$$\frac{n_{\mathrm{e}} n_{\mathrm{I}+}}{n_i} = \frac{2 g_{\mathrm{I}+}}{g_i} \exp\left(\frac{\varepsilon_{\mathrm{exc},i} - \varepsilon_{\mathrm{iz,I}+}}{k_{\mathrm{B}} T}\right). \tag{71}$$

Combining equations (70) and (71) we then find

$$\frac{K_{\mathrm{rec}}}{K_{\mathrm{iz}}} = \frac{g_i}{2 g_{\mathrm{I}+}} \exp\left(\frac{\varepsilon_{\mathrm{iz,I}+} - \varepsilon_{\mathrm{exc},i}}{k_{\mathrm{B}} T}\right). \tag{72}$$

As before, we typically set $T = T_{\mathrm{e}}$.

For some models, cross-sections for the reverse reaction are needed instead of the rate coefficient. Considering reaction (65) as an example, the principle of detailed balance in this case gives [124]

$$\frac{\sigma_{\mathrm{deexc},ji}\left(\varepsilon\right)}{\sigma_{\mathrm{exc},ij}\left(\varepsilon + \Delta\varepsilon_{ij}\right)} = \frac{g_i}{g_j}\left(\frac{\varepsilon + \Delta\varepsilon_{ij}}{\varepsilon}\right), \tag{73}$$

where ε is the electron energy, $\sigma_{\mathrm{exc}}(\varepsilon + \Delta\varepsilon_{ij})$ is the energy-dependent excitation cross-section, $\sigma_{\mathrm{deexc}}(\varepsilon)$ is the energy-dependent de-excitation cross-section, and $\Delta\varepsilon_{ij} = \varepsilon_{\mathrm{exc},j} - \varepsilon_{\mathrm{exc},i}$.

ORCID iDs

Trevor Lafleur 0000-0002-9926-2187
Benjamin Esteves 0000-0002-3724-4899
Cyril Drag 0000-0001-9247-3945
Anne Bourdon 0000-0003-3662-4651
Pascal Chabert 0000-0002-6211-4746
Luca Vialetto 0000-0003-3802-8001
Rawoof Shaik 0009-0002-4391-9634

References

[1] Kaiho T 2014 *Iodine Chemistry and Applications* (Wiley)
[2] Rafalskyi D *et al* 2021 In-orbit demonstration of an iodine electric propulsion system *Nature* **599** 411
[3] Goebel D M, Katz I and Mikellides I G 2023 *Fundamentals of Electric Propulsion* (Wiley)
[4] Gold H, Rulis R J, Maruna F A J and Hawersaat W H 1965 *Description and Operation of Spacecraft in Sert I ion Thrustor Flight Test, Nasa TM X-1077* (NASA)
[5] Beattie J and Matossian J 1990 Xenon ion sources for space applications *Rev. Sci. Instrum.* **61** 348
[6] Humble R W, Gary H N and Larson W J 1995 *Space Propulsion Analysis and Design* (McGraw-Hill)
[7] Stuhlinger E 1964 *Ion Propulsion for Space Flight* (McGraw-Hill)

[8] NIST 2021 Thermophysical properties of fluid systems *NIST Chemistry Webbook, SRD 69* (National Institute of Standards and Technology) (available at:https://webbook.nist.gov/chemistry/fluid/)

[9] Welle R 1990 Availability considerations in the selection of inert propellants for ion engines *Proc. 21st Int. Electric Propulsion Conf.* (Electric Rocket Propulsion Society) p IEPC-1990-2589

[10] Herman D A and Unfried K G 2015 Xenon acquisition strategies for high-power electric propulsion nasa missions *Proc. JANNAF SPS Subcommittee Meeting* (NASA Glenn Research Center) p GRC-E-DAA-TN23198

[11] McDowell J C 2020 The low earth orbit satellite population and impacts of the SpaceX Starlink constellation *Astrophys. J. Lett.* **892** L36

[12] Fazio N, Gabriel S, Golosnoy I O and Wollenhaupt B 2019 Mission cost for gridded ion engines using alternative propellants *Proc. 36th Int. Electric Propulsion Conf.* (Electric Rocket Propulsion Society) p IEC-2019-831

[13] Sandau R 2010 Status and trends of small satellite missions for Earth observation *Acta Astronaut.* **66** 1

[14] Figliozzi G 2021 NASA cubesat to demonstrate water-fueled moves in space (NASA) (available at: www.nasa.gov/centers-and-facilities/ames/nasa-cubesat-to-demonstrate-water-fueled-moves-in-space)

[15] Lawrence A *et al* 2022 The case for space environmentalism *Nat. Astron.* **6** 428

[16] Euroconsult 2021 Satellites to be built and launched by 2030 *Market Research Report* (Euroconsult)

[17] Wertz J R, Everett D F and Puschell J J 2011 *Space Mission Engineering: The New SMAD* (Microcosm Press)

[18] Fortune Business Insights 2023 Xenon market size, share & industry analysis, by type (N3, N4.5, and N5), by application (imaging & lighting, satellite, electronics & semiconductors, medical, and others), and regional forecast, 2024–2032 *Market Report* FBI101965 (Fortune Business Insights)

[19] The Economist 2023 How rare-gas supply adapted to Russia's war (available at: www.economist.com/finance-and-economics/2023/03/30/how-rare-gas-supply-adapted-to-russias-war)

[20] Munro-O'Brien T F and Ryan C N 2023 Performance of a low power Hall effect thruster with several gaseous propellants *Acta Astronaut.* **206** 257

[21] Dressler R, Chiu Y-H and Levandier D 2000 Propellant alternatives for ion and Hall effect thrusters *Proc. 38th Aerospace Sciences Meeting & Exhibit* (AIAA) p AIAA-2000-0602

[22] Tverdokhlebov O and Semenkin A 2001 Iodine propellant for electric propulsion—to be or not to be *Proc. 37th Joint Propulsion Conf. & Exhibit* (AIAA) p AIAA-2001-3350

[23] Matsutani A, Ohtsuki H and Koyama F 2005 Iodine solid source inductively coupled plasma etching of InP *Jpn. J. Appl. Phys.* **44** L576

[24] Minnhagen L 1962 The energy levels of neutral atomic iodine *Ark. Fys.* **21** 415

[25] US Geological Survey 2024 Iodine, mineral commodity summaries (available at: https://pubs.usgs.gov/periodicals/mcs2024/mcs2024-iodine.pdf)

[26] Esteves B 2022 Investigation of iodine plasmas for space propulsion applications *PhD Thesis* Institut polytechnique de Paris

[27] Martínez J M, Rafalskyi D, Rossi E Z and Aanesland A 2020 Development, qualification and first flight data of the iodine based cold gas thruster for cubesats *Proc. 5th IAA Conf. on University Satellite Missions and CubeSat Workshop* (American Astronautical Society) p IAA-AAS-CU-20-XX-XX

[28] Lafleur T, Habl L, Rossi E Z and Rafalskyi D 2022 Development and validation of an iodine plasma model for gridded ion thrusters *Plasma Sources Sci. Technol.* **31** 114001

[29] Hamilton J R 2015 Consultancy project for LPP. I_2 and I^- data *Technical Report* (Quantemol)

[30] Hamilton J R 2017 Iodine: I_2^+ molecule and I atom *Technical Report* (Quantemol)

[31] Ambalampitiya H B, Hamilton K R, Zatsarinny O, Bartschat K, Turner M A P, Dzarasova A and Tennyson J 2021 Electron scattering cross-section calculations for atomic and molecular iodine *Atoms* **9** 103

[32] Lafleur T, Esteves B, Drag C, Bourdon A, Chabert P, Martinez Martinez J, Vialetto L, Bowden G and Shaik R 2025 Iodine plasmas for space propulsion and industrial applications (data) *Zenodo* (https://doi.org/10.5281/zenodo.17348832)

[33] Pavese F 2022 The triple point temperature of iodine *J. Chem. Thermodyn.* **165** 106639

[34] Washburn E W and West C J 1928 *International Critical Tables of Numerical Data, Physics, Chemistry and Technology* (National Research Council)

[35] Gillespie L J and Fraser L H 1936 The normal vapor pressure of crystalline iodine *J. Am. Chem. Soc.* **58** 2260

[36] Berkenblit M and Reisman A 1966 The vapor pressure of iodine in the temperature interval 43°–80°C *J. Electrochem. Soc.* **113** 93

[37] Lindenberg A 1971 System of thermodynamic equations for heat capacity and vapor pressure of solid and liquid iodine *C. R. Hebdomadaires Séances Acad. Sci. C* **273** 1017

[38] Cheng W-Y, Chen L, Yoon T H, Hall J L and Ye J 2002 Sub-doppler molecular-iodine transitions near the dissociation limit (523–498 nm) *Opt. Lett.* **27** 571

[39] Chen L 2005 High-precision spectroscopy of molecular iodine: from optical frequency standards to global descriptions of hyperfine interactions and associated electronic structure *PhD Thesis* University of Colorado

[40] Bureau International des Poids et Mesures 2023 *The International System of Units (SI)* (Bureau International des Poids et Mesures) (available at:www.bipm.org/en/publications/si-brochur)

[41] Sako T, Haraya K, Shindo Y, Obata K and Hakuta T 1979 Vapor pressure of liquid iodine *Kagaku Kogaku Ronbunshu* **5** 304

[42] Poling B E *et al* 2001 *The Properties of Gases and Liquids* vol 5 (Mcgraw-Hill)

[43] Poynting J 1881 V. Change of state: solid-liquid *London, Edinburgh Dublin Phil. Mag. J. Sci.* **12** 32

[44] Gerstenkorn S and Luc P 1978 *Atlas du Spectre d'Absorption de la Molecule d'Iode 14800-20000 cm^{-1}* (Editions du Centre National de la Recherche Scientifique (CNRS))

[45] D'alterio R, Mattson R and Harris R 1974 Potential curves for the I_2 molecule: an undergraduate physical chemistry experiment *J. Chem. Educ.* **51** 282

[46] Tellinghuisen J 1982 The D' → A' transition in I_2 *J. Mol. Spectrosc.* **94** 231

[47] Verma R D 1960 Ultraviolet resonance spectrum of the iodine molecule *J. Chem. Phys.* **32** 738

[48] Franck J and Dymond E G 1926 Elementary processes of photochemical reactions *Trans. Faraday Soc.* **21** 536

[49] Curtis W E and Evans S F 1933 The spectra of the halogen molecules. Part I. Iodine *Proc. R. Soc. A* **141** 603

[50] Tellinghuisen J 1973 Resolution of the visible-infrared absorption spectrum of I_2 into three contributing transitions *J. Chem. Phys.* **58** 2821

[51] Tellinghuisen J 1985 *The Franck-Condon Principle in Bound-Free Transitions (Advances in Chemical Physics)* (Wiley)

[52] Tellinghuisen J 1982 Transition strengths in the visible–infrared absorption spectrum of I_2 *J. Chem. Phys.* **76** 4736

[53] Tellinghuisen J 2011 Least-squares analysis of overlapped bound-free absorption spectra and predissociation data in diatomics: the $C(^1\Pi_u)$ state of I_2 *J. Chem. Phys.* **135** 054301

[54] Teichteil C and Pelissier M 1994 Relativistic calculations of excited states of molecular iodine *Chem. Phys.* **180** 1

[55] Williamson J 2007 Teaching the rovibronic spectroscopy of molecular iodine *J. Chem. Educ.* **84** 1355

[56] Schwarzer D, Schroeder J and Schröder C 2001 Quantum yields for the photodissociation of iodine in compressed liquids and supercritical fluids *Z. Phys. Chem.* **215** 183

[57] Saiz-Lopez A and Plane J M C 2004 Novel iodine chemistry in the marine boundary layer *Geophys. Res. Lett.* **31** L04112

[58] Ye J, Ma L S and Hall J L 2001 Molecular iodine clock *Phys. Rev. Lett.* **87** 270801

[59] Esteves B, Blondel C, Chabert P, Michel T and Drag C 2024 Measurement of the main neutral species densities and temperatures in iodine plasmas using optical absorption techniques *Plasma Sources Sci. Technol.* **33** 015004

[60] Burkholder J B *et al* 2020 Chemical kinetics and photochemical data for use in atmospheric studies *JPL Publication 19-5* (JPL NASA)

[61] Lukashov S, Petrov A and Pravilov A 2018 *The Iodine Molecule* (Springer)

[62] McNaught I J 1980 The electronic spectrum of iodine revisited *J. Chem. Educ.* **57** 101

[63] Herzberg G 2013 *Molecular Spectra and Molecular Structure* vol 1 (Read Books Limited)

[64] Gerjuoy E and Stein S 1955 Rotational excitation by slow electrons *Phys. Rev.* **97** 1671

[65] Vialetto L, Moussa A B, van Dijk J, Longo S, Diomede P, Guerra V and Alves L L 2021 Effect of anisotropic scattering for rotational collisions on electron transport parameters in CO *Plasma Sources Sci. Technol.* **30** 075001

[66] Vargaftik N B 2020 *Handbook of Thermal Conductivity of Liquids and Gases* (CRC Press)

[67] Rankine A O 1915 On the viscosity of the vapour of iodine *Proc. R. Soc. A* **91** 201

[68] Svehla R A 1963 *Estimated Viscosities and Thermal Conductivities of Gases at High Temperatures* (NASA)

[69] Polzin K A, Seixal J F, Mauro S L, Burt A O, Martinez A and Martin A K 2017 The iodine satellite (iSat) propellant feed system-design and development *Proc. 35th Int. Electric Propulsion Conf.* (Electric Rocket Propulsion Society) p IEPC-2017-11

[70] Ho C Y, Powell R W and Liley P E 1972 Thermal conductivity of the elements *J. Phys. Chem. Ref. Data* **1** 279

[71] Grondein P, Lafleur T, Chabert P and Aanesland A 2016 Global model of an iodine gridded plasma thruster *Phys. Plasmas* **23** 033514

[72] Stull D R 1965 *JANAF Thermochemical Tables* (Clearinghouse for Federal Scientific and Technical Information)

[73] Zehe M J, Gordon S and McBride B J 2002 CAP: a computer code for generating tabular thermodynamic functions from NASA Lewis coefficients *Technical Report* TP-2001-210959/REV1 (NASA)

[74] NASA Glenn Research Center 2023 Chemical equilibirum with applications (available at: https://cearun.grc.nasa.gov/ThermoBuild/)

[75] Lighthill M 1957 Dynamics of a dissociating gas. Part I. Equilibrium flow *J. Fluid Mech.* **2** 1

[76] Heller L 1959 Equilibrium statistical mechanics of dissociating diatomic gases *Phys. Fluids* **2** 147

[77] Holbrook R T and Kunc J A 1994 Impact of dissociation and ionization on properties of iodine vapor *Phys. Plasmas* **1** 1075

[78] Perlman M L and Rollefson G 1941 The vapor density of iodine at high temperatures *J. Chem. Phys.* **9** 362

[79] Baulch D L, Duxbury J, Grant S J and Montague D C 1981 *Evaluated Kinetic Data for High Temperature Reactions. Volume 4: Homogeneous Gas Phase Reactions of Halogen- and Cyanide-Containing Species* (*Journal of Physical and Chemical Reference Data* vol 10) (American Chemical Society and the American Institute of Physics for the National Bureau of Standards)

[80] Ip J and Burns G 1972 Recombination of iodine atoms by flash photolysis over a wide temperature range. II I_2 in He, Ar, Xe, N_2, CO *J. Chem. Phys.* **56** 3155

[81] Mohler F L 1925 Relative production of negative and positive ions by electron collisions *Phys. Rev.* **26** 614

[82] Hogness T R and Harkness R W 1928 The ionization processes of iodine interpreted by the mass-spectrograph *Phys. Rev.* **32** 784

[83] Frost D C and McDowell C A 1960 The ionization and dissociation of some halogen molecules by electron impact *Can. J. Chem.* **38** 407

[84] Healey R 1938 LXXX. The behaviour of electrons in iodine vapour *London, Edinburgh Dublin Phil. Mag. J. Sci.* **26** 940

[85] Buchdahl R 1941 Negative ion formation in iodine vapor by electron impacts *J. Chem. Phys.* **9** 146

[86] Biondi M A 1958 Dissociative attachment of electrons in iodine. I. Microwave determination of the absolute cross section at 300° K *Phys. Rev.* **109** 2005

[87] Fox R 1958 Dissociative attachment of electrons in iodine. II. Mass spectrographic determination of the energy dependence of the cross section *Phys. Rev.* **109** 2008

[88] Biondi M A and Fox R E 1958 Dissociative attachment of electrons in iodine. III. Discussion *Phys. Rev.* **109** 2012

[89] Truby F K 1968 Dissociative electron attachment in I_2 vapor at 295° K *Phys. Rev.* **172** 24

[90] Truby F 1969 Temperature Dependence of Electron Attachment in I_2 Vapor *Phys. Rev.* **188** 508

[91] Woolsey G A, Plumb I C and Lewis D B 1973 Langmuir probe characteristics in a positive-ion/negative-ion plasma *J. Phys. D: Appl. Phys.* **6** 1883

[92] Emeleus K G and Coulter J R M 1983 Notes on discharges in low-pressure iodine vapour *Int. J. Electron.* **54** 777

[93] National Institute of Standards and Technology 2021 *Atomic Spectra Database, NIST Standard Reference Database 78* (available at: https://physics.nist.gov/asd)

[94] Esteves B, Blondel C, Chabert P and Drag C 2023 Two-photon absorption laser induced fluorescence (TALIF) detection of atomic iodine in low-temperature plasmas and a revision of the energy levels of I I *J. Phys. B: At. Mol. Opt. Phys.* **56** 055002

[95] Wu J and Yuan J 2007 Fully relativistic *R*-matrix study of the interaction between a slow electron and atomic iodine: scattering and photodetachment *Phys. Rev. A* **76** 024702

[96] Zatsarinny O *et al* 2011 Electron-collision cross sections for iodine *Phys. Rev. A* **83** 042702

[97] Lucken R 2019 Theory and simulation of low-pressure plasma transport phenomena: application to the PEGASES Thruster *PhD Thesis* Université Paris-Saclay

[98] Marmuse F 2020 Iodine plasmas: experimental and numerical studies. Application to electric propulsion *PhD Thesis* Sorbonne Université

[99] Hayes T R, Wetzel R C and Freund R S 1987 Absolute electron-impact-ionization cross-section measurements of the halogen atoms *Phys. Rev. A* **35** 578

[100] Margreiter D, Deutsch H and Märk T 1994 A semiclassical approach to the calculation of electron impact ionization cross-sections of atoms: from hydrogen to uranium *Int. J. Mass Spectrom. Ion Process.* **139** 127

[101] Huo W M and Kim Y-K 2000 Use of relativistic effective core potentials in the calculation of total electron-impact ionization cross-sections *Chem. Phys. Lett.* **319** 576

[102] Joshipura K and Limbachiya C G 2002 Theoretical total ionization cross-sections for electron impact on atomic and molecular halogens *Int. J. Mass Spectrom.* **216** 239

[103] Bartlett P L and Stelbovics A T 2004 Electron-impact ionization cross sections for elements Z = 1 to Z = 54 *At. Data Nucl. Data Tables* **86** 235

[104] Kim Y-K and Rudd M E 1994 Binary-encounter-dipole model for electron-impact ionization *Phys. Rev. A* **50** 3954

[105] Ali M A and Kim Y-K 2008 Ionization cross sections by electron impact on halogen atoms, diatomic halogen and hydrogen halide molecules *J. Phys. B: At. Mol. Opt. Phys.* **41** 145202

[106] Vinodkumar M, Dave R, Bhutadia H and Antony B K 2010 Electron impact total ionization cross sections for halogens and their hydrides *Int. J. Mass Spectrom.* **292** 7

[107] Naghma R, Mahato B N, Vinodkumar M and Antony B K 2011 Electron impact total ionization cross sections for atoms with Z = 49–54 *J. Phys. B: At. Mol. Opt. Phys.* **44** 105204

[108] Levko D and Raja L L 2021 Fluid modeling of inductively coupled iodine plasma for electric propulsion conditions *J. Appl. Phys.* **130** 173302

[109] Dietz P, Becker F, Keil K, Holste K and Klar P J 2020 Performance of a rf neutralizer operating with noble gases and iodine *Eur. Phys. J. Appl. Phys.* **91** 10901

[110] Zatsarinny O and Bartschat K 2013 The B-spline R-matrix method for atomic processes: application to atomic structure, electron collisions and photoionization *J. Phys. B: At. Mol. Opt. Phys.* **46** 112001

[111] Carr J M, Galiatsatos P, Gorfinkiel J D, Harvey A G, Lysaght M, Madden D, Mašín Z, Plummer M, Tennyson J and Varambhia H 2012 UKRmol: a low-energy electron-and positron-molecule scattering suite *Eur. Phys. J. D* **66** 1

[112] Mašín Z, Benda J, Gorfinkiel J D, Harvey A G and Tennyson J 2020 UKRmol+: a suite for modelling electronic processes in molecules interacting with electrons, positrons and photons using the R-matrix method *Comput. Phys. Commun.* **249** 107092

[113] Tennyson J, Brown D B, Munro J J, Rozum I, Varambhia H N and Vinci N 2007 Quantemol-N: an expert system for performing electron molecule collision calculations using the R-matrix method *J. Phys.: Conf. Ser.* **86** 012001

[114] Cooper B *et al* 2019 Quantemol electron collisions (QEC): an enhanced expert system for performing electron molecule collision calculations using the R-matrix method *Atoms* **7** 97

[115] Agrawal A, Gupta S, Sharma L and Srivastava R 2024 Theoretical investigation of iodine plasma through detailed electron impact excitation cross-section calculations and collisional-radiative model analysis *Plasma Sources Sci. Technol.* **33** 115010

[116] Gupta S, Sharma L and Srivastava R 2018 Electron-impact excitation of Xe^+ and polarization of its subsequent emissions *J. Quant. Spectrosc. Radiat. Transfer* **219** 7

[117] Madison D H, Bartschat K and Srivastava R 1991 Distorted-wave calculation of elastic and inelastic scattering of electrons from cadmium *J. Phys. B: At. Mol. Opt. Phys.* **24** 1839

[118] Tallents G 2018 *An Introduction to the Atomic and Radiation Physics of Plasmas* (Cambridge University Press)

[119] Yadav H, Vinodkumar M, Limbachiya C, Vinodkumar P C and Mason N J 2020 Low energy electron interactions with iodine molecule (I_2) *J. Quant. Spectrosc. Radiat. Transfer* **250** 107035

[120] Tennyson J 2010 Electron–molecule collision calculations using the R-matrix method *Phys. Rep.* **491** 29

[121] Cockett M C R, Donovan R J and Lawley K P 1996 Zero kinetic energy pulsed field ionization (ZEKE − PFI) spectroscopy of electronically and vibrationally excited states of I_2^+: the $A^2\Pi_{3/2,u}$ state and a new electronic state, the $a^4\Sigma_u^-$ state *J. Chem. Phys.* **105** 3347

[122] Deutsch H, Becker K and Märk T 2000 Calculation of absolute electron-impact ionization cross-sections of dimers and trimers *Eur. Phys. J. D* **12** 283

[123] Probst M, Deutsch H, Becker K and Märkde T 2001 Calculations of absolute electron-impact ionization cross sections for molecules of technological relevance using the DM formalism *Int. J. Mass Spectrom.* **206** 13

[124] Lieberman M A and Lichtenberg A J 2005 *Principles of Plasma Discharges and Materials Processing* (Wiley)

[125] Tam W and Wong S F 1978 Dissociative attachment of halogen molecules by 0–8 eV electrons *J. Chem. Phys.* **68** 5626

[126] Brooks H L, Hunter S R and Nygaard K J 1979 Temperature dependence of the electron attachment coefficient in iodine *J. Chem. Phys.* **71** 1870

[127] Kurepa M, Babić D and Belić D 1981 Attachment rate coefficients of halogen molecules (F_2, Cl_2, Br_2, I_2) for mean electron energies 10^{-2} to 10^2 eV *Chem. Phys.* **59** 125

[128] Pozdneev S 2000 Electron scattering on excited diatomic molecules in selected rovibrational states *J. Russ. Laser Res.* **21** 182

[129] Shipsey E J 1970 Thermal-energy dissociative attachment of I_2; deduction of the curve crossing point from experimental measurements *J. Chem. Phys.* **52** 2274

[130] Birtwistle D and Modinos A 1978 Dissociative attachment in iodine *J. Phys. B: At. Mol. Phys.* **11** 2949

[131] Ayala J, Wentworth W and Chen E 1981 Electron attachment to halogens *J. Phys. Chem.* **85** 768

[132] Gallagher J, Beaty E, Dutton J and Pitchford L 1983 An annotated compilation and appraisal of electron swarm data in electronegative gases *J. Phys. Chem. Ref. Data* **12** 109

[133] Caledonia G 1975 Survey of the gas-phase negative ion kinetics of inorganic molecules. Electron attachment reactions *Chem. Rev.* **75** 333

[134] Rosenstock H M, Draxl K, Steiner B W and Herron J-T 1977 *Energetics of Gaseous Ions* (American Chemical Society and the American Institute of Physics for the National Bureau of Standards)

[135] Peláez R J, Blondel C, Delsart C and Drag C 2009 Pulsed photodetachment microscopy and the electron affinity of iodine *J. Phys. B: At. Mol. Opt. Phys.* **42** 125001

[136] Mathur D and Badrinathan C 1987 A new channel for observing giant resonances: dissociative ionization of molecular iodine by electrons *Phys. Lett. A* **123** 345

[137] Poline M *et al* 2022 Final-state-resolved mutual neutralization in I^+-I^- collisions *Phys. Rev. A* **106** 012812

[138] Mulliken R S 1971 Iodine revisited *J. Chem. Phys.* **55** 288

[139] Prince B D, Levandier D J and Bemish R J 2017) Application of a first generation collisional radiative model for iodine to optical emissions from the plume of an iodine Hall effect thruster *Proc. 53rd AIAA/SAE/ASEE Joint Propulsion Conf.* (AIAA) p AIAA-2017-4634

[140] Prince B D, Levandier D J and Bemish R J 2020 Photoemission resulting from collisions of I_2 with 5–100 eV electrons *J. Phys. B: At. Mol. Opt. Phys.* **53** 215201

[141] Huber K 2013 *Molecular Spectra and Molecular Structure: IV. Constants of Diatomic Molecules* (Springer)

[142] Thompson D L 1974 Monte carlo classical dynamical study of the Cl + Cl_2 and I + I_2 systems: vibrational relaxation and atom-exchange reactions *J. Chem. Phys.* **60** 4557

[143] Millikan R C and White D R 1963 Systematics of vibrational relaxation *J. Chem. Phys.* **39** 3209

[144] Phelps A V 1994 The application of scattering cross sections to ion flux models in discharge sheaths *J. Appl. Phys.* **76** 747

[145] Smirnov B 2003 *Physics of Atoms and Ions* (Springer)

[146] Hause M L, Prince B D and Bemish R J 2015 A guided-ion beam study of the collisions and reactions of I^+ and I_2^+ with I_2 *J. Chem. Phys.* **142** 074301

[147] Sakabe S and Izawa Y 1992 Simple formula for the cross sections of resonant charge transfer between atoms and their positive ions at low impact velocity *Phys. Rev. A* **45** 2086

[148] Choi M 2016 Modeling an iodine Hall thruster plume in the iodine satellite (ISAT) *Proc. Liquid Propulsion (LPS) Meeting* (NASA Glenn Research Center) GRC-E-DAA-TN37710

[149] Huang S and Gudmundsson J T 2013 A particle-in-cell/Monte Carlo simulation of a capacitively coupled chlorine discharge *Plasma Sources Sci. Technol.* **22** 055020

[150] Thorsteinsson E and Gudmundsson J T 2009 A global (volume averaged) model of a chlorine discharge *Plasma Sources Sci. Technol.* **19** 015001

[151] Gudmundsson J T, Kawamura E and Lieberman M A 2013 A benchmark study of a capacitively coupled oxygen discharge of the oopd1 particle-in-cell Monte Carlo code *Plasma Sources Sci. Technol.* **22** 035011

[152] Karmohapatro S B 1965 Charge exchange of Cl^- ions with atomic chlorine *J. Phys. Soc. Japan* **20** 839

[153] Szabo J, Pote B, Paintal S, Robin M, Hillier A, Branam R D and Huffmann R E 2012 Performance evaluation of an iodine-vapor Hall thruster *J. Propuls. Power* **28** 848

[154] Yeung T H Y 1958 Recombination coefficients for positive and negative ions *Proc. Phys. Soc.* **71** 341

[155] Greaves C 1964 Ion-ion recombination in iodine afterglows *J. Electron. Control* **17** 171

[156] Spencer-Smith J 1935 LXXXIII. Negative ions of iodine. Part II. Ion beams *London, Edinburgh Dublin Phil. Mag. J. Sci.* **19** 1016

[157] Smirnov B M 2008 *Physics of Ionized Gases* (Wiley)

[158] Fritioff K, Sandström J, Hanstorp D, Ehlerding A, Larsson M, Collins G, Pegg D, Danared H, Källberg A and Le Padellec A 2003 Electron-impact detachment from Cl^- *Phys. Rev. A* **68** 012712

[159] Benilov M 1996 Multifluid equations of a plasma with various species of positive ions and the Bohm criterion *J. Phys. D: Appl. Phys.* **29** 364

[160] Benilov M S 1997 A kinetic derivation of multifluid equations for multispecies nonequilibrium mixtures of reacting gases *Phys. Plasmas* **4** 521

[161] Brewer L and Tellinghuisen J B 1971 Detection of iodine atoms by an atomic fluorescence technique: application to study of diffusion and wall recombination *J. Chem. Phys.* **54** 5133

[162] Raimbault J-L, Blondel C, Esteves B and Drag C 2025 Space-time dependence of the atomic density produced by laser photodissociation in a confined molecular gas: application to iodine *J. Appl. Phys.* submitted

[163] Chichinin A 2006 Chemical properties of electronically excited halogen atoms $X(^2P_{1/2})$ (X = F, Cl, Br, I) *J. Phys. Chem. Ref. Data* **35** 869

[164] Deakin J J and Husain D 1972 Temperature dependence of collisionally induced spin orbit relaxation of electronically excited iodine atoms, $I(5^2P_{1/2})$ *J. Chem. Soc., Faraday Trans. 2* **68** 1603

[165] Kartazaev V A, Penkin N P and Tolmachev Y A 1977 Determination of the temperature dependence of the rate constant representing quenching of metastable iodine atoms by iodine molecules *Sov. J. Quantum Electron.* **7** 608

[166] Cline J I and Leone S R 1991 Temperature dependence of the quenching of $I^*(^2P_{3/2})$ by iodine from 300 to 800 K *J. Phys. Chem.* **95** 2917

[167] Burde D, Yang T and McFarlane R 1993 Temperature dependence of the collisional deactivation of $I(^2P_{1/2})$ by I_2 and O_2 from 300 to 600 K *Chem. Phys. Lett.* **205** 69

[168] Hall G, Marinelli W and Houston P 1983 Electronic-to-vibrational energy transfer from $I(5^2P_{1/2})$ to I_2 $(25 < v < 43)$ *J. Phys. Chem.* **87** 2153

[169] Bailey V and Healey R 1935 LVII. The behaviour of electrons in chlorine *London, Edinburgh Dublin Phil. Mag. J. Sci.* **19** 725

[170] Bailey J, Makinson R and Somerville J 1937 XIV. The behaviour of electrons in bromine *London, Edinburgh Dublin Phil. Mag. J. Sci.* **24** 177

[171] González-Magaña O and De Urquijo J 2018 Measurement of electron swarm coefficients in chlorine and its mixtures with nitrogen *Plasma Sources Sci. Technol.* **27** 06LT02

[172] Martínez J M and Lafleur T 2023 On the selection of propellants for cold/warm gas propulsion systems *Acta Astronaut.* **212** 54

[173] Jerman G A 2022 Iodine vapor exposure testing of engineering materials *Technical Report* TM-20220015272 (NASA)

[174] Martínez Martínez J and Rafalskyi D 2022 Design and development of iodine flow control systems for miniaturized propulsion systems *CEAS Space J.* **14** 91

[175] Craig B D and Anderson D B 1965 *Handbook of Corrosion Data* (ASM International)

[176] Zschätzsch D, Benz S L, Holste K, Vaupel M, Hey F G, Kern C, Janek J and Klar P J 2022 Corrosion of metal parts on satellites by iodine exposure in space *J. Electr. Propuls.* **1** 14

[177] Beck C L, Riley B J, Chong S, Karkamkar A, Seiner D R and Clark S B 2021 Molecular iodine interactions with metal substrates: towards the understanding of iodine interactions in the environment following a nuclear accident *J. Nucl. Mater.* **546** 152771

[178] Winston Revie R 2011 *Uhlig's Corrosion Handbook* (Wiley)

[179] Farina S B, Duffo G and Galvele J R 2002 Stress corrosion cracking of zirconium and zircaloy-4 in iodine containing solution *Proc. CORROSION 2002* (NACE International) p C2002–02436

[180] Fontana M G and Staehle R W 1976 *Advances in Corrosion Science and Technology* vol 5 (Plenum Press)

[181] Guidi C, Becatti G, Bernazzani L, Ceccarini A, Paganucci F and Saravia M M 2024 Study on the compatibility between iodine and common aerospace materials *Acta Astronaut.* **220** 392

[182] Lai G Y 2007 *High Temperature Corrosion and Materials Applications* (ASM International)

[183] Thompson S J, VanGermert J J, Farnell C C, Farnell C C, Farnell S C, Hensen T J, Ham R, Williams D D, Chandler J P and Williams J D 2019 Development of an iodine compatible hollow cathode *Proc. AIAA Propulsion and Energy 2019 Forum* (AIAA) p AIAA-2019-3997

[184] Mathieu B 1990 Un exemple de transition d'un processus de corrosion en phase gazeuse vers une corrosion en milieu aqueux: cas de l'acier inoxydable Z2CN18-10 par l'iode et l'eau en phase vapeur *PhD Thesis* Université de Dijon

[185] Beck C L, Riley B J, Chong S, Smith N, Seiner D R, Seiner B N, Engelhard M H and Clark S B 2021 Molecular iodine interactions with Fe, Ni, Cr and stainless steel alloys *Ind. Eng. Chem. Res.* **60** 2447

[186] Costa G, Benavides G, Kulis M and Setlock J 2020 Corrosion behavior of stainless steel 304 and nickel 625 under iodine vapor at 300 °C *Technical Report* TM-20205001422 (NASA)

[187] Holste K *et al* 2020 Ion thrusters for electric propulsion: scientific issues developing a niche technology into a game changer *Rev. Sci. Instrum.* **91** 061101

[188] Wassermann E, Falconer W and Yager W 1968 Photodissociation of molecular iodine *Ber. Bunsenges. Phys. Chem.* **72** 248

[189] Katsoprinakis G, Chatzidrosos G, Kypriotakis J, Stratakis E and Rakitzis T 2016 High steady-state column density of I(^{2}P$_{3/2}$) atoms from I$_2$ photodissociation at 532 nm: towards parity non-conservation measurements *Sci. Rep.* **6** 33261

[190] Lafleur T, Schulze J and Donkó Z 2019 Plasma-surface interactions *Plasma Sources Sci. Technol.* **28** 040201

[191] Radmilović-Radjenović M and Radjenović B 2007 A particle-in-cell simulation of the breakdown mechanism in microdischarges with an improved secondary emission model *Contrib. Plasma Phys.* **47** 165

[192] Donkó Z 2001 Apparent secondary-electron emission coefficient and the voltage-current characteristics of argon glow discharges *Phys. Rev. E* **64** 026401

[193] Kaganovich I, Raitses Y, Sydorenko D and Smolyakov A 2007 Kinetic effects in a Hall thruster discharge *Phys. Plasmas* **14** 057104

[194] Lafleur T, Chabert P and Booth J-P 2013 Secondary electron induced asymmetry in capacitively coupled plasmas *J. Phys. D: Appl. Phys.* **46** 135201

[195] Wen Y-Y, Zhang Y-R, Jiang G, Song Y-H and Wang Y-N 2019 Secondary electron effect on sustaining capacitively coupled discharges: a hybrid modeling investigation of the ionization rate *AIP Adv.* **9** 055019

[196] Habl L, Rafalskyi D and Lafleur T 2020 Ion beam diagnostic for the assessment of miniaturized electric propulsion systems *Rev. Sci. Instrum.* **91** 093501

[197] Hershkowitz N 1989 How Langmuir probes work *Plasma Diagnostics: Discharge Parameters and Chemistry* (Academic)

[198] Lobbia R B and Beal B E 2017 Recommended practice for use of langmuir probes in electric propulsion testing *J. Propuls. Power* **33** 566

[199] Habl L, Rafalskyi D and Lafleur T 2021 Secondary electron emission due to multi-species iodine ion bombardment of different target materials *J. Appl. Phys.* **129** 153302

[200] Corbella C, Marcak A, de los Arcos T and von Keudell A 2016 Revising secondary electron yields of ion-sputtered metal oxides *J. Phys. D: Appl. Phys.* **49** 16LT01

[201] Depla D, Li X, Mahieu S and De Gryse R 2008 Determination of the effective electron emission yields of compound materials *J. Phys. D: Appl. Phys.* **41** 202003

[202] Lewis M A, Glocker D A and Jorne J 1989 Measurements of secondary electron emission in reactive sputtering of aluminum and titanium nitride *J. Vac. Sci. Technol. A* **7** 1019

[203] Yamauchi Y and Shimizu R 1983 Secondary electron emission from aluminum by argon and oxygen ion bombardment below 3 keV *Jpn. J. Appl. Phys.* **22** L227

[204] Raizer Y P 1991 *Gas Discharge Physics* (Springer)

[205] Daksha M, Derzsi A, Mujahid Z, Schulenberg D, Berger B, Donkó Z and Schulze J 2019 Material dependent modeling of secondary electron emission coefficients and its effects on PIC/MCC simulation results of capacitive RF plasmas *Plasma Sources Sci. Technol.* **28** 034002

[206] Yamamura Y and Tawara H 1996 Energy dependence of ion-induced sputtering yields from monatomic solids at normal incidence *At. Data Nucl. Data Tables* **62** 149

[207] Eckstein W 2008 Sputtering yields *Vacuum* **82** 930

[208] Sigmund P 1969 Theory of sputtering. I. Sputtering yield of amorphous and polycrystalline targets *Phys. Rev.* **184** 383

[209] Yamamura Y and Shindo S 1984 An empirical formula for angular dependence of sputtering yields *Radiat. Eff.* **80** 57

[210] Küstner M, Eckstein W, Dose V and Roth J 1998 The influence of surface roughness on the angular dependence of the sputter yield *Nucl. Instrum. Methods Phys. Res. B* **145** 320

[211] Doerner R P, Whyte D G and Goebel D M 2003 Sputtering yield measurements during low energy xenon plasma bombardment *J. Appl. Phys.* **93** 5816

[212] Tartz M, Heyn T, Bundesmann C, Zimmermann C and Neumann H 2011 Sputter yields of Mo, Ti, W, Al, Ag under xenon ion incidence *Eur. Phys. J. D* **61** 587

[213] Williams J D, Gardner M M, Johnson M L and Wilbur P J 2003 Xenon sputter yield measurements for ion thruster materials *Proc. 28th Int. Electric Propulsion Conf.* (Electric Rocket Propulsion Society) p IEPC-2003-130

[214] Yim J T 2017 A survey of xenon ion sputter yield data and fits relevant to electric propulsion spacecraft integration *Proc. 35th Int. Electric Propulsion Conf.* (Electric Rocket Propulsion Society) p IEPC-2017-060

[215] Eckstein W and Preuss R 2003 New fit formulae for the sputtering yield *J. Nucl. Mater.* **320** 209

[216] Kino H, Ikuse K, Dam H-C and Hamaguchi S 2021 Characterization of descriptors in machine learning for data-based sputtering yield prediction *Phys. Plasmas* **28** 013504

[217] Rafalskyi D, Rossi E Z, Coral G, Habl L, Jain P, Bore A, Dudin S, Lafleur T and Dudin D 2024 Lifetime testing campaign of an iodine-fed electric propulsion system *Proc. Space Propulsion 2024* (3AF) p S2024-38

[218] Gilleo M and Kash S 1961 Propulsion by composite beams of negative and positive ions *ARS J.* **31** 621

[219] Bussi G and Filippi F 1963 *Propulsion Electrostatique Par Ions Postifs et Negatifs* vol 26 (Institute di Machine E. Motori per Aeromobile, Turin, Pubblicazione)

[220] Dong W, Kilpatrick W, Teem J and Zuccaro D 1962 Negative iodine formation on metal hexaboride surfaces *Proc. ARS Electric Propulsion Conf.* (AIAA) p ARS aer-2441-62

[221] Gamero-Castano M and Hruby V 2001 Electrospray as a source of nanoparticles for efficient colloid thrusters *J. Propuls. Power* **17** 977

[222] Keidar M 2016 Micro-cathode arc thruster for small satellite propulsion *Proc. 2016 IEEE Aerospace Conf.* (IEEE)

[223] Dressler R A, Levandier D J and Chiu Y-H 2003 Iodine electric propulsion thrusters *US Patent No.* US6609363B1

[224] Chabert P 2006 Electronegative plasma motor *US Patent No.* US9603232b2

[225] Szabo J, Pote B, Paintal S, Robin M, Kolencik G, Hillier A, Branam R and Huffman R 2011 Performance evaluation of an iodine vapor Hall thruster *Proc. 47th AIAA/ASME/SAE/ASEE Joint Propulsion Conf. & Exhibit* (AIAA) p AIAA-2011-5891

[226] Szabo J and Robin M 2014 Plasma species measurements in the plume of an iodine fueled Hall thruster *J. Propuls. Power* **30** 1357

[227] Chiu Y-H and Prince B 2012 Optical emission spectra of the iodine Hall thruster *Proc. 48th AIAA/ASME/SAE/ASEE Joint Propulsion Conf. & Exhibit* (AIAA) p AIAA-2012-3872

[228] Szabo J, Robin M, Paintal S, Pote B, Hruby V and Freeman C 2014 Iodine plasma propulsion test results at 1-10 kW *IEEE Trans. Plasma Sci.* **43** 141

[229] Szabo J, Robin M, Paintal S, Pote B, Hruby V and Freeman C 2013 Iodine propellant space propulsion *Proc. 33rd Int. Electric Propulsion Conf.* (Electric Rocket Propulsion Society) p IEPC-2013-311

[230] Dankanich J, Szabo J J, Pote B, Oleson S R and Kamhawi H 2014 Mission and system advantages of iodine Hall thrusters *Proc. 50th AIAA/ASME/SAE/ASEE Joint Propulsion Conf.* (AIAA) p AIAA-2014-3905

[231] Kamhawi H *et al* 2016 Overview of iodine propellant Hall thruster development activities at NASA Glenn Research Center *Proc. 52nd AIAA/SAE/ASEE Joint Propulsion Conf.* (AIAA) p AIAA-2016-4729

[232] Dankanich J, Polzin K A and Kamhawi H 2014 Iodine Hall thruster demonstration mission concept and development *Proc. 50th AIAA/ASME/SAE/ASEE Joint Propulsion Conf.* (AIAA) p AIAA-2014-3910

[233] Tsay M, Frongillo J, Zwahlen J and Paritsky L 2016 Maturation of iodine fueled BIT-3 RF ion thruster and RF neutralizer *Proc. 52nd AIAA/SAE/ASEE Joint Propulsion Conf.* (AIAA) p AIAA-2016-4544

[234] Holste K *et al* 2018 Performance of an iodine-fueled radio-frequency ion-thruster *Eur. Phys. J. D* **72** 9

[235] Aanesland A, Meige A and Chabert P 2009 Electric propulsion using ion-ion plasmas *J. Phys.: Conf. Ser.* **162** 012009

[236] Aanesland A, Popelier L, Leray G, Chabert P, Mazouffre S and Gerst D 2009 Plasma propulsion with electronegative gases *Proc. 31st Int. Electric Propulsion Conf.* (Electric Rocket Propulsion Society) p IEPC-2009-001

[237] Lafleur T, Rafalskyi D and Aanesland A 2014 Alternate extraction and acceleration of positive and negative ions from a gridded plasma source *Plasma Sources Sci. Technol.* **24** 015005

[238] Aanesland A, Rafalskyi D, Bredin J, Grondein P, Oudini N, Chabert P, Levko D, Garrigues L and Hagelaar G 2014 The PEGASES gridded ion-ion thruster performance and predictions *IEEE Trans. Plasma Sci.* **43** 321

[239] Yang J, Jia S, Zhang Z, Zhang X, Jin T, Li L, Cai Y and Cai J 2020 Performance of a 4 cm iodine-fueled radio frequency ion thruster *Plasma Sci. Technol.* **22** 094006

[240] Bellomo N *et al* 2022 Design and in-orbit demonstration of REGULUS, an iodine electric propulsion system *CEAS Space J.* **14** 79

[241] Vinci A E, Bianchi F M and Rafalskyi D 2024 Modeling and experimental results of low-power iodine-fed Hall thruster propulsion system *Proc. 38th Int. Electric Propulsion Conf.* (Electric Rocket Propulsion Society) p IEPC-2024-121

[242] Xu Z, Wang P, Cai D, Tan R and Jiang W 2024 Numerical and experimental research on the performance of an iodine-fed Hall thruster *Vacuum* **222** 113082

[243] Paganucci F, Saravia M M, Vinci A, Bernazzani L, Ceccarini A, Pellegrini G, Andressui T, Ducci C, Pedrini D and Kutfuß N 2019 I2HET: development of an iodine-fed Hall effect thruster *Proc. 36th Int. Electric Propulsion Conf.* (Electric Rocket Propulsion Society) p IEPC-2019-660

[244] Esteves B *et al* 2024 Iodine (I_2) and noble gases (Xe, Kr, Ar) plasma physics for HETs with preliminary characterisation of the PPS®X00 running on these alternative propellants *Proc. 38th Int. Electric Propulsion Conf.* (Electric Rocket Propulsion Society) p IEPC-2024-559

[245] Tirila V-G, Demairé A and Ryan C N 2023 Review of alternative propellants in Hall thrusters *Acta Astronaut.* **212** 284

[246] Hey F *et al* 2022 Overview of the European iodine Fed Cusp Field Thruster Research and Innovation Action-iFACT *Proc. 37th Int. Electric Propulsion Conf.* (Electric Rocket Propulsion Society) p IEPC-2022-530

[247] Busek 2025 RF ion thrusters (available at: www.busek.com/rf-ion-thrusters)

[248] ThrustMe 2025 The NPT30-I2 (available at: www.thrustme.fr/products/npt30-i2)

[249] Busek 2025 Hall thrusters (available at: www.busek.com/hall-thrusters)

[250] ThrustMe 2025 JPT150 (available at: www.thrustme.fr/products/jpt150)

[251] T4i 2025 REGULUS-50-I2 (available at: www.t4innovation.com/regulus-50-electric-propulsion-system/)

[252] Ponti F *et al* 2025 Advancing iodine thruster technology: insights and objectives of project BOOST *J. Electr. Propuls.* **4** 41

[253] Cybulski R, Shellhammer D, Lovell R, Domino E, Kotnik J, Cybulski J and Loveli R 1965 Results from SERT I ion rocket flight test *Proc. 4th Symp. on Advanced Propulsion Concepts* (Gordon and Breach Science Publishers) p 21

[254] Scholze F, Tartz M and Neumann H 2008 Inductive coupled radio frequency plasma bridge neutralizer *Rev. Sci. Instrum.* **79** 02B724

[255] Morishita T, Tsukizaki R, Yamamoto N, Kinefuchi K and Nishiyama K 2020 Application of a microwave cathode to a 200-W Hall thruster with comparison to a hollow cathode *Acta Astronaut.* **176** 413

[256] Motoki T, Takasaki D, Koizumi H, Ataka Y, Komurasaki K and Takao Y 2022 Experimental study on the performance characteristics of a miniature microwave discharge cathode *Acta Astronaut.* **196** 231

[257] Becke P S, Kottke N G, Vaupel M, Kutufa N, Tajmar M and Hey F G 2024 Review on the current state of iodine compatible neutralizers *J. Electr. Propuls.* **3** 1

[258] Frank W and Chabert T 1993 Dry etching of single-crystal silicon trench in hydrogen iodide containing plasmas: I. Pure *J. Electrochem. Soc.* **140** 490

[259] Kim H-M, Cha B-C and Kim D-W 2023 Simultaneous introduction of iodine and Fe-Nx into carbon nanospheres for enhanced catalytic activity towards oxygen reduction using a solution plasma process *Electrochem. Commun.* **156** 107589

[260] Gillam T, Goh C, Ninan N, Bilimoria K, Shirazi H, Saboohi S, Al-Bataineh S, Whittle J and Blencowe A 2021 Iodine complexed poly (vinyl pyrrolidone) plasma polymers as broad-spectrum antiseptic coatings *Appl. Surf. Sci.* **537** 147866

[261] Krása J *et al* 1998 Multiply charged ions from iodine laser-produced plasma of medium-and high-Z targets *Laser Part. Beams* **16** 5

[262] Jirasek V, Schmiedberger J, Čenský M and Kodymova J 2012 Dissociation of molecular iodine in RF discharge for oxygen-iodine lasers *Eur. Phys. J. D* **66** 1

[263] Kochetov I, Napartovich A, Vagin N and Yuryshev N 2009 Mechanism of pulse discharge production of iodine atoms from CF_3I molecules for a chemical oxygen-iodine laser *J. Phys. D: Appl. Phys.* **42** 055201

[264] Shuaibov A, Grabovaya I, Gomoki Z, Kalyuzhnaya A and Shchedrin A 2009 Output characteristics and parameters of the plasma from a gas-discharge low-pressure ultraviolet source using helium-iodine and xenon-iodine mixtures *Tech. Phys.* **54** 1819

[265] Matsutani A, Ohtsuki H and Koyama F 2006 Solid source dry etching process for GaAs and InP *Jpn. J. Appl. Phys.* **45** 8374

[266] Ohori D, Ishihara T, Wang X, Endo K, Hsieh T-H, Li Y, Natori N, Matsui K and Samukawa S 2023 Hydrogen iodide (HI) neutral beam etching characteristics of InGaN and GaN for micro-LED fabrication *Nanotechnology* **34** 365302

[267] Pearton S, Chakrabarti U, Hobson W, Abernathy C, Katz A, Ren F, Fullowan T and Perley A 1992 Hydrogen iodide-based dry etching of GaAs, InP and related compounds *J. Electrochem. Soc.* **139** 1763

[268] Fujita M, Sugitatsu A, Uesugi T and Noda S 2004 Fabrication of indium phosphide compound photonic crystal by hydrogen iodide/xenon inductively coupled plasma etching *Jpn. J. Appl. Phys.* **43** L1400

[269] Matsutani A, Ohtsuki H and Koyama F 2011 Inductively coupled plasma etching of silicon using solid iodine as an etching gas source *Jpn. J. Appl. Phys.* **50** 06GG07

[270] Lim W, Stafford L, Song J-I, Park J-S, Heo Y, Lee J-H, Kim J-J and Pearton S 2007 Dry etching of zinc-oxide and indium-zinc-oxide in IBr and BI_3 plasma chemistries *Appl. Surf. Sci.* **253** 3773
[271] Wang J, Cho H, Childress J, Pearton S, Sharifi F, Dahmen K and Gillman E 1999 Iodine-and bromine-based dry etching of $LaCaMnO_3$ *Plasma Chem. Plasma Process.* **19** 229
[272] Hong J *et al* 1999 Plasma chemistries for high density plasma etching of sic *J. Electron. Mater.* **28** 196
[273] Karecki S, Pruette L and Reif R 1998 Plasma etching of dielectric films with novel iodofluorocarbon chemistries: iodotrifluoroethylene and 1-iodoheptafluoropropane *J. Vac. Sci. Technol. A* **16** 755
[274] Kim S Y, Park I-S and Ahn J 2022 Atomic layer etching of SiO_2 using trifluoroiodomethane *Appl. Surf. Sci.* **589** 153045
[275] Park J-S, Park I-S, Kim S Y, Lee T, Ahn J, Shim T-H and Park J-G 2019 Plasma etching of SiO_2 with CF_3I gas in plasma-enhanced chemical vapor deposition chamber for in-situ cleaning *Sci. Adv. Mater.* **11** 1667
[276] Adamovich I *et al* 2017 The 2017 plasma roadmap: low temperature plasma science and technology *J. Phys. D: Appl. Phys.* **50** 323001
[277] Kanarik K J, Lill T, Hudson E A, Sriraman S, Tan S, Marks J, Vahedi V and Gottscho R A 2015 Overview of atomic layer etching in the semiconductor industry *J. Vac. Sci. Technol. A* **33** 020802
[278] Schrauwen J, Van Thourhout D and Baets R 2007 Iodine enhanced focused-ion-beam etching of silicon for photonic applications *J. Appl. Phys.* **102** 103104
[279] Schrauwen J, Van Thourhout D and Baets R 2006 Focused-ion-beam fabricated vertical fiber couplers on silicon-on-insulator waveguides *Appl. Phys. Lett.* **89** 141102
[280] Lota G *et al* 2016 The modified activated carbon treated with a low-temperature iodine plasma used as electrode material for electrochemical capacitors *Mater. Lett.* **175** 96
[281] He L, Zhou D, Lin Y, Ge R, Hou X, Sun X and Zheng C 2018 Ultrarapid in situ synthesis of Cu_2S nanosheet arrays on copper foam with room-temperature-active iodine plasma for efficient and cost-effective oxygen evolution *ACS Catal.* **8** 3859
[282] Mesko M F, Mello P A, Bizzi C A, Dressler V L, Knapp G and Flores E M 2010 Iodine determination in food by inductively coupled plasma mass spectrometry after digestion by microwave-induced combustion *Anal. Bioanal. Chem.* **398** 1125
[283] Oliveira A A, Trevizan L C and Nobrega J A 2010 Iodine determination by inductively coupled plasma spectrometry *Appl. Spectrosc. Rev.* **45** 447
[284] Julshamn K, Dahl L and Eckhoff K 2001 Determination of iodine in seafood by inductively coupled plasma/mass spectrometry *J. AOAC Int.* **84** 1976
[285] Mochalov L, Logunov A, Kitnis A, Prokhorov I, Kovalev A, Yunin P, Gogova D and Vorotyntsev V 2020 Plasma-chemical purification of iodine *Sep. Purif. Technol.* **238** 116446
[286] Esteves B, Marmuse F, Drag C, Bourdon A, Laguna A A and Chabert P 2022 Charged-particles measurements in low-pressure iodine plasmas used for electric propulsion *Plasma Sources Sci. Technol.* **31** 085007
[287] Esteves B, Drag C, Bourdon A and Alvarez-Laguna A 2022 Experimental and numerical investigation of a gridded ion thruster running with different propellants (I_2, Xe, Kr, Ar) *Proc. 37th Int. Electric Propulsion Conf.* (Electric Rocket Propulsion Society) p IEPC-2022-416
[288] Jia-Richards O and Lafleur T 2023 Iodine electric propulsion system thrust validation: from numerical modeling to in-space testing *J. Propuls. Power* **39** 896
[289] Liu R, Liu W, Li Y, Wang W, Zhang G and Tang H 2024 Low current iodine-fed hollow cathode discharge: insights from fluid model *Plasma Sources Sci. Technol.* **33** 115021
[290] Saifutdinova A, Makushev A, Gatiyatullin F and Saifutdinov A 2024 Simulation of the plasma parameters dynamics in iodine in an electric rocket engine based on ICP discharge *High Energy Chem.* **58** S215
[291] Saifutdinova A, Makushev A, Sysoev S and Saifutdinov A 2024 Parametric analysis of plasma-chemical processes in electrodeless RF and microwave discharges in iodine vapor *High Energy Chem.* **58** 575
[292] Lequette N 2025 Numerical model of the PEGASES spacecraft thruster *PhD Thesis* Institut polytechnique de Paris
[293] Bianchi F M, Vinci A E and Garrigues L 2025 Global modeling of iodine Hall thruster performance and discharge properties *J. Appl. Phys.* **137** 043301
[294] Chabert P, Esteves B, Bourdon A and Lafleur T 2025 Steady-state plasma model of an iodine-fueled Hall thruster *J. Appl. Phys.* **138** 043303
[295] Andrews S, Andriulli R, Souhair N, Di Fede S, Pavarin D, Ponti F and Magarotto M 2023 Coupled global and PIC modelling of the REGULUS cathode-less plasma thrusters operating on xenon, iodine and krypton *Acta Astronaut.* **207** 227
[296] Saini V and Ganesh R 2024 Numerical simulation of an expanding magnetic field plasma thruster: a comparative study for argon, xenon and iodine fuel gases *J. Plasma Phys.* **90** 905900411
[297] Niu X, Li X, Liu H and Yu D 2019 Fluid simulation of ionization process in iodine cusped field thruster *Eur. Phys. J. D* **73** 1
[298] Gehring T, Eizaguirre S, Jin Q, Dycke J, Renschler M and Kling R 2021 On the temperature and plasma distribution of an inductively driven Xe-I_2-discharge *Plasma* **4** 745
[299] Jones A 2019 French startup ThrustMe found fast route to orbit through China's Spacety (SpaceNews) (available at: https://spacenews.com/french-startup-thrustme-found-fast-route-to-orbit-through-chinas-spacety/)
[300] Jones A 2021 French startup demonstrates iodine propulsion in potential boost for space debris mitigation efforts (SpaceNews) (available at: https://spacenews.com/french-startup-demonstrates-iodine-propulsion-in-potential-boost-for-space-debris-mitigation-efforts/)
[301] Space-track.org 2021 *United States Space Command and the Combined Space Component Command* (available at: www.space_track.org)
[302] NASA Goddard Space Flight Center 2020 *General Mission Analysis Tool (GMAT), version R2018a* (available at: https://software.nasa.gov/software/gsc-18094-1)
[303] Rathsman P, Kugelberg J, Bodin P, Racca G D, Foing B and Stagnaro L 2005 SMART-1: development and lessons learnt *Acta Astronaut.* **57** 455
[304] Kerslake W, Goldman R and Nieberding W 1971 SERT II-Mission, thruster performance and in-flight thrust measurements *J. Spacecr. Rockets* **8** 213
[305] Krejci D, Reissner A, Seifert B, Jelem D, Hörbe T, Plesescu F, Friedhoff P and Lai S 2018 Demonstration of the IFM nano FEEP thruster in low Earth orbit *Proc. 4S Symp.* (European Space Agency)
[306] Kramer A, Bangert P and Schilling K 2020 UWE-4: first electric propulsion on a 1U CubeSat—In-Orbit experiments and characterization *Aerospace* **7** 98
[307] Rafalskyi D 2025 private communication

[308] Foust J 2023 Artemis 1 cubesat nearing end of mission (SpaceNews) (available at: https://spacenews.com/artemis-1-cubesat-nearing-end-of-mission/)

[309] Olson K R 2018 *Poisoning & Drug Overdose* 7th edn (Lange Medical Books/McGraw-Hill)

[310] The National Institute for Occupational Safety and Health 2025 *CDC—NIOSH Pocket Guide to Chemical Hazards—Iodine* (available at: www.cdc.gov/niosh/npg/npgd0342.html)

[311] Solomon S, Garcia R R and Ravishankara A 1994 On the role of iodine in ozone depletion *J. Geophys. Res.: Atmos.* **99** 20491

[312] Feng W, Plane J M, Chipperfield M P, Saiz-Lopez A and Booth J-P 2023 Potential stratospheric ozone depletion due to iodine injection from small satellites *Geophys. Res. Lett.* **50** e2022GL102300

[313] Saiz-Lopez A, Plane J M, Baker A R, Carpenter L J, Von Glasow R, Gómez Martín J C, McFiggans G and Saunders R W 2012 Atmospheric chemistry of iodine *Chem. Rev.* **112** 1773

[314] Fourie D, Hedgecock I M, De Simone F, Sunderland E M and Pirrone N 2019 Are mercury emissions from satellite electric propulsion an environmental concern? *Environ. Res. Lett.* **14** 124021

[315] Sabat K C and Murphy A B 2017 Hydrogen plasma processing of iron ore *Metall. Mater. Trans. B* **48** 1561

[316] FAA 2021 *Report to Congress: Risk Associated with Reentry Disposal of Satellites from Proposed Large Constellations in Low Earth Orbit* (FAA)

[317] Becke P S *et al* 2025 Development and iodine testing of a Novel C12A7 electride planar hollow cathode *Research Square Preprint* (https://doi.org/10.21203/rs.3.rs-5738180/v1)

[318] Xin L, Tianhang M, Jianhao Z, Hui L, Zhongxi N and Daren Y 2025 Preliminary characterization of an iodine-compatible LaB_6 hollow cathode *Plasma Sci. Technol.* **27** 064005

[319] Taillefer Z R, Blandino J J and Szabo J 2020 Characterization of a barium oxide cathode operating on xenon and iodine propellants *J. Propuls. Power* **36** 575

[320] Benavides G F, Kamhawi H, Mackey J, Haag T and Costa G 2018 Iodine Hall-effect electric propulsion system research, development and system durability demonstration *Proc. 2018 Joint Propulsion Conf.* (AIAA) p AIAA-2018-4422

[321] Szabo J, Robin M, Paintal S, Pote B and Hruby V 2012 High density Hall thruster propellant investigations *Proc. 48th AIAA/ASME/SAE/ASEE Joint Propulsion Conf. & Exhibit* (AIAA) p AIAA-2012-3853

[322] Rand L P and Williams J D 2013 Instant start electride hollow cathode *Proc. 33rd Int. Electric Propulsion Conf.* (Electric Rocket Propulsion Society) p IEPC-2013-305

[323] Rand L P 2014 A calcium aluminate electride hollow cathode *PhD Thesis* Colorado State University

[324] Zhiwei H, Pingyang W, Zhongxi N, Zhanwen Y and Zongqi X 2022 Early experimental investigation of the C12A7 hollow cathode fed on iodine *Plasma Sci. Technol.* **24** 074004

[325] Kottke N G, Tajmar M and Hey F G 2024 Hollow cathode testing of Y_2O_3, La_2O_3-doped tungsten and LaB_6 emitters with krypton and iodine *Vacuum* **220** 112812

[326] Rossi E Z, Rafalskyi D, Lafleur T, Dudin S, Bore A, Habl L and Jain P 2024 Lifetime testing challenges of a complete iodine-based electric propulsion system *Proc. 38th Int. Electric Propulsion Conf.* (Electric Rocket Propulsion Society) p IEPC-2024-627

[327] Hey W and Leipunski A 1930 Bildung negativer Ionen einiger Stoffe *Z. Phys.* **66** 669

[328] Mazouffre S, Dannenmayer K and Pérez-Luna J 2007 Examination of plasma-wall interactions in Hall effect thrusters by means of calibrated thermal imaging *J. Appl. Phys.* **102** 023304

[329] Dannenmayer K and Mazouffre S 2008 Sizing of Hall effect thrusters with input power and thrust level: an empirical approach *J. Tech. Phys.* **49** 231

[330] Liard L, Raimbault J, Rax J and Chabert P 2007 Plasma transport under neutral gas depletion conditions *J. Phys. D: Appl. Phys.* **40** 5192

[331] Gaboriau F and Boeuf J-P 2014 Chemical kinetics of low pressure high density hydrogen plasmas: application to negative ion sources for ITER *Plasma Sources Sci. Technol.* **23** 065032

[332] Popov N 2011 Fast gas heating in a nitrogen-oxygen discharge plasma: I. Kinetic mechanism *J. Phys. D: Appl. Phys.* **44** 285201

[333] Donnelly V and Malyshev M 2000 Diagnostics of inductively coupled chlorine plasmas: measurements of the neutral gas temperature *Appl. Phys. Lett.* **77** 2467

[334] Pintassilgo C D and Guerra V 2015 On the different regimes of gas heating in air plasmas *Plasma Sources Sci. Technol.* **24** 055009

[335] Pearton S, Abernathy C and Vartuli C 1994 ECR plasma etching of GaN, AlN and InN using iodine or bromine chemistries *Electron. Lett.* **30** 1985

[336] Jorns B and Lafleur T 2023 Foundations of plasmas as ion sources *Plasma Sources Sci. Technol.* **32** 014001

[337] Petro E M and Sedwick R J 2017 Effects of water-vapor propellant on electrodeless thruster performance *J. Propuls. Power* **33** 1410

[338] Nakagawa Y, Koizumi H, Naito Y and Komurasaki K 2020 Water and xenon ECR ion thruster-comparison in global model and experiment *Plasma Sources Sci. Technol.* **29** 105003

[339] Sheppard A J and Little J M 2024 Characterization of water propellant in an electron cyclotron resonance thruster *Phys. Plasmas* **31** 073507

[340] Andreussi T, Ferrato E and Giannetti V 2022 A review of air-breathing electric propulsion: from mission studies to technology verification *J. Electr. Propuls.* **1** 31

[341] Cerny D, Bacis R, Bussery B, Nota M and Verges J 1991 Experimental determination and calculation of the collision relaxation rates in the $5^2P_{1/2}$ and $5^2P_{3/2}$ levels of atomic iodine *J. Chem. Phys.* **95** 5790

[342] Luc-Koenig E, Morillon C and Vergès C 1973 Etude de la transition “interdite” $^2P_{1/2} \rightarrow {}^2P_{3/2}$ de la configuration np^5 dans le brome et l’iode par spectrometrie de fourier *Physica* **70** 175

[343] Ha T-K, He Y, Pochert J, Quack M, Ranz R, Seyfang G and Thanopoulos I 1995 Absolute integrated band strength and magnetic dipole transition moments in the $^2P_{3/2} \rightarrow {}^2P_{1/2}$ fine structure (with hyperfine structure) transition of the iodine atom: experiment and theory *Ber. Bunsenges. Phys. Chem.* **99** 384

[344] Luc-Koenig E, Morillon C and Verges J 1975 Etude expérimentale et théorique de l’iode atomique. Observation du spectre d’arc infrarouge, classification et structure hyperfine *Phys. Scr.* **12** 199